AFOSR-TR-95

0617

REPORT DOCUMENTATION PAGE

Public reporting burden for this collection of information is estimated to average ... hour per response, ... gathering and maintaining the data needed, and completing and reviewing the collection of information. Including suggestions for reducing this burden, to Washington Headquarters ... Davis Highway, Suite 1204, Arlington, VA 22202-4302, and to the Office of Management and Budget, Pa...

1. AGENCY USE ONLY (Leave blank)	2. REPORT DATE	3. REPORT TYPE AND DATES COVERED
		FINAL REPORT 15 Apr 92 - 14 Apr 95

4. TITLE AND SUBTITLE
Laser Interactions in STM and STM-Like Devices: Applications to Infrared and Optical Detection

5. FUNDING NUMBERS
61102F
2305/GS

6. AUTHOR(S)
Professor T. E. Sullivan and Prof P. H. Cutler

7. PERFORMING ORGANIZATION NAME(S) AND ADDRESS(ES)
Temple University
Department of Electrical Engineering
Philadelphia, PA

8. PERFORMING ORGANIZATION REPORT NUMBER

9. SPONSORING/MONITORING AGENCY NAME(S) AND ADDRESS(ES)
AFOSR/NE
110 Duncan Avenue Suite B115
Bolling AFB DC 20332-0001

10. SPONSORING/MONITORING AGENCY REPORT NUMBER
F49620-92-J-0209

11. SUPPLEMENTARY NOTES

12a. DISTRIBUTION/AVAILABILITY STATEMENT
APPROVED FOR PUBLIC RELEASE: DISTRIBUTION UNLIMITED

12b. DISTRIBUTION CODE

13. ABSTRACT (Maximum 200 words)

SEE FINAL REPORT ABSTRACT

DTIC
ELECTE
OCT 13 1995
S D
B

19951011 162

14. SUBJECT TERMS

15. NUMBER OF PAGES

16. PRICE CODE

17. SECURITY CLASSIFICATION OF REPORT	18. SECURITY CLASSIFICATION OF THIS PAGE	19. SECURITY CLASSIFICATION OF ABSTRACT	20. LIMITATION OF ABSTRACT
UNCLASSIFIED	UNCLASSIFIED	UNCLASSIFIED	UNCLASSIFIED

Final Report

Laser Interactions in STM and STM-like Devices: Applications to Infrared and Optical Detection.

T.E. Sullivan
Department Electrical Engineering
Temple University
Philadelphia, PA

P.H. Cutler
Department of Physics
Pennsylvania State University
University Park, PA

Grant Number: F 49620-92-J00209

Executive Summary

This final report contains a summary of the principle finding. Experimental and Theoretical details are presented in greater detail in a series of Appendices. This format was chosen since this report may be read by individuals with specific interests thereby enabling the reader to find the relevant detailed information in one place.

The principle research objectives of the grant were:

1) Investigate the infrared and optical receiving properties of STM irradiated tunnel junctions and to determine the effects of geometry, temperature, and materials properties on the receiving properties.

2) Investigate the proposal that the electron transit time in irradiated vacuum tunnel structures can be characterized in terms of the natural time scale provided by the laser frequency and to determine the physical mechanisms limiting the response of the tunnel device.

Several of the significant accomplishments achieved were:

1) Successfully fabricated atomically sharp silicon emitter embedded in a thin, 30 Angstrom, tunnel oxide. This represented the first fabrication of the solid state equivalent of a STM as a circuit element.

2) Extended the fundamental understanding of the limitations of the planar Fowler-Nordheim theory when applied to tunneling from atomically sharp emitter tips by calculating the fields induced at these tips using a more realistic prolate-spheroidal co-ordinate model. This is a marked deviation from the purely planar Fowler-Nordheim approximation. This calculation represented the solution to a previously unsolved problem in electrostatics. A fully three dimensional analytic solution for a sharp tip and a planar base was found. The analytic solution included the effects of the image and multiple image potentials in the model calculation.

y Codes
Avail and/or
Dist Special
A-1

3) Calculated the effects of inelastic processes in time dependent tunneling in an STM junction using a kinetic formulation of the transfer Hamiltonian method.

4) Designed and built a digitally controlled, network accessible STM which affords remote accessing over the university network and real time data acquisition. All aspects of the experimental control of the STM are under computer control, including coarse and fine approach, settling and pulse control of laser and incoherent sources.

5) Determined that the role of incoherent photoassisted tunneling in the visible region is minimal. Incoherently stimulated tunnel currents were below 0.01 nanoamperes. This is contrasted with typical STM tunnel currents on the order of 1 nanoampere.

6) Preliminary experiments of the role of surface modification in the Fowler-Nordheim or field emission range of tunneling appears to be associated with a field effect and not with thermal evaporation. This has important implications in the fabrication of 10-20 Angstrom feature sized devices. Experiments are continuing on establishing the mechanism for the fabrication of nanosized dots on the order of 20 Angstrom diameters and 10 Angstrom depth.

7) Developed the imaging and control software to monitor surface modification between laser pulses to establish greater accuracy in nano distance measurements which affect determination of tunnel times.

These investigation have important payoff to the Air Force in the areas of surface modification and nano-scale fabrication and the area of high speed tunnel devices acting as either switching elements or as infrared and optical detectors.

Introduction

Selective room temperature infrared and laser receivers incorporated into silicon integrated circuits have important implications in high speed infrared signal processing and optical computation. Although a wide range of III-V and II-VI compound semiconductors exist with stoichiometrically adjustable band gaps these materials must be heteroepitaxially grown by MBE or MOCVD, and as such are costly and difficult to produce. In addition long wavelength infrared detectors using extrinsic silicon require cooling to liquid helium temperatures.

Infrared laser frequency mixing, and tunnel time measurements using laser rectification in STM junctions have offered the opportunity to explore variable gap metal on metal and metal on silicon tunnel devices in a controlled way. The sharp or pointed tip geometry introduces a geometric asymmetry into the tunnel junction which produces a field enhancement for tunneling from the emitter tip. This tunneling asymmetry provides a mechanism for rectifying an alternating laser field.

GANT Fabrication

Atomically sharpened silicon emitters are formed from a heavily doped n-type substrate. The emitters form small field emission-like structures that are positioned within 30 Angstroms from a planar substrate by growing a thin tunnel oxide on the silicon emitter. A thicker deposited oxide is used to planarize the surrounding emitter surface. One of the drawbacks to fabricating nano-sized junctions with macroscopic integrated circuit processes is the device variability which is introduced as the feature size becomes progressively smaller. Wet chemical etch as well as reactive ion etching of the thick planarizing oxide opens windows in the oxide which are subject to variation due to the diffusive nature of the etching process. The opening in the thick oxide effectively determines the emission area for each of the field emitters in the array. The critical spacing between anode and cathode is unaffected since that critical distance is set by the

subsequent growth of the tunnel oxide atop the exposed emitter tip. The fabrication and the electrical testing of the devices is presented in Appendix A

A statistical analysis of the emission area variability is important in determining the total emission current developed by the tunnel array. This realization led to an investigation of the three important factors which will affect the final design rules for the fabrication of GANT devices.

The factors are:
1) The three dimensional nature of the emitter field in the tunnel junction.
2) The effective emission area which may be significantly different from the oxide hole opening.
3) The statistical variability of the tip radius formed by stress inhibited thermal oxidation.

Three dimensional tunnel field

In all previous calculations of the electric field in an STM junction we have used the prolate spheroidal model and calculated the on-axis electric field. This effectively reduced the calculation of the electric field in the tunnel junction to a one-dimensional case. At the time this was appropriate since the geometrically correct on axis solution was obtained analytically it represented the maximum tunnel junction field and was subsequently used in the WKB approximation to calculate the maximum tunnel current density.

The analytic solution for the full three dimensional field configuration including a fully three dimensional image and multiple image interactions had remained an unsolved problem. Although numerical methods have been suggested these solutions suffer from the usual problem of accuracy without a comparison to an analytic solution. In Appendix B the details and results of that calculation are presented.

The importance of this solution for tunneling in geometrically asymmetric

junctions should not be underestimated. With a knowledge of the spatial dependence of the electric field reasonably accurate estimates of emission areas are possible. These results are discussed in Appendix B.

Statistical Analysis of Emitter Tip Variation and Effect on Current

The formation of atomically sharp and nearly atomically sharp field emitters in silicon rests on a technique known as stress inhibited oxidation. This oxidation process and well as all other oxidation processes rely on the diffusion of the oxidizing species. For nearly atomically sharp tips the critical oxidation area is confined to a region less than 100 X 100 Angstroms in size. Fluctuations in the oxidizing agent concentration produce variations in the final emitter shape. On the average this variation may at first seem negligibly small. In fact this variation has a exponentially large effect of the final current density.

Unlike the case of planar tunnel structures and isoplanar integrated circuits these devices follow a Fowler Nordheim-like current voltage characteristic. The exponential nature of the current density on the tunnel field is reflected directly in the sharpness of the respective tip radii. A small variation in the tip radius produces a large change in the emitter current.

In the analysis we have performed we have analytically derived probability distribution functions for arrays of emitter devices for two cases: any Gaussian distribution of tip radii and any Rayleigh distribution of tip radii. The controlling current voltage relationship was assumed to follow a classical Fowler-Nordheim law. This result is the first time that an analytic probability distribution function has been obtained for arrays of field emitter devices. This result becomes an important analytic tool in characterizing process variation and predicting array performance.

These results are presented in detail in Appendix C and are generally applicable to field emitter arrays independent of the tip-anode spacing..

Inelastic Processes in Tunneling

The shape of the tunnel current as a function of tip-anode spacing is determined using kinetic theory and the transfer Hamiltonian method. The photo-assisted inelastic tunneling current is given in terms of laser frequency, electric field (which is calculatable from the exact three dimensional solution given in appendix B), and appropriate barrier parameters for a materially asymmetric junction. The calculation of the laser stimulated inelastic current is based on a free electron model. The technique, however, is extendable to include the effects of band structure.

The results of this calculation are presented in Appendix D.

Digitally Controlled STM

A detailed description of the computer controlled STM is presented in Appendix E. The STM itself is directly operated from remote sites through the university network. Remote operation proved to be necessary given the location of the Nanostructures and Materials Laboratory on the 7th Floor of the Engineering Building. The location of the laboratory on the 7th floor is adjacent to the building elevator shaft which proved a regular source of vibrations which were damped. Additionally the build is adjacent to a trolley line which produces significant low frequency noise. Successful operation of the STM and the need to accurately control the tip-anode spacing required that virtually all experimentation be performed between midnight and six am in the morning. The experiments are set up during the day and the data acquisition can be accomplished from adjacent offices and via long distance telephone. Without the remote accessing of the system the noise characteristics of the building would have dominated.

A discussion of the computer system designed and used through out the grant t appear in Appendix E.

Surface Modification

The determination of the operational tunnel time in a laser irradiated STM requires a controlled tip-base spacing. During the experimental calibration of the system in preparation for the laser experiments an unexpected modification of the base surface was detected. The gold base became pitted giving rise to spurious tip-base spacings. This modification of the surface did not occur when the STM was operating in the imaging or normal tunneling mode. This mode is defined as tip-base spacings such that the STM IV characteristic is linear- that is spacings less than 10 Angstroms. Surface modification occurred only when the STM operated in the Fowler-Nordheim region-highly non-linear current voltage characteristic, and only for the case when the tip was positively biased. This condition corresponds to the forward bias case during laser irradiation.

Preliminary results indicate the creation of circular and elliptical pits is not related to heating of the gold anode. At the time of this report preliminary results indicate that the creation of the nano-size pits is a field effect. Additional temperature calculations and experiments to determine the mechanism for the pit creation are currently underway in an effort to ascertain the formation mechanism.

These results on surface modification during static IV testing of the junction came about due to an upgrade we developed for our imaging software. Since the detailed structure of the surface is important in maintaining constant tip-base spacings planar anode regions are sought for IV testing. Once a region is selected it is extensively mapped. Static current voltage measurements are performed with re-imaging before and after each IV is taken. This is a tedious and time consuming procedure. During such testing the field induced pits were discovered.

An important series of experiments are about to be started which require further modifications to the software. Since this surface modification is believed to be a field induced effect- the transient or induced current may play the dominant role in creating the pits. Induced currents occurring when the system is switching voltages may be further reduced by changing

the number of incremental voltage steps and hence eliminate the pitting.

On the other side of the issue is the important observation that surface modification in the STM junction is related to field and not temperature effects could have a significant impact of nano-scale surface modification.

Figures of nanoscale field induced pits are shown in Appendix F.

Laser Induced Thermoelectric Effects in STM Junctions

We have calculated the spatial and temporal temperature distributions for a conical metal emitter under laser irradiance. The full three dimensional heat diffusion equation is solved simultaneously wit h the Fourier equation for heat flux, assuming no radiation losses. Both Joule heating and Thomson thermoelectric effects were studies.

The details of the Green's function method used in the calculation are given in Appendix G.

Appendix A
Fabrication and Testing of Geometrically Asymmetric Tunnel Structure

Geometrically Asymmetric Nano-tunnel Structures
D.C.Schweitzer, T.E. Sullivan
Department of Electrical Engineering
Temple University, Philadelphia, PA 19122
R.B. Marcus
Department of Chemistry
New Jersey Institute of Technology
Newark, N.J.
Paul H. Cutler
Department of Physics
The Pennsylvania State University
University Park, PA 16802

Introduction

In recent years there has been renewed interest in the use of vacuum microelectronic devices for flat panel displays and rf generation. In this paper we extend those application to the development of high speed optical and infrared detectors. The development of both the point contact diode and the STM tunnel junction have shown that novel geometrically asymmetric nanotunnel device structures can be used as an alternative method of detection for high speed optically modulated signals. One of the most promising device structures under investigation are the at atomically sharpened silicon field emitters. While these devices are similar to the electrochemically etched metal emitters used in both the scanning tunneling microscope and field ion microscopes, atomically sharpened silicon emitters have many advantages over these devices.

We present the results on the development of a novel asymmetric tunnel structure which can be directly incorporated into a silicon integrated circuit using standard semiconductor processing technologies. This device structure is referred to as a Geometrically Asymmetric Nanotunnel Structure or GANT structure. The GANT structure consists of an atomically sharpened silicon field emitter separated from a planar metal electrode by a thin (d< 30 Angstroms) tunnel gap. It will be shown that an emitter processing scheme such as this facilitates:(i) the fabrication of large arrays of identical field emitter elements, (ii) the fabrication of controllable, repeatable cathode to anode contact geometries, and (iii) the incorporation of field emission devices into integrated circuits using current semiconductor processing technologies.

In addition, electrical (I-V) characteristics show a current density enhancement of

vacuum tunnel gap, into an integrated circuit has been greatly simplified through the use of a thermally grown silicon-dioxide barrier, The use of a low temperature, thermally grown, silicon dioxide film has been shown to provide an accurate and repeatable method for forming thin tunnel gap spacings < 50 Angstroms.

Although the GANT structure presented in this paper differs in many ways from an STM tunnel junction, it has been shown that this design scheme has a number of advantages over STM/point contact tunnel structures. These advantages include (i) fabrication in large arrays, (ii) fabrication with a known, controllable, and repeatable contact geometry and (iii) can be readily incorporated into standard integrated circuits using current processing technologies.

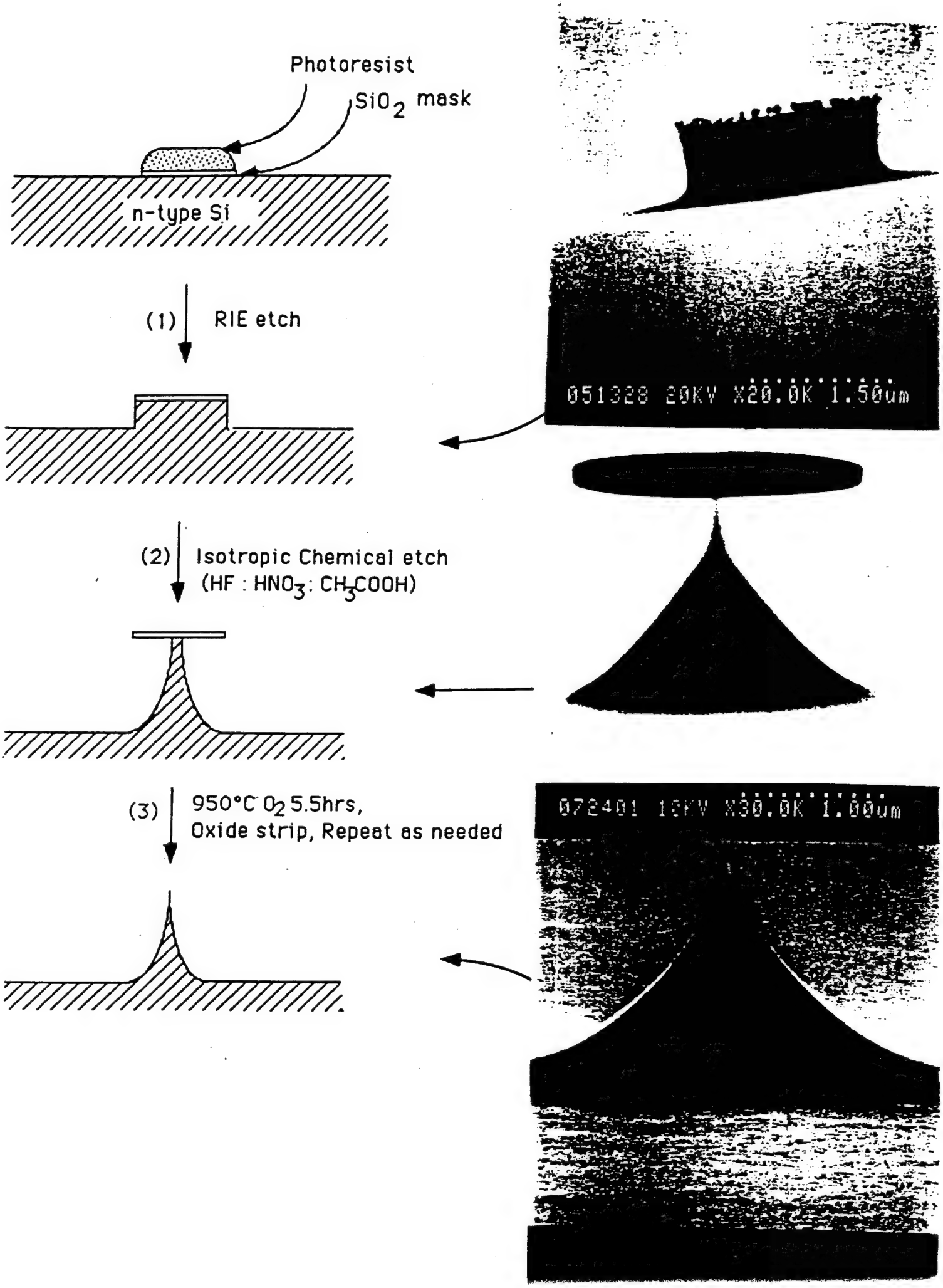
Photoresist
SiO_2 mask
n-type Si
(1) RIE etch
(2) Isotropic Chemical etch
(HF : HNO_3 : CH_3COOH)
(3) 950°C O_2 5.5hrs,
Oxide strip, Repeat as needed
051328 20KV X20.0K 1.50um
072401 10KV X30.0K 1.00um

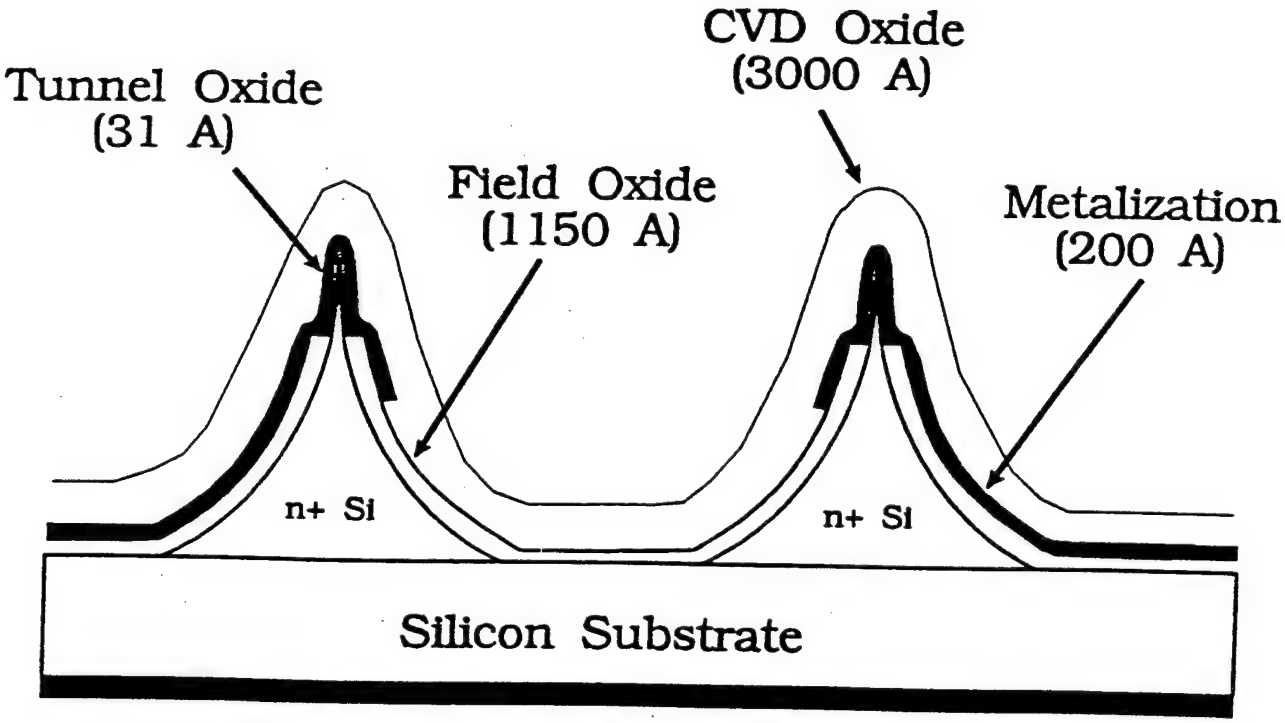
CVD Oxide
(3000 A)
Tunnel Oxide
(31 A)
Field Oxide
(1150 A)
Metalization
(200 A)
n+ Si
n+ Si
Silicon Substrate

Appendix B

NAME: Using APL format PAGE: 1 SESS: 29 OUTPUT: Mon Sep 19 17:13:56 1994
xy2/third/journals3/apl/24oct94/020443apl
BY: grace REV: grace@xy2/third/CLS_journals3/GRP_apl/JOB_24oct94/DIV_020443apl ♦ 020443apl
THIS IS A LASER PROOF

Three-dimensional electrostatic potential, and potential-energy barrier, near a tip-base junction

Lo-Hong Pan and Thomas E. Sullivan
Department of Electrical Engineering, Temple University, Philadelphia, Pennsylvania 19122

Vallorie J. Peridier
Department of Mechanical Engineering, Temple University, Philadelphia, Pennsylvania 19122

Paul H. Cutler and Nicholas M. Miskovsky
104 Davey Lab, The Pennsylvania State University, University Park, Pennsylvania 16802

(Received 28 March 1994; accepted for publication 17 August 1994)

The geometry of an atomically sharp or nearly atomically sharp tip in proximity to a planar anode may be closely approximated in the prolate-spheroidal coordinate system. An exact three-dimensional electrostatic-potential solution for a free charge in such a tip/base junction is given in this letter, including calculations for both the symmetrical on-axis case and the asymmetric off-axis case. An exact solution for the potential-energy barrier is also given; this solution has immediate applications in three-dimensional tunneling studies and in calculations of electron trajectories in micron- and submicron-sized field-emitter arrays. © *1994 American Institute of Physics.*

We report that an exact three-dimensional solution to the Laplace/Poisson equation has been obtained in the prolate-spheroidal coordinate system. This result is significant because the prolate-spheroidal coordinate system provides an accurate geometrical representation of an emission tip close to a planar anode, a geometry which arises in scanning tunneling microscope devices (STM) and related tunnel structurs. In this letter the first off-axis calculation for the potential due to a free electron in such a voltage-biased tip/base junction is given.

Theoretical understanding of quantum-electronic phenomena in nanoscale devices is critical in the continued development of nanoelectronics. As important class of quantum-electronic devices consist of a biased tip/anode or tip/base junction, in which the tip is atomically sharp ($r_{tip}<2$ nm) and close (3 nm) to the planar surface. For example, such devices include scanning tunneling microscopes (STM) and geometrically asymmetric nanotunnel structures (GANTS).[1] Of particular interest is the capability to quantify the tunneling current for such devices, a calculation which, in turn, requires an accurate estimate of the induced potential energy of a point charge in the tip/base junction. Much of the theoretical work to date has been carried out using an effectively one-dimensional or planar analysis, and while there are some devices (e.g., quantum-well heterostructures) for which this one-dimensional approach proves to be an adequate strategy, it is clearly not an ideal geometrical approximation for a three-dimensional device utilizing a tip/base junction. However, it emerges that the geometrical features of devices such as the STM may be closely approximated in the prolate-spheroidal coordinate system, with the tip and base each represented as a hyperboloid surface.

energy barrier. It is worthwhile to note that exact solutions such as these permit the calculation of these fields to *arbitrary* accuracy, even in regions of severe spatial variation; calculations are given here for the on- and off-axis case of a point charge in a biased tip/anode junction.

To begin the analysis, the prolate-spheroidal coordinate system is given by[2]

$$x=a\sinh(u)\sin(v)\cos(\phi),$$
$$y=a\sinh(u)\sin(v)\sin(\phi), \tag{1}$$
$$z=a\cosh(u)\cos(v),$$

where a is one-half the distance between the hyperboli foci; curves corresponding to constant v are hyperboloid surfaces, while those for constant u are prolate-spheroidal surfaces. Geometrically the problem has axial symmetry, and if the charge is on the symmetry axis $u=0$ the solution for the resulting electrostatic potential is effectively a one-dimensional problem which could be addressed, say, with a method-of-images technique.[3,4] However, if the charge is located at an off-axis position then the problem for the electrostatic potential is fully three dimensional.

Starting with (1), the variable transformations $\xi=\cosh(u)$, $\eta=\cos(v)$, generate a coordinate system defined by

$$x=a\sqrt{\xi^2-1}\sqrt{1-\eta^2}\cos(\phi),$$
$$y=a\sqrt{\xi^2-1}\sqrt{1-\eta^2}\sin(\phi), \tag{2}$$
$$z=a\xi\eta.$$

The region between the two hyperboloid surfaces is the

$$\int_1^\infty K_\tau^m(\mu)K_{\tau'}^m(\mu)d\mu=\frac{(-1)^m}{\tau\tanh(\pi\tau)}\frac{\Gamma(\frac{1}{2}+i\tau+m)}{\Gamma(\frac{1}{2}+i\tau-m)}\times\delta(\tau-\tau'), \tag{10}$$

note that the second solution for $K_\tau^m(\mu)$ is $K_\tau^m(-\mu)$. From (8) it is evident that the solutions for $S(\eta)$ are also conical functions. Consequently, the general solution for V_I, noting that the eigenvalues m are discrete and the eigenvalues τ are continuous, is

$$V_I=\sum_{m=0}^{\infty}(2-\delta_{0,m})\cos(m\phi)\cdot\int_0^\infty[B_\tau^m K_\tau^m(\eta)+C_\tau^m K_\tau^m(-\eta)]K_\tau^m(\xi)d\tau, \tag{11}$$

with

$$B_\tau^m=\frac{q}{4\epsilon_0 a}\alpha_\tau^m K_\tau^m(\xi_c)K_\tau^m(-\eta_2)\cdot\frac{K_\tau^m(\eta_c)K_\tau^m(-\eta_1)-K_\tau^m(-\eta_c)K_\tau^m(\eta_1)}{K_\tau^m(\eta_1)K_\tau^m(-\eta_2)-K_\tau^m(-\eta_1)K_\tau^m(\eta_2)}, \tag{12}$$

$$C_\tau^m=\frac{q}{4\epsilon_0 a}\alpha_\tau^m K_\tau^m(\xi_c)K_\tau^m(\eta_1)\cdot\frac{K_\tau^m(-\eta_c)K_\tau^m(\eta_2)-K_\tau^m(\eta_c)K_\tau^m(-\eta_2)}{K_\tau^m(\eta_1)K_\tau^m(-\eta_2)-K_\tau^m(-\eta_1)K_\tau^m(\eta_2)}.$$

Here, the charge is located at $\mathbf{x}_c=(\xi_c,\eta_c,0)$, and the constant α_τ^m in (12) is

$$\alpha_\tau^m=\frac{\tau\tanh(\pi\tau)}{\cosh(\pi\tau)}\left[\frac{\Gamma(\frac{1}{2}+i\tau-m)}{\Gamma(\frac{1}{2}+i\tau+m)}\right]^2. \tag{13}$$

Thus the electrostatic potential V (4) is calculated from (6), (7), and (11), and the potential energy Φ is

$$\Phi=q(V_B+V_I), \tag{14}$$

where V_B is given by (6) and V_I by (11). Also, it can be shown[7] that the electric field on the emitter surface at $\eta=\eta_1$, E_1, is

$$E_1=\frac{-2V_0}{a}\frac{1}{\sqrt{\xi^2-\eta_1^2}\sqrt{1-\eta_1^2}}\frac{1}{\ln\left(\frac{1+\eta_2}{1-\eta_2}\frac{1-\eta_1}{1+\eta_1}\right)}+\frac{q}{2\pi a\epsilon_0}\frac{1}{\sqrt{\xi^2-\eta_1^2}\sqrt{1-\eta_1^2}}\cdot\sum_{m=0}^{\infty}(-1)^m(2-\delta_{o,m})$$
$$\times\cos(m\phi)\int_0^\infty d\tau\left[\tau\tanh(\pi\tau)\frac{\Gamma(\frac{1}{2}+i\tau-m)}{\Gamma(\frac{1}{2}+i\tau+m)}[K_\tau^m(\xi_c)K_\tau^m(\xi)]\left(\frac{K_\tau^m(-\eta_c)K_\tau^m(\eta_2)-K_\tau^m(\eta_c)K_\tau^m(-\eta_2)}{K_\tau^m(\eta_1)K_\tau^m(-\eta_2)-K_\tau^m(-\eta_1)K_\tau^m(\eta_2)}\right)\right]. \tag{15}$$

Note that the first term in Eq. (15) is the emitter-surface electric field due to the bias potential which is independent of the charge location; the second term is the interaction field produced by the induced surface-charge distributions on the tip and base and the free-charge located at $\mathbf{x}_c=(\xi_c,\eta_c,0)$.

Figure 2 shows computed contour plots of the potential V due to a point charge in a voltage-biased tip–base junction, for both the on-axis and an off-axis case. In both plots: $\eta_1=0.9$ (which corresponds to a tip half-angle of 0.45 radians or 26°); the value of a is chosen so that the radius of the tip at the apex is 20 Å; and the bias voltage of the tip relative to the base is 5 V.

In conclusion, an exact three-dimensional solution for the electrostatic potential due to a charge in a voltage-biased tip/anode junction, modeled in the prolate-spheroidal coordinate system, has been obtained. The results of this study will be used for characterizing the tunneling current at a tip/anode junction using a three-dimensional tunneling analysis, and will be used to carry out a systematic study of off-axis tunneling and its impact on the estimation of active emission areas in nanosized devices.

This work was supported in part by AFOSR Grant No. 49620-92J-0202P00001.

[1] T. E. Sullivan, Y. Kuk, and P. H. Cutler, IEEE Trans. Electron Devices II 31, 2659 (1989).
[2] G. Arfken, *Mathematical Methods for Physicists*, 2nd ed. (Academic, New York, 1970), pp. 103–106.
[3] P. H. Cutler, J. He, J. Miller, N. M. Miskovsky, B. Weiss, and T. E. Sullivan, Prog. Surf. Sci. 42, 169 (1993).
[4] J. He, P. H. Cutler, N. M. Miskovsky, T. E. Feuchtwang, T. E. Sullivan, and M. Chung, Surf. Sci. 246, 348 (1991).
[5] E. W. Hobson, *Theory of Spherical and Ellipsoidal Harmonics* (Chelsea, New York, 1965).
[6] R. G. van Nostrand, J. Math. Phys. 33, 276 (1954).
[7] V. J. Peridier, L. H. Pan, and T. E. Sullivan (unpublished).

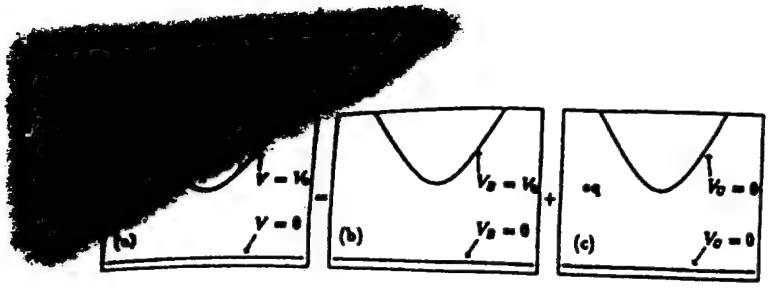

FIG. 1. (a) The problem for V, the total potential energy. (b) The subsidiary problem for V_B, the potential energy due to the tip/anode bias. (c) The subsidiary problem for V_C, the potential energy due to the charge.

$$\nabla^2=\frac{1}{a^2(\xi^2-\eta^2)}\left[\frac{\partial}{\partial\xi}\left((\xi^2-1)\frac{\partial}{\partial\xi}\right)+\frac{\partial}{\partial\eta}\left((1-\eta^2)\frac{\partial}{\partial\eta}\right)+\frac{\xi^2-\eta^2}{(\xi^2-1)(1-\eta^2)}\frac{\partial^2}{\partial\phi^2}\right]. \tag{3}$$

The Laplacian operator is linear, and consequently, the solution for the potential V can be expressed as the sum of two subsidiary potentials,

$$V=V_B+V_C. \tag{4}$$

Here, V_B is the potential due to the bias voltage applied to the tip-plate junction, for instance V_0, and V_C includes the effects of the charge's interaction with the induced surface-charge distribution on the base and tip; note that this surface change is distributed so as to yield zero potential on these conducting surfaces. Schematics associated with V and the subsidiary problems V_B, V_C are given in Fig. 1.

From Fig. 1(b) it is evident that the problem for V_B, the potential due solely to the potential-bias V_0 between the tip and anode, is independent of ξ, ϕ, and the physical location of the charge $\mathbf{x}_c$. Thus, the equations governing V_B are

$$\frac{\partial}{\partial\eta}\left[(1-\eta^2)\frac{\partial}{\partial\eta}\right]V_B=0,\quad V_B(\eta_1)=V_0,\quad V_B(\eta_2)=0. \tag{5}$$

The solution for V_B may be found by elementary methods and is

$$V_B=V_0\frac{\ln\left[\left(\frac{1+\eta_2}{1-\eta_2}\right)\left(\frac{1-\eta}{1+\eta}\right)\right]}{\left[\left(\frac{1+\eta_2}{1-\eta_2}\right)\left(\frac{1-\eta_1}{1+\eta_1}\right)\right]}. \tag{6}$$

The potential V_C due to the charge satisfies the Poisson equation and may be written as the sum of a general (homogeneous) and a particular solution, viz.

$$V_C=\frac{q}{4\pi\epsilon_0|\mathbf{x}-\mathbf{x}_c|}+V_I. \tag{7}$$

The interaction potential V_I satisfies the Laplace equation and has homogeneous boundary conditions; however, since the potential is fully three dimensional it is convenient to "separate" the solution into a product of functions in each coordinate direction, for instance $V_I=R(\xi)S(\eta)F(\phi)$. Applying the Laplacian operator (3) on V_I in this separated form and designating the separation constants as A and m^2, the solutions in each coordinate variable are governed by

$$\frac{\partial^2F}{\partial\phi^2}+m^2F=0,$$
$$\frac{\partial}{\partial\xi}\left\{(\xi^2-1)\frac{\partial R}{\partial\xi}\right\}-\left\{A+\frac{m^2}{\xi^2-1}\right\}R=0, \tag{8}$$
$$\frac{\partial}{\partial\eta}\left\{(1-\eta^2)\frac{\partial S}{\partial\eta}\right\}+\left\{A-\frac{m^2}{1-\eta^2}\right\}S=0,$$

To obtain $F(\phi)$ the charge may be set, with no loss of generality, to an azimuthal location $\phi=0$, so that the solutions for $F(\phi)$ will be of the form $\cos(m\phi)$.

The boundary conditions for V_I are homogeneous at η_1, η_2; this suggests that $R(\xi)$ must be expanded in an orthogonal set of functions and thus the constant A must be negative. Setting $A=n(n+1)$ gives associated Legendre polynomials P_n^m with complex degree $n=-\frac{1}{2}\pm i\tau$. Following Hobson,[5] designate

$$K_\tau^m(\mu)=P_{-1/2\pm i\tau}^m(\mu); \tag{9}$$

the functions K_τ^m are called conical functions, and the orthogonality relation for the conical functions is[6]

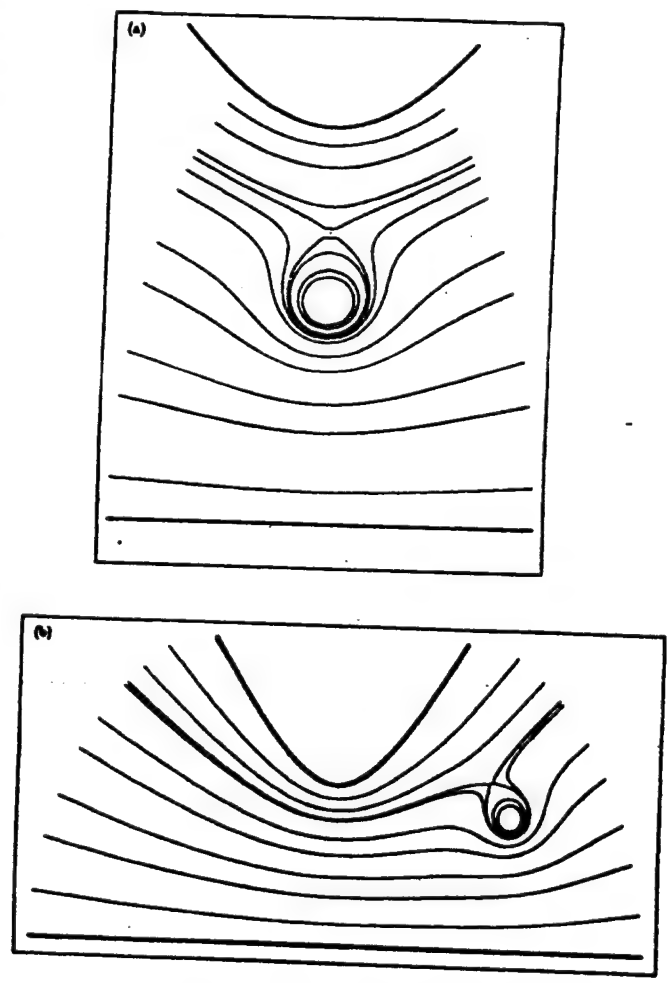

FIG. 2. (a) Contours of constant potential for a charge on the symmetry axis. (b) Contours of constant potential for an off-axis charge, in the plane of the charge.

$$\int_1^\infty K_\tau^m(\mu)K_{\tau'}^m(\mu)d\mu=\frac{(-1)^m}{\tau\tanh(\pi\tau)}\frac{\Gamma(\frac{1}{2}+i\tau+m)}{\Gamma(\frac{1}{2}+i\tau-m)}\times\delta(\tau-\tau'),\tag{10}$$

note that the second solution for $K_\tau^m(\mu)$ is $K_\tau^m(-\mu)$. From (8) it is evident that the solutions for $S(\eta)$ are also conical functions. Consequently, the general solution for V_I, noting that the eigenvalues m are discrete and the eigenvalues τ are continuous, is

$$V_I=\sum_{m=0}^{\infty}(2-\delta_{0,m})\cos(m\phi)\int_0^\infty[B_\tau^m K_\tau^m(\eta)+C_\tau^m K_\tau^m(-\eta)]K_\tau^m(\xi)d\tau,\tag{11}$$

with

$$B_\tau^m=\frac{q}{4\epsilon_0 a}\alpha_\tau^m K_\tau^m(\xi_c)K_\tau^m(-\eta_2)\cdot\frac{K_\tau^m(\eta_c)K_\tau^m(-\eta_1)-K_\tau^m(-\eta_c)K_\tau^m(\eta_1)}{K_\tau^m(\eta_1)K_\tau^m(-\eta_2)-K_\tau^m(-\eta_1)K_\tau^m(\eta_2)},\tag{12}$$

$$C_\tau^m=\frac{q}{4\epsilon_0 a}\alpha_\tau^m K_\tau^m(\xi_c)K_\tau^m(\eta_1)\cdot\frac{K_\tau^m(-\eta_c)K_\tau^m(\eta_2)-K_\tau^m(\eta_c)K_\tau^m(-\eta_2)}{K_\tau^m(\eta_1)K_\tau^m(-\eta_2)-K_\tau^m(-\eta_1)K_\tau^m(\eta_2)}.$$

Here, the charge is located at $\mathbf{x}_c=(\xi_c,\eta_c,0)$, and the constant α_τ^m in (12) is

$$\alpha_\tau^m=\frac{\tau\tanh(\pi\tau)}{\cosh(\pi\tau)}\left[\frac{\Gamma(\frac{1}{2}+i\tau-m)}{\Gamma(\frac{1}{2}+i\tau+m)}\right]^2.\tag{13}$$

Thus the electrostatic potential V (4) is calculated from (6), (7), and (11), and the potential energy Φ is

$$\Phi=q(V_B+V_I),\tag{14}$$

where V_B is given by (6) and V_I by (11). Also, it can be shown[7] that the electric field on the emitter surface at $\eta=\eta_1$, E_1, is

$$E_1=\frac{-2V_0}{a}\frac{1}{\sqrt{\xi^2-\eta_1^2}\sqrt{1-\eta_1^2}}\frac{1}{\ln\left(\frac{1+\eta_2}{1-\eta_2}\frac{1-\eta_1}{1+\eta_1}\right)}+\frac{q}{2\pi a\epsilon_0}\frac{1}{\sqrt{\xi^2-\eta_1^2}\sqrt{1-\eta_1^2}}\cdot\sum_{m=0}^{\infty}(-1)^m(2-\delta_{o,m})$$
$$\times\cos(m\phi)\int_0^\infty d\tau\left[\tau\tanh(\pi\tau)\frac{\Gamma(\frac{1}{2}+i\tau-m)}{\Gamma(\frac{1}{2}+i\tau+m)}[K_\tau^m(\xi_c)K_\tau^m(\xi)]\left(\frac{K_\tau^m(-\eta_c)K_\tau^m(\eta_2)-K_\tau^m(\eta_c)K_\tau^m(-\eta_2)}{K_\tau^m(\eta_1)K_\tau^m(-\eta_2)-K_\tau^m(-\eta_1)K_\tau^m(\eta_2)}\right)\right].\tag{15}$$

Note that the first term in Eq. (15) is the emitter-surface electric field due to the bias potential which is independent of the charge location; the second term is the interaction field produced by the induced surface-charge distributions on the tip and base and the free-charge located at $\mathbf{x}_c=(\xi_c,\eta_c,0)$.

Figure 2 shows computed contour plots of the potential V due to a point charge in a voltage-biased tip–base junction, for both the on-axis and an off-axis case. In both plots: $\eta_1=0.9$ (which corresponds to a tip half-angle of 0.45 radians or 26°); the value of a is chosen so that the radius of the tip at the apex is 20 Å; and the bias voltage of the tip relative to the base is 5 V.

In conclusion, an exact three-dimensional solution for the electrostatic potential due to a charge in a voltage-biased tip/anode junction, modeled in the prolate-spheroidal coordinate system, has been obtained. The results of this study will be used for characterizing the tunneling current at a tip/anode junction using a three-dimensional tunneling analysis, and will be used to carry out a systematic study of off-axis tunneling and its impact on the estimation of active emission areas in nanosized devices.

This work was supported in part by AFOSR Grant No. 49620-92J-0202P00001.

[1] T. E. Sullivan, Y. Kuk, and P. H. Cutler, IEEE Trans. Electron Devices II 31, 2659 (1989).
[2] G. Arfken, *Mathematical Methods for Physicists*, 2nd ed. (Academic, New York, 1970), pp. 103–106.
[3] P. H. Cutler, J. He, J. Miller, N. M. Miskovsky, B. Weiss, and T. E. Sullivan, Prog. Surf. Sci. 42, 169 (1993).
[4] J. He, P. H. Cutler, N. M. Miskovsky, T. E. Feuchtwang, T. E. Sullivan, and M. Chung, Surf. Sci. 246, 348 (1991).
[5] E. W. Hobson, *Theory of Spherical and Ellipsoidal Harmonics* (Chelsea, New York, 1965).
[6] R. G. van Nostrand, J. Math. Phys. 33, 276 (1954).
[7] V. J. Peridier, L. H. Pan, and T. E. Sullivan (unpublished).

B5137

JAN 11 1995

AN ANALYTICAL SOLUTION FOR MICROTIP FIELD EMISSION CURRENT AND EFFECTIVE EMISSION AREA

J. D. Zuber, T.E. Sullivan, Li-Hong Pan
Department of Electrical Engineering
Temple University
Philadelphia, PA 19122

Vallorie J. Peridier
Department of Mechanical Engineering
Temple University
Philadelphia, PA 19122

Paul H. Cutler
Department of Physics
The Pennsylvania State University
University Park, PA 16802

Abstract

Classical field emission theory is based on the one-dimensional planar Fowler-Nordheim theory which relates current density to the applied constant electric field at the emitter surface. However, in the actual non-planar, tip-anode geometry the electric field varies along the microtip surface, giving rise to a spatially dependent current density. This paper accounts for the electric field and the current density variations along a microtip and derives analytical expressions for tip current and emission area. Calculations for current density and total tip current are carried out using an exact three-dimensional electric field solution in prolate spheroidal coordinates in conjunction with the classical Fowler-Nordheim emission theory. The numerical results provide a physical context for the often used field enhancement factor β through the use of exact analytical expressions.

requires an exact three-dimensional solution for the electrostatic potential both at the emitter surface and in the adjoining free space region between emitter and anode.

One approach often taken for adapting the one-dimensional Fowler-Nordheim analysis to inherently three-dimensional structures, is to model the surface electric field as some constant times the applied voltage V, i.e. $F=\beta V$. Here, the parameter β or field enhancement factor is often modelled as a function of the tip geometry. For example, one model for the field enhancement factor is $\beta=1/kr$, where r is the microtip radius of curvature and k is a factor to be empirically determined [2]. β factors are routinely reported which provide reasonable fits of current/voltage data to the Fowler-Nordheim equation, assuming $F=\beta V$ [2,3]. Alternative approaches have also been tried to fit Spindt-emitter data using a model which involved two empirically determined factors, β and γ, to relate the electric field quantity F to the gate and collector voltages, respectively [4].

Theoretical difficulties for the field enhancement factor are known to arise in the context of extremely sharp tips ($r<100$ Å). For example, the Fowler-Nordheim analysis has built-in assumptions concerning the electron supply function and induced surface charge, assumptions which are predicated on a planar, semi-infinite medium emission surface; for the case of extremely sharp tips either the radius of curvature or the physical dimension of the tip may violate such assumptions [5]. An additional conceptual

difficulty with the field enhancement approach is that generally the field is treated as a constant over the entire emission surface. Recognizing this, a more recent theoretical analysis has endeavored to quantify β by modeling the apex of the microtip as a floating sphere [6].

A principal restriction of the field enhancement concept for adapting the Fowler-Nordheim to three dimensional structures remains; that is, a calculation of tunnel current cannot be obtained *a priori* for a given physical system because an empirical estimate of β is required. Thus, although the β factor provides a convenient scheme for the comparison of experimental data, it is strictly an empirically determined quantity. What is desired here is a conceptual framework which permits an estimate of tunnel current, in the context of the Fowler-Nordheim analysis, from first principles; that is the objective addressed in this paper.

The work described in this paper offers a scheme to evaluate the performance of field emission microtips from first principles, in the context of the Fowler-Nordheim theory, without the need of an empirically determined β factor. This objective has been achieved by the use of an exact, fully three-dimensional solution for the electric field in a microtip/base junction [7]. This geometry models the microtip and anode as hyperboloid surfaces, and obtains an exact solution for several fully, three-dimensional electrostatic quantities due to a free charge in a tip/base junction, in the prolate-

spheroidal coordinate system. To fully appreciate the significance of this model it is worthwhile to consider Figures 1 & 2. Figure 1 shows: (a) a tip modeled as a constant-radius structure (such as that idealized in the floating-sphere model), the dotted line, and (b) the tip modeled as a hyperboloid surface, the solid line. In Figure 2 a transmission electron micrograph (TEM) of a fabricated silicon tip is reproduced [8], overlaid by the two models given in Figure 1. It is self-evident that the hyperboloid surface offers an excellent physical approximation for the geometrical features of a field emission microtip, and such agreement motivated the utilization of the exact prolate spheroidal solution for the electric field to quantify the emission characteristics of microtips.

The methodology adopted in this paper is as follows. The exact solution for the electrostatic field of the microtip/base junction given by the prolate spheroidal model is substituted into the Fowler-Nordheim equation, yielding an analytic expression that describes the tunnel current density at every point on the surface. The total tip current is then obtained by integration of this current density expression over the surface of the microtip. The current density on the tip surface decays rapidly with the distance from the tip apex. Using this result, we have been able to develop an estimation scheme for the effective emission area of the tip.

II. Electric Field Derivation

The derivation for the electric field on a microtip surface, in a biased tip/base junction as modeled in a prolate spheroidal geometry, is given in [7]. The prolate spheroidal coordinate system shown in Figure 3 is defined by the coordinates ξ, η, and ϕ [7] where $\xi \in [1,\infty)$, $\eta \in [\eta_2,\eta_1]$, $\phi \in [0,2\pi]$. η_1 corresponds to the hyperboloidal surface of the tip, η_2 is the planar anode surface, lines of constant ξ define prolate spheroidal surfaces, and ϕ is the azimuthal angle of rotation about the symmetry or major axis. Other key parameters of interest include the foci distance of 2a, the tip-anode distance d, and the tip half angle θ. These three parameters are related by the expression $\theta=\cos^{-1}(d/a)$. The tip radius r on axis is defined as $r=a \sin\theta \tan\theta$.

If a voltage V_0 is applied between the tip and anode, the Laplace equation, $\nabla^2 V=0$, must be satisfied. In prolate spheroidal coordinates, the Laplacian is given by:

$$\nabla^2=\frac{1}{a^2(\xi^2-\eta^2)}\left[\frac{\partial}{\partial\xi}\left((\xi^2-1)\frac{\partial}{\partial\xi}\right)+\frac{\partial}{\partial\eta}\left((1-\eta^2)\frac{\partial}{\partial\eta}\right)+\frac{\xi^2-\eta^2}{(\xi^2-1)(1-\eta^2)}\frac{\partial^2}{\partial\phi^2}\right] \quad (1)$$

Setting $V(\eta_1)=0$ at the tip and $V(\eta_2)=V_0$ at the anode, the electrostatic potential is symmetric in ξ and ϕ and thus is independent of ξ and ϕ, so that the solution for V is:

$$V(\eta) = V_0 \frac{\ln\left[\left(\frac{1+\eta}{1-\eta}\right)\left(\frac{1-\eta_1}{1+\eta_1}\right)\right]}{\ln\left[\left(\frac{1+\eta_2}{1-\eta_2}\right)\left(\frac{1-\eta_1}{1+\eta_1}\right)\right]} \tag{2}$$

The field $F(\xi)$ at any point on the surface of the tip is determined from the negative gradient of $V(\eta)$. $F(\xi)$ is a vector with components in the ξ and ϕ directions equal to zero. The resulting magnitude of $F(\xi)$ in the η direction is:

$$F(\xi) = \frac{-2V_0}{a} \frac{1}{\sin(\theta)\sqrt{\xi^2-\cos^2(\theta)}\ \ln\left(\frac{1-\cos(\theta)}{1+\cos(\theta)}\right)} \tag{3}$$

where $\cos(\theta)$ has been substituted for η [9]. Note that θ is the cone angle of the microtip, with $\theta \rightarrow \pi/2$ a very flat tip, and $\theta \rightarrow 0$ an extremely sharp tip. Note also that ξ in effect measures the distance on the top surface from the apex, with $\xi=1$ the apex ordinate.

III. Implications for Field-Enhancement Factor

It is possible to substitute an expression in r, the radius of curvature at the apex, for the parameter a and put $F(\xi)$ in a form that follows the field enhancement concept $F=\beta V$, where β is expressed as $\beta=1/kr$.

$$F(\xi)=\frac{V_0}{r}\frac{-2\tan(\theta)}{\sqrt{\xi^2-\cos^2(\theta)}\ \ln\left(\frac{1-\cos(\theta)}{1+\cos(\theta)}\right)} \tag{4}$$

With $F(\xi)$ in this form a field enhancement factor defined by k, would be expressed as:

$$k(\xi)=\frac{\sqrt{\xi^2-\cos^2(\theta)}\ \ln\left(\frac{1-\cos(\theta)}{1+\cos(\theta)}\right)}{-2\tan(\theta)} \tag{5}$$

Asymptotic analysis may be used to show that $k>>1$ in the limit of very sharp tip ($\theta\rightarrow 0$), and that $kr\rightarrow d$ in the limit of very blunt tips ($\theta\rightarrow\pi/2$, $\xi\rightarrow 1$). This means that as the tip broadens to become a planar surface; the geometry appears as two parallel plates and the β factor approaches the expected limiting value 1/d.

IV. Tip Current Calculation

The most general form of the Fowler-Nordheim equation is [10]:

$$j(F) = \frac{e^3 F^2}{8\pi h \psi t^2\left(\sqrt{\frac{e^3 F}{\psi}}\right)} \exp\left[\frac{-8\pi\sqrt{2m}\psi^{\frac{3}{2}}}{3heF} v\left(\frac{\sqrt{e^3 F}}{\psi}\right)\right] \qquad (6)$$

In this expression F is the electric field (V/cm), ψ is the material work function (eV), h is Planck's constant (erg-sec), e is the electron charge (stat-coul), j is the current density (amp/cm^2), and m is the electron mass (gm).

The v function is dependent on an involved composition of elliptic integrals and varies from 1 to 0 as electric field strength increases [10]. The t^2 function is a slowly varying -function of the applied field and is approximated as 1.1 [10]. In order to avoid calculations with the integrals that define v, an approximation that has been made is [11]:

$$v(F) = 0.95 - y(F)^2 \qquad y(F) = 3.79 x 10^{-4} \frac{\sqrt{F}}{\psi} \qquad (7)$$

Using this approximation and substituting the values for t^2 and the constants, the equation can be expressed in CGS units:

$$j(F) = \frac{1.54x10^{-6}F^2}{1.1\psi}\exp\left[\frac{-6.83x10^7\psi^{\frac{3}{2}}}{F}[0.95-y(F)^2]\right] \qquad (8)$$

This form of the equation uses electric field values in volt/cm. Converting the field values to volt/Å the equation can be written as:

$$j(F) = AF^2\exp\left[-\frac{B}{F}\right] \qquad (9)$$

where the constants A and B are given by:

$$A = \frac{1.54x10^{10}}{1.1\psi}\exp\left[\frac{9.811}{\sqrt{\psi}}\right] \qquad B = 0.649\psi^{\frac{3}{2}} \qquad (10)$$

The Fowler-Nordheim equation developed above provides for the current density j(F) measured in amps/cm^2 for the case of a planar geometry and a constant electric field. In comparison, the prolate spheroidal electric field F(ξ) varies with ξ, the dimensionless distance from the apex of the microtip, where the field F is greatest.

Unlike the one-dimensional analysis where the field is constant both on the surface and in the adjoining free space, the three-dimensional nature of $F(\xi)$ yields a spatially variable electric field both on the surface and in the adjoining free space. If we imagine the tip to be composed of numerous, infinitesimal planar segments of area $d\xi d\phi$ distributed in a manner similar to the marks on a golf ball, we can apply the Fowler-Nordheim equation on each planar segment and then integrate the resulting $j(\xi)$ over the microtip surface to obtain tip current, where ξ_0 is the upper limit of ξ that defines the effective emission area; the systematic selection criterion for the ξ_0 cutoff value is described below.

$$j(\xi) = AF(\xi)^2 \exp\left[-\frac{B}{F(\xi)}\right] \tag{11}$$

$$i(d, V, \theta, \psi) = \int_0^{2\pi}\int_1^{\xi_0} 10^{-16} j(\xi)\, h_\phi(\xi)\, h_\xi(\xi)\, d\xi\, d\phi \tag{12}$$

The tip current i is explicitly shown as a function of various parameters, and the functions h_ϕ and h_ξ are prolate spheroidal metrics [9]. Substitution of the various functions in (16) and simplifying leads to the expression:

$$i(d, V, \theta, \psi) = x(\theta, \psi)\ V^2 \int_1^{\xi_0} \frac{\exp\left[\frac{y(d, \theta, \psi)}{V}\sqrt{\xi^2 - \cos^2(\theta)}\right]}{\sqrt{\xi^2 - \cos^2(\theta)}}\, d\xi \tag{13}$$

where the functions x and y are defined as:

$$x(\theta,\psi) = \frac{3.5186x10^{-5}\ \exp\left(\frac{9.811}{\sqrt{\psi}}\right)}{\psi\ \sin(\theta)\ \ln\left(\frac{1-\cos(\theta)}{1+\cos(\theta)}\right)^2} \tag{14}$$

$$y(d,\theta,\psi) = 0.3245\ d\ \psi^{\frac{3}{2}} \tan(\theta) \ln\left(\frac{1-\cos(\theta)}{1+\cos(\theta)}\right)$$

Numerical results based on the above method have been selected and the corresponding curves for electric field, current density, and tip current are plotted in Figures 4-6. It is significant to notice how quickly the current density is reduced as a function of ξ, the distance along the surface from the tip axis. Various sets of calculations have been done for other values of V, d, and θ, including the limiting geometries of a very sharp tip and a tip so blunt that it approximates a flat plane.

In those cases where the value of ξ in the region of electron emission remains close to 1, the tip current integral of (13) can be very closely approximated as:

$$i(d,V,\theta,\psi) = \frac{x\ V^3}{y}\left[\exp\left(\frac{y}{V}\sqrt{\xi_0^2-\cos^2(\theta)}\right)-\exp\left(\frac{y}{V}\sin(\theta)\right)\right] \tag{15}$$

This equation provides the value of tip current in amperes for a geometry specified by d and θ, and for an effective emission area defined by the range $\xi = \in [1, \xi_0]$.

V. Effective Emission Area

Calculations for the tip current indicate that most of the current is due to the tip area that is very close to the tip axis. The numerical results show that 99.9% of the tip current is from an area where current density has decayed to 3 orders of magnitude below the current density peak located on axis. This lower limit of 3 orders of magnitude reduction in current density will be used in a derivation of the effective emission area.

The value of ξ at which the current density is reduced by a factor of 10^{-3} is given by:

$$\frac{j(\xi)}{j(1)} = 10^{-3} \qquad (16)$$

The pre-exponential terms for $j(\xi)$ and $j(1)$, from equation (11), effectively cancel for values of ξ close to 1, and the exponential terms determine the value of ξ which satisfies (16). Performing this operation and solving for ξ yields the following expression:

$$\xi_0 = \sqrt{\left[\frac{-21.287\ V}{\psi^{\frac{3}{2}}\ d\tan(\theta)\ \ln\left(\frac{1-\cos(\theta)}{1+\cos(\theta)}\right)} + \sin(\theta)\right]^2 + \cos^2(\theta)} \qquad (17)$$

This expression defines the proper ξ_0 for use in the current equation shown in (15). In the case (b) of the parameters selected for the figures, the value of ξ_0 is 1.0068. With the substitution of (17) into (15) and simplifying, the equation for tip current can be expressed as:

$$i(d, V, \theta, \psi) = \frac{-x\ V^3}{y}\left[\exp\left(\frac{y}{V}\sin(\theta)\right)\right] \qquad (18)$$

Similarly, (17) can now be used to calculate the effective emission area:

$$A(d, \theta, \xi_0) = \int_0^{2\pi}\int_1^{\xi_0} h_\phi(\xi)\, h_\xi(\xi)\, d\xi\, d\phi \qquad (19)$$

$$A(d, \theta, \xi_0) = \frac{\pi d^2\ \tan(\theta)}{\cos(\theta)}\xi_0\sqrt{\xi_0^2 - \cos^2(\theta)} - \pi d^2 \sin(\theta)\ln\left(\xi_0 + \sqrt{\xi_0^2 - \cos^2(\theta)}\right)$$

$$-\pi\ d^2\tan^2(\theta) + \pi d^2 \sin(\theta)\ln[1+\sin(\theta)]$$

In the case (b) of the parameters selected for the figures, the effective emission area is 32,706 Å^2.

VI. Comparisons with Experimental Determinations of Beta

The expression for a local β, the field enhancement factor associated with the expression $F(\xi)$, is:

$$\beta(\xi) = \frac{-2}{a \sin(\theta) \sqrt{\xi^2 - \cos^2(\theta)} \ln\left(\frac{1-\cos(\theta)}{1+\cos(\theta)}\right)} \qquad (20)$$

The local beta factor is dependent only upon the geometry of the tip defined by the tip half angle θ and the foci distance a, and varies along the surface of the tip with values of ξ. Figure 7 exhibits this behavior by displaying the inverse of the beta factor versus ξ, for a range of selected on axis tip radii. Note that the value of β^{-1} converges to the parallel-plate value of the tip-anode distance d in the limit as the tip radius approaches infinity.

The following experimental estimates for an averaged, global tip value for β, as given by several investigators, are in close agreement with the results shown in Figure 7.

Year	Researcher	Tip Radius	β value	Reference
1953	Dyke/Trolan	18 μm	12,800 cm^{-1}	[12]
1993	Jenkins	~10 nm	636,000 cm^{-1}	[13]
1994	Hong *et al.*	~25 nm	210,000 cm^{-1}	[14]

VII. Conclusions

The use of the prolate spheroidal tip/anode model [7] allows for the exact representation of the bias electric field and is used, in conjunction with classical Fowler-Nordheim theory [1] to calculate surface varying electric field tunnel current densities, net tip current, and effective emission area. Because the prolate spheroidal coordinate system is such a close geometrical approximation to the tip-to-plane geometry, our microtip calculations within that system possess an unexpected simplicity.

It has been suspected for years that the β factor is only geometry dependent, and data has shown it to be of constant value. The exact field solution in prolate spheroidal coordinates largely corroborates those assertions. As derived for a single microtip the β factor is solely dependent on geometry; it does not vary with any electrical operating characteristics.

Close examination of Figure 7 reveals that experimentation with microtips of radii 250-400 Å (e.g., Spindt tips) would observe a nearly constant β factor. As researchers find ways to create microtip arrays with an average of tip radii approaching 50 Å, they may begin to observe a non-constant value for β.

In the derivation of the prolate spheroidal tip current, the exact solution for the electric field $F(\xi)$ was substituted into the classic, planar Fowler-Nordheim equation for current

density, and we imagined the tip as numerous planar segments of area $d\xi d\phi$. In reality, as the electron tunnels from the surface, it does not experience a completely flat surface as assumed by the Fowler-Nordheim theory. However, the implicit assumption here is that the surface appears approximately planar as long as the local radius of curvature for the surface is larger than the tunnel distance of the electron.

REFERENCES

[1]R.H. Good Jr. and E.W. Muller, *Handbuch der Physik*, XXI, Springer, 192, (1956).

[2]Brodie and C.A. Spindt, *Vacuum Microelectronics*, Academic Press Inc., New York, 14, (1992).

[3]W.P. Dyke, Sci. Am., 210-1, 108, (1964).

[4]David W. Jenkins, IEEE Trans. Electron Devices, ED-40, 666, (1993).

[5]Jun He, Theory of Electron Emission from Atomically Sharp Metallic Emitters in High Electric Fields, The Pennsylvania State University, iv (1992).

[6]Dan Nicolaescu, J. Vac. Sci. Technol. B 11, 392, (1993).

[7]L.H. Pan, T.E. Sullivan, V.J. Peridier, P.H. Cutler, and N.M. Miskovsky, Appl. Phys. Letters, 65 (17), 2151-2153 (1994).

[8]Photograph courtesy of R.B. Marcus.

[9]G. Arfken, *Mathematical Methods for Physicists*, Academic Press Inc., New York, 103-106, (1970).

[10]R.H. Good Jr. and E.W. Muller, 188.

[11]C.A. Spindt, I. Brodie, L. Humphrey, and E.R. Westerberg, J. Appl. Phys. 47, 5250, (1976).

[12]W.P. Dyke and J.K. Trolan, Physical Review 89 (4), 805, (1953).

[13]David W. Jenkins, 670.

[14]D. Hong, M. Aslam, M. Feldman, and M. Olinger, J. Vac. Sci. Technol. B 12, 767, (1994).

CAPTION PAGE

Figure 1. Comparison of prolate spheroidal and constant radius tip geometries.

Figure 2. Comparison of prolate spheroidal and constant radius tip geometries with a microtip transmission electron micrograph (TEM) overlay.

Figure 3. Prolate spheroidal coordinate system.

Figure 4. Electric field vs. ξ for a prolate spheroidal tip with d=10000 Å, a=10025 Å, ϕ=4.7 eV, and voltages (a) V=100 volts, (b) V=150 volts, (c) V=200 volts.

Figure 5. Current density vs. ξ for a prolate spheroidal tip. d=10000 Å, a=10025 Å, ϕ=4.7 eV, and voltages (a) V=100 volts, (b) V=150 volts, (c) V=200 volts.

Figure 6. Tip current vs. ξ for a prolate spheroidal tip. d=10000 Å, a=10025 Å, ϕ=4.7 eV, and voltages (a) V=100 volts, (b) V=150 volts, (c) V=200 volts.

Figure 7. β^{-1} vs. ξ for a prolate spheroidal tip with d=10000 Å, and selected values of the on axis tip radius r. (a) r=10 Å, (b) r=50 Å, (c) r=200 Å, and (d) r=1025 Å, (e) r=∞.

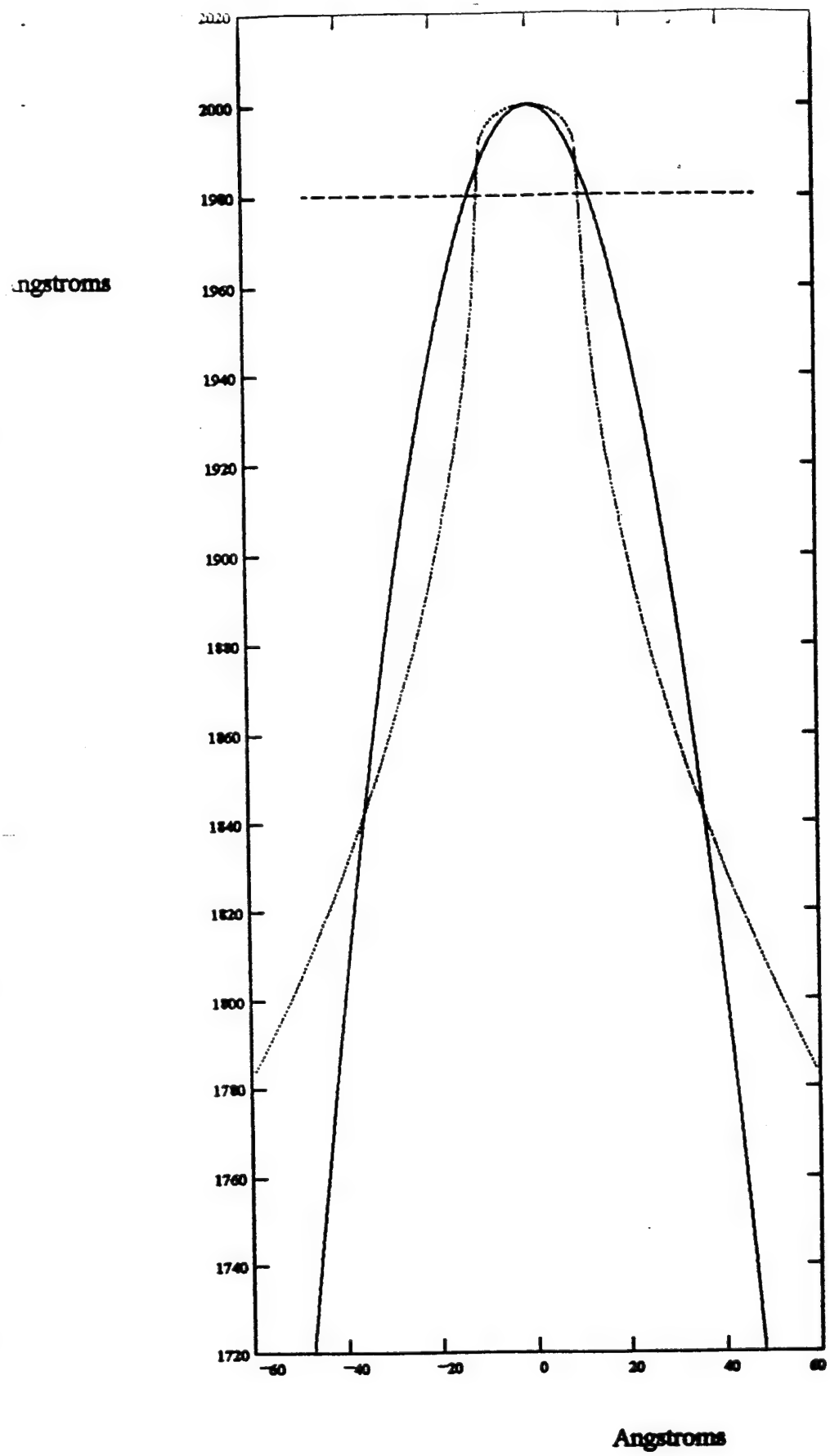
ngstroms
2020
2000
1980
1960
1940
1920
1900
1880
1860
1840
1820
1800
1780
1760
1740
1720
-60
-40
-20
0
20
40
60
Angstroms

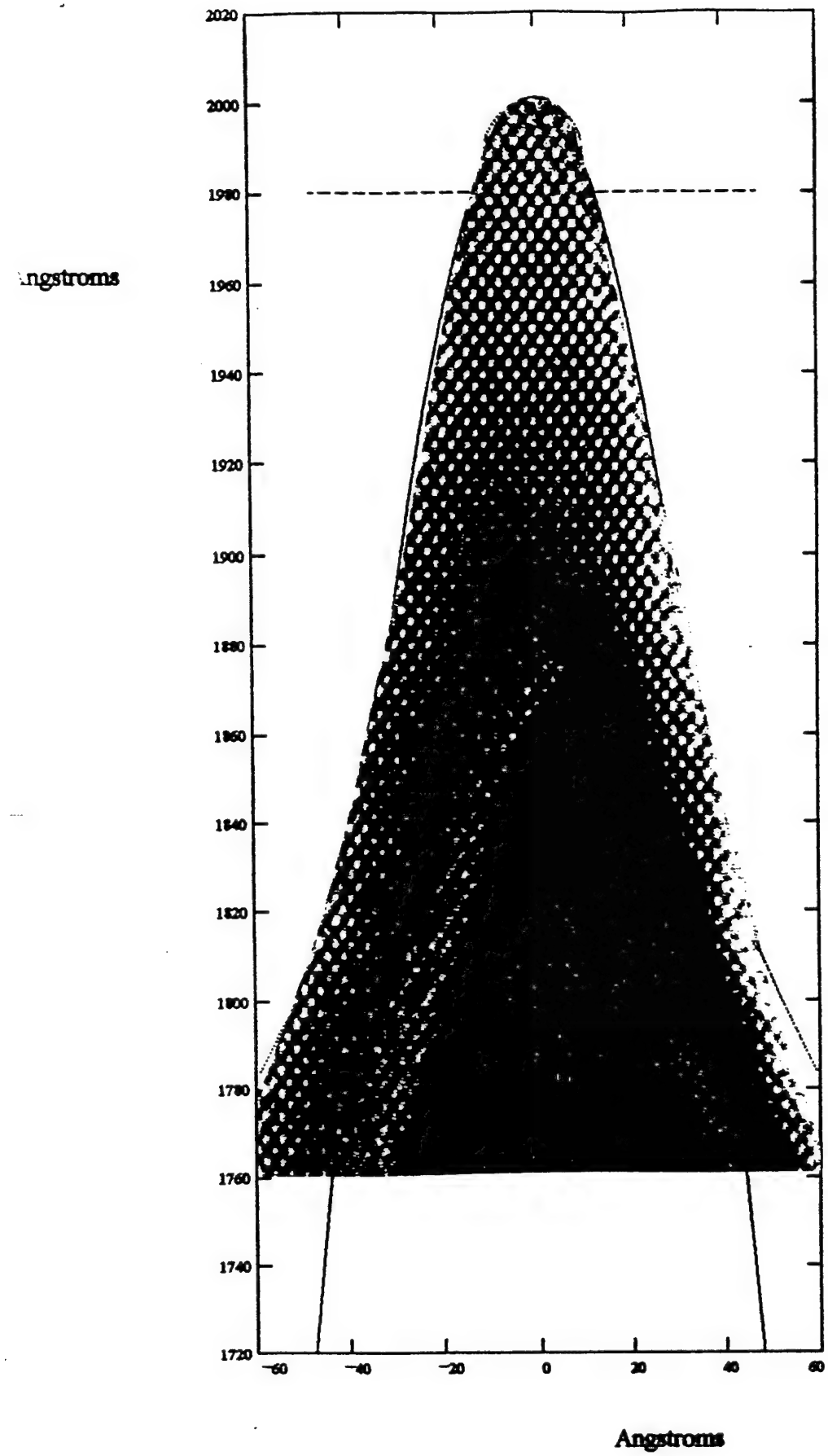
ngstroms
2020
2000
1980
1960
1940
1920
1900
1880
1860
1840
1820
1800
1780
1760
1740
1720
-60
-40
-20
0
20
40
60
Angstroms

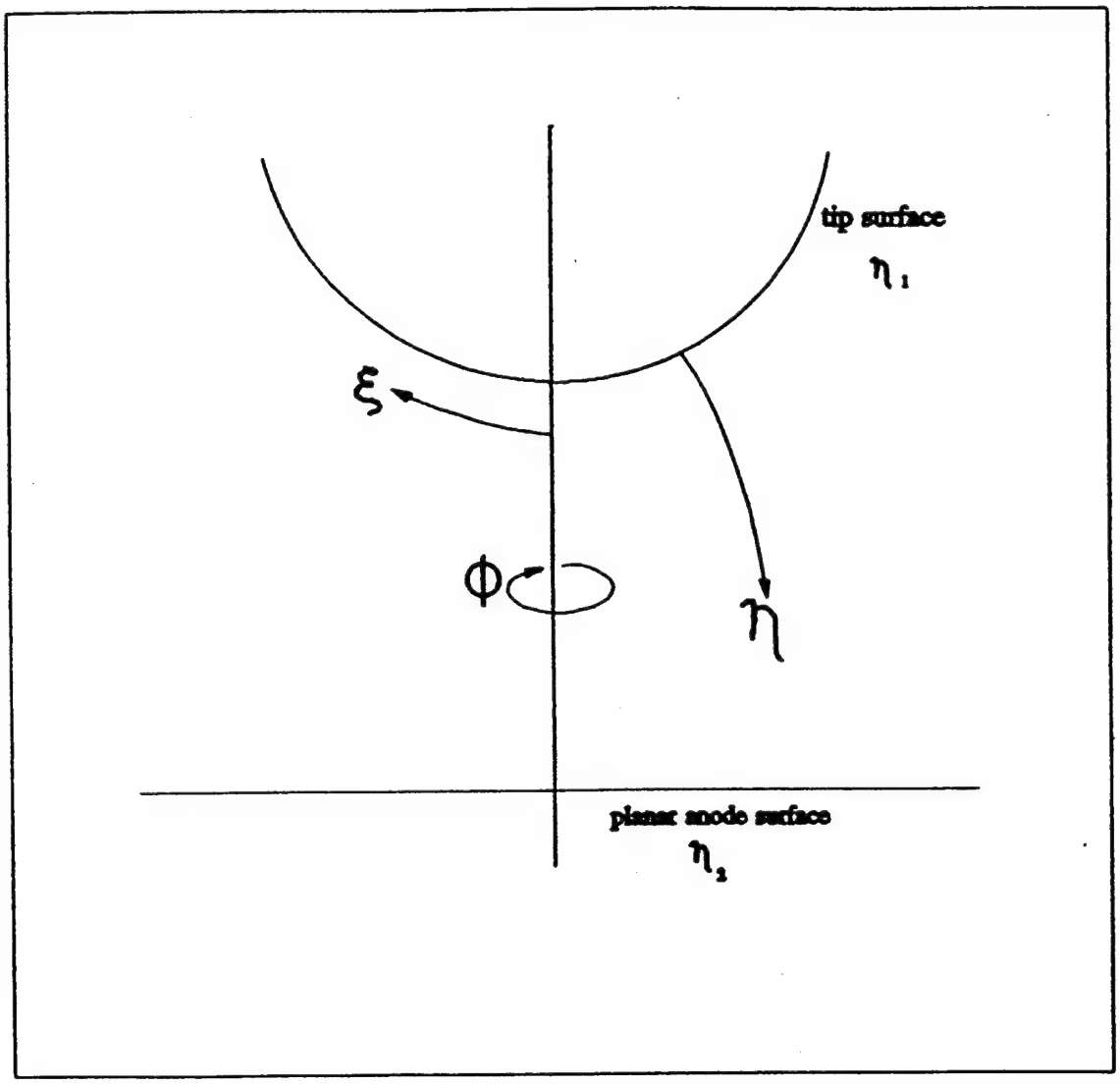
tip surface
η_1
ξ
ϕ
η
planar anode surface
η_2

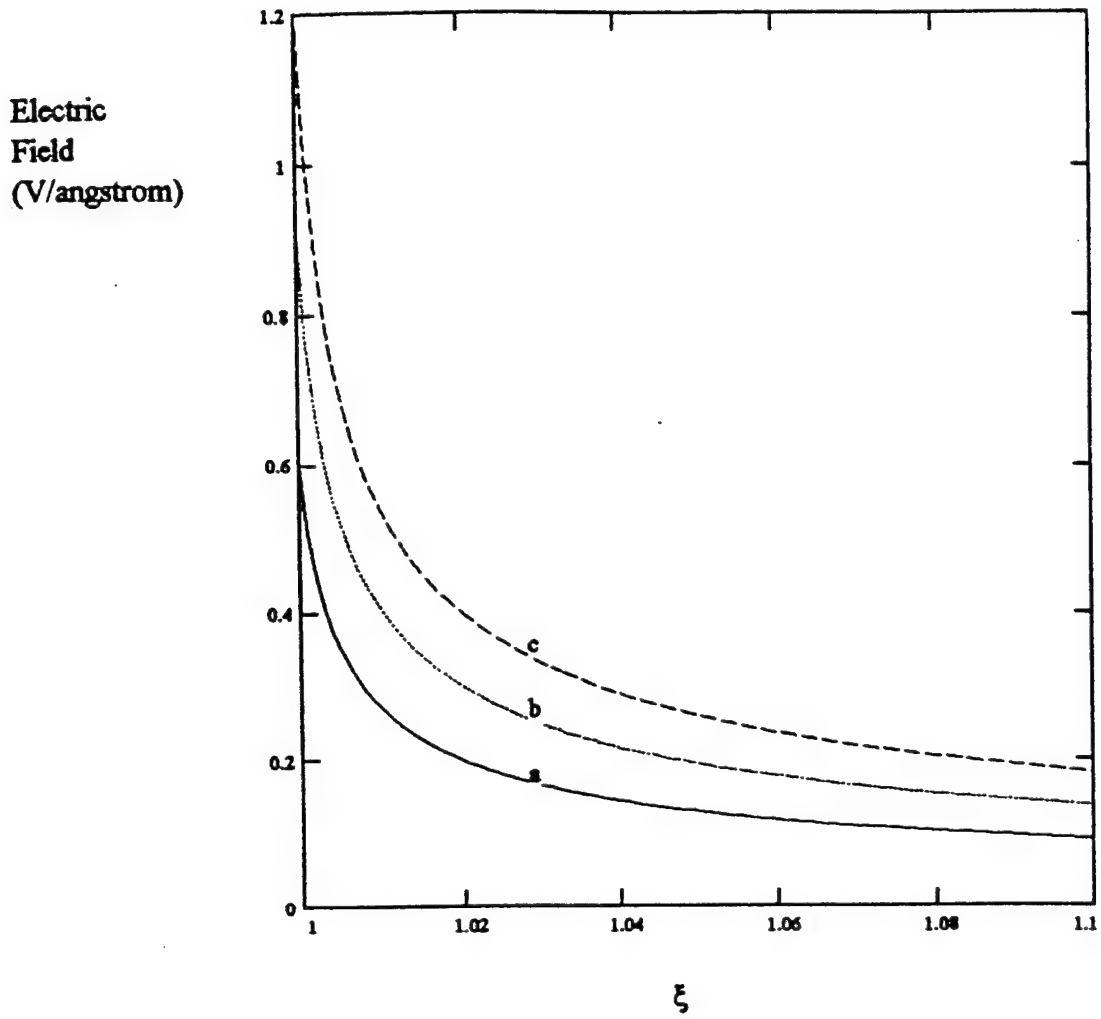
Electric
Field
(V/angstrom)
1.2
1
0.8
0.6
0.4
0.2
0
1
1.02
1.04
1.06
1.08
1.1
c
b
a
ξ

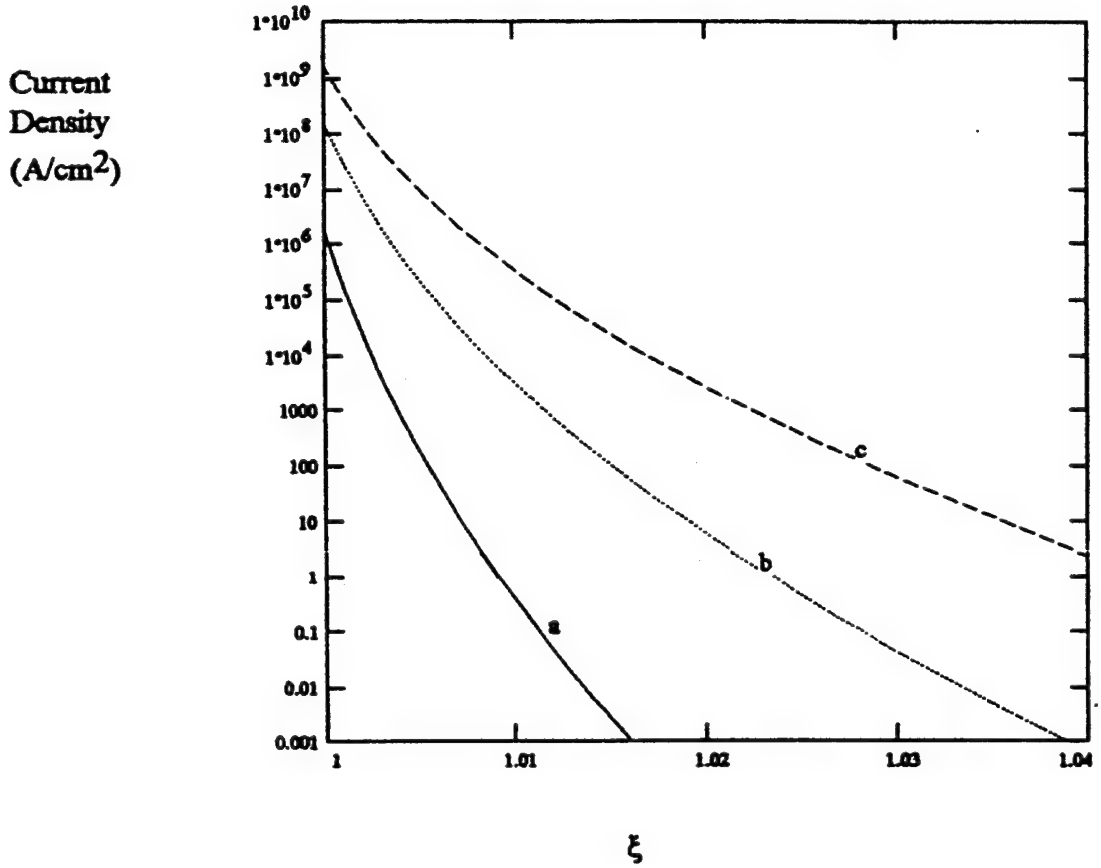
Current
Density
(A/cm2)
1*10^10
1*10^9
1*10^8
1*10^7
1*10^6
1*10^5
1*10^4
1000
100
10
1
0.1
0.01
0.001
1
1.01
1.02
1.03
1.04
a
b
c
ξ

Tip
Current
(A)

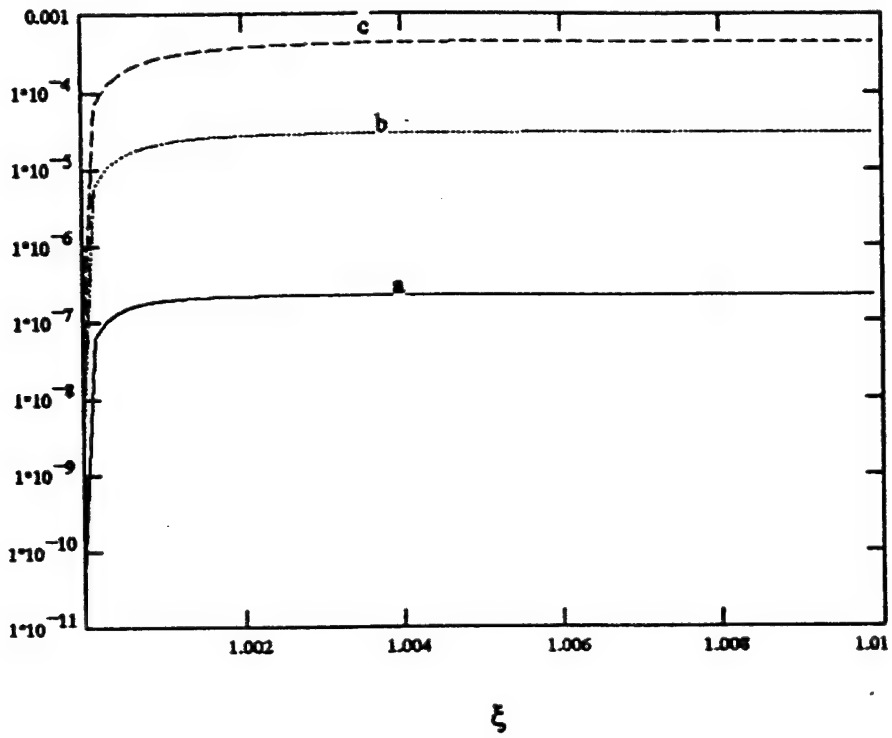

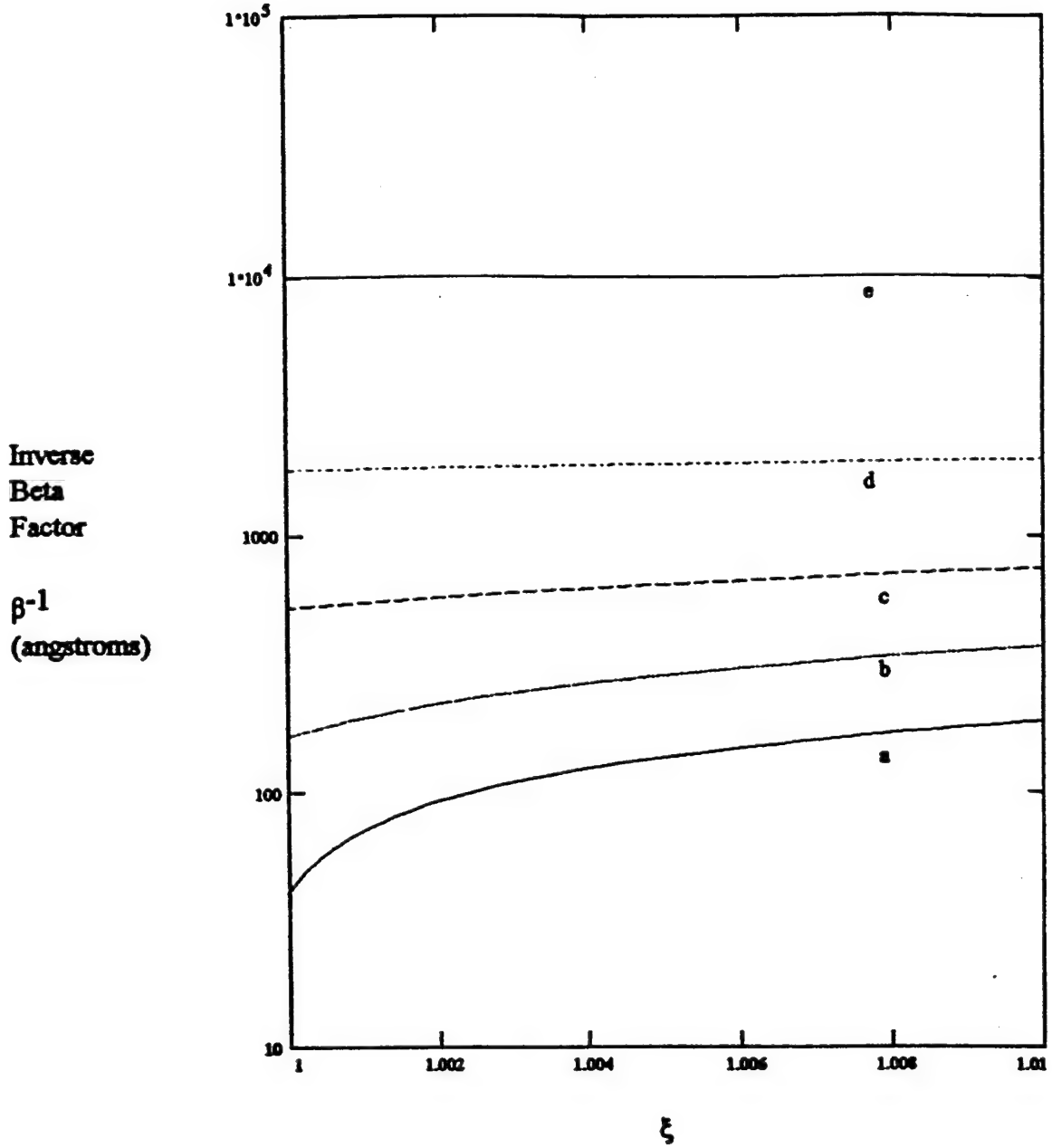
Inverse
Beta
Factor
β-1
(angstroms)
1·10^5
1·10^4
1000
100
10
1
1.002
1.004
1.006
1.008
1.01
ξ
a
b
c
d
e

Appendix C

JAN 11 1995

5136

STATISTICAL EFFECTS OF TIP RADIUS VARIATION ON CURRENT EMISSION IN FIELD EMISSION ARRAYS

J. D. Zuber, T.E. Sullivan
Department of Electrical Engineering
Temple University
Philadelphia, PA 19122

Vallorie J. Peridier
Department of Mechanical Engineering
Temple University
Philadelphia, PA 19122

Paul H. Cutler
Department of Physics
The Pennsylvania State University
University Park, PA 16802

Abstract

Process variation inherent in the fabrication of field emitter arrays leads to microtip radii variations which can significantly affect the device characteristics of vacuum field emitters. This paper treats the tip radius as a random variable and examines the effect of tip radius variation on current emission within the Fowler-Nordheim theory. The dominance of the sharpest tips in an array is quantified by using examples of arrays with Gaussian and Rayleigh tip radius probability density functions (pdf). It is proposed that the Rayleigh pdf may be a good model for the real tip radius variation. Some expected values for tip current are tabulated for a variety of statistical parameters.

I. Introduction

The successful application of field emitter arrays (FEA) as flat panel displays and their potential application in radio frequency (rf) generation and amplification has spurred interest in the yield-limiting mechanisms and the reliability of these devices.

Field emitter arrays must perform their function to electrical specifications, such as the total array current and gating frequency, throughout their intended lifetimes. An important issue for the utilization of FEAs is the statistical variability in fabrication that causes the electrical parameters to vary from emitter to emitter [1-4]. These observations show that all of the emitters within an array may not function or that a few of the emitters are producing most of the observed current while others are emitting at a much lower current level.

In a properly fabricated array all of the emitters are expected to be fully functional. There are, however, yield loss mechanisms that limit the total number of fully functional devices. These loss mechanisms typically fall into three categories. The first two are circuit design problems and random point defects attributed to dust or particulate fallen on the device area during fabrication. The third yield loss mechanism is the one addressed in this paper, namely, the parametric processing variability.

In this paper we examine the effects of statistical process variability on the emission current. We treat the tip radius, r, as a random variable with a Normal (Gaussian) or a Rayleigh pdf. The pdf for the emission current is subsequently derived.

The results presented here clarify previous observations that current emission comes from only a few tips in an array. More importantly, tip current expected values are shown for some selected array parameters based on the generally accepted Fowler-Nordheim theory for tunneling current.

II. Parametric Process Variability

The fabrication of field emission arrays (FEA) is subject to the same process variation inherent in all integrated circuit processes running under statistical process control. Processing latitude in photolithography, wet chemical or plasma etching, and metal or dielectric deposition conditions all contribute to the variability of geometric features on the wafer. These process control variances lead to FEA feature size variability within an array, from array to array within a wafer, and from wafer to wafer.

The highly nonlinear current-voltage (I-V) characteristics of FEA devices, using either the classic planar Fowler-Nordheim or the non-planar hyperboloidal tip models [5,6], magnify the effects of process variations as seen in the measured I-V relationship. One

such example is the dependence of the surface field on the tip radius of curvature. The fabrication process steps, with their respective variances leading to the completed geometry of the tip radius, will each contribute variation to the final geometric shape of the tips. Hence, the variation in tip radii for the final structure is a function of one or more independent variations due to the individual processing steps. The independence of the process variances can be seen from the independence of the steps themselves.

As an example, consider that a target feature size formed in photoresist depends on the thickness of the photoresist, the exposure dosage, and the development time used to form the desired image. Once the image is formed and the exposed photoresist is removed, the image of the desired feature is transferred to the wafer. The final geometrical feature, however, has not yet been formed. Due to variations in the photolithographic steps, the image formed across the wafer surface exhibits variation. The geometrical feature, as an example the gate opening, is then formed by plasma or wet chemical etching. There already exists a variation in the photoresist pattern due to photolithographic processes. Superimposed on top of that photolithographic variation is the statistically independent variation due solely to the plasma or wet etching itself which can originate from diffusion effects in the etchant chemical, or pressure and power variations in the case of plasma processing.

The statistical variation of a feature in an array must often be determined by optical, scanning electron micrograph (SEM), or transmission electron micrograph (TEM) inspections. These exhaustive in-process inspections carried out during device fabrication are time consuming and expensive. The most easily acquired statistical data on arrays is obtained by using computer controlled testing of the I-V relationship for completed devices. On these devices the overall effects of the combined process variations give rise to variations in the measured I-V data. Testing of individual devices and arrays of devices is performed by computer controlled parametric testers which record the data and can display it in statistical form.

When seen from the perspective of the completed and tested devices, the formal problem in this case is the relationship between the statistical variation in the measured I-V data for individually sampled devices and the variation in a critical geometric feature within the device. The formal analysis developed here can be extended to predict a statistical variation necessary to meet a total current specification for a system.

III. Fowler-Nordheim Theory for Microtips

Relating the electric field at the surface of a sharp tip to the tip radius and to the applied voltage has received considerable attention. Much of the theoretical work [7] has adopted the relationship $F=\beta V$, where F is the electric field at the emitter surface and

V is the applied voltage. The β factor, either constant or dependent on the radius r, is used to account for the particular tip geometry in the otherwise one dimensional Fowler-Nordheim analysis [8]. One theoretical analysis [9], undertaken to fit experimental data based on the Spindt emitter, used a model that involved two empirically derived factors to relate the electric field to the separate gate and collector voltages. Another effort in modeling [10] indicated that the β factor approach may be reasonable for tips with a radius that is greater than 100 angstroms, but in the case of atomically sharp tips the β factor may be an over-simplification [8]. A more recent analysis [11] used a floating sphere model (FSM) and derived a formula for the β factor based on geometrical considerations. Despite the recent discussions regarding the theoretical necessity for the β factor, it is still widely used as a common basis for comparison of experimental results.

In the analyses that follow, the focus is on the tip-to-tip radius variation in an array and how that variation affects both the tip and aggregate array current. For the purpose of these calculations the β factor will be defined as $\beta(r)=1/kr$. The k term is a geometric factor and the r dependence provides a β value that increases with decreasing radius and yields greater field enhancement than a constant β value. The k term will be assumed to have a constant value. The electric field and radius relationship can now be used in the Fowler-Nordheim equation to calculate the current density for a tip. In those cases where β is defined differently from $\beta(r)=1/kr$, the explicit dependence of β on the

geometrical feature size, r, is incorporated in the expression for the current density j(r). The derivation of the current probability density function then proceeds in the same manner.

The most general form of the Fowler-Nordheim equation is [12]:

$$j(F)=\frac{e^3F^2}{8\pi h\phi t^2\left(\sqrt{\frac{e^3F}{\phi}}\right)}\exp\left[\frac{-8\pi\sqrt{2m}\phi^{\frac{3}{2}}}{3heF}v\left(\frac{\sqrt{e^3F}}{\phi}\right)\right] \qquad (1)$$

In this expression F is the electric field (V/cm), ϕ is the material work function (eV), h is Plank's constant (erg-sec), e is the electron charge (stat-coul), and m is the electron mass (gm).

The v function is dependent on an involved composition of elliptic integrals and varies from 1 to 0 as electric field strength increases. The t^2 function is a slowly varying function of the applied field and is approximated as 1.1 [12]. In order to avoid calculations with the elliptic integrals, the function v is approximated by [13]:

$$v(F) = 0.95 - y(F)^2 \qquad y(F)=3.79x10^{-4}\frac{\sqrt{F}}{\phi} \qquad (2)$$

Using this approximation and substituting the values for t^2 and the constants, j(F) can be expressed in amps/cm^2 as:

$$j(F)=\frac{1.54x10^{-6}F^2}{1.1\phi}\exp\left[\frac{-6.83x10^7\phi^{\frac{3}{2}}}{F}[0.95-y(F)^2]\right] \qquad (3)$$

This form of the equation uses electric field values in volt/cm. Replacing the electric field in favor of the applied voltage V and transforming to the radius of curvature in angstroms as the independent variable r, the current density expression becomes:

$$j(r)=\frac{A}{r^2}\exp(-Br) \qquad (4)$$

where the constants A and B for a given V are defined as:

$$A=\frac{1.54x10^{10}V^2}{1.1\phi k^2}\exp\left[\frac{9.811}{\sqrt{\phi}}\right] \qquad B=\frac{0.649\phi^{\frac{3}{2}}k}{V} \qquad (5)$$

IV. Calculation of Total Current

The Fowler-Nordheim equation developed above provides for the current density j(r) in amps/cm^2 for each individual tip with its particular radius. The current from a microtip can be found by multiplying the current density j(r) by the effective emitting area for

that radius. The total current of the FEA is a summation of tip current for all of the individual tips. Although the Fowler-Nordheim and non-planar emission theories express the emission current as a current density, the total emission current from an individual tip or an array is the parameter of interest. As such, we rewrite the current density as a tip current using an appropriately chosen expression for the emission area. There is no general agreement on the calculation of effective emitting area for a microtip. A recent theoretical study [9] used the model of a spherical tip on the end of a cone and calculated the area of emission α_{tip} with a dependence on the emitter tip half angle.

The approach shown in the calculations that follow is to adopt an emission area for the tips that can be viewed as being dependent on the microfabrication procedure used to create the tip. In particular, our experimentation on atomically sharp silicon emitters made use of a technique to isotropically etch silicon while using a silicon dioxide "hat" as a mask. This technique creates concave sides for the microtip structure, and these sides would ideally be perpendicular to the fine tip area at the most upper part of the side wall. Thus, the emission area that is used in the following calculations is the half-spherical shell surface described by $\alpha(r)=2\pi r^2$, where r is expressed in centimeters.

The tip current in amperes can then be expressed as $i(r)=j(r)\alpha(r)$, which yields the following expression:

$$i(r)=2x10^{-16}\pi A \exp(-Br) \qquad (6)$$

The radius r is in angstroms. In most geometrical cases the effective emitting area should scale in proportion to the square of the radius, certainly to a good approximation if not exactly. Therefore, this simplification in the final expression for i(r) should exist in most tip geometries.

V. Current Probability Density Function Derivation

The tip radius can be viewed as a continuous random variable in a given range. This random variable is described by a probability density function (pdf) over that range. If an appropriate tip radius pdf can be determined, then stochastic methods [14] can be used to analyze field emission parameters in light of the Fowler-Nordheim equation and non-planar emission theories [5,6].

We considered two arrays of microtips in which the radius is modeled as a continuous random variable; the first distributed Gaussian $f_R(r)$ and the second distributed Rayleigh $h_R(r)$ as shown in Table 1. In all cases the range of radii values is 100-300 Å (angstroms).

To find the current probability density functions ($f_I(i)$ for the Gaussian pdf and $h_I(i)$ for the Rayleigh pdf) describing current for a single tip, the root (r_0) for the radius r and the derivative of the current must be found [15] from equation (6):

$$r_0 = \frac{\ln\left[\frac{i(r)}{2x10^{-16}\pi A}\right]}{-B} \qquad (7)$$

$$\frac{d}{dr}i(r) = -2x10^{-16}\pi AB\ \exp(-Br) \qquad (8)$$

$$f_I(i) = \frac{f_R(r_0)}{\left|\frac{d}{dr}i(r_0)\right|} \qquad h_I(i) = \frac{h_R(r_0)}{\left|\frac{d}{dr}i(r_0)\right|} \qquad (9)$$

The corresponding current probability density functions are shown in Table 1. These functions are plotted in Figure 1. The total probability area under each of the curves has been calculated and shown to be unity. Since the abscissa current values are in amperes and cover a range of only about 0.001 ampere, the plotted ordinate values can be exceedingly large. In the continuous random variable case the point probabilities at a particular current value have no meaning; only in a range of current values can a determination of probability be made. The expected values for tip current were computed and are also shown in Figure 1.

Using a similar procedure for finding functions of a random variable, the current probability density functions describing the total current from an array are derived. The resultant total current probability density functions mirror the tip current probability density functions with the substitution of the total array current variable for the tip current variable. The expected values for the total array current are those for the tip current multiplied by the number of tips in the array.

Choosing between probability density functions for modelling the array current performance is important. Since the actual distribution is difficult and expensive to obtain, it often remains unknown. However, some insight from experimentation may be used to identify a likely pdf for a given fabrication process.

We propose the use of the Rayleigh distribution to represent the tip radius variation. Consider that etch rates also vary as a function of crystal plane or lattice direction. For example, in a simple cubic lattice the directions x, y, and z could experience different etch rates. If these particular coordinates at the tip surface are considered Gaussian distributed random variables due to etching variations along their respective directions, then the random variable representing the radius would be:

$$R=\sqrt{X^2+Y^2+Z^2} \qquad (10)$$

With this definition, the random variable R would be Rayleigh distributed [16]. The same approach can be generalized to include any number of lattice directions (i.e., for the diamond lattice) and the resulting tip radius pdf would still be shown to be Rayleigh.

The Rayleigh distribution is shown plotted against the Gaussian distribution in Figure 2. The Rayleigh parameters have been set to align closely with the Gaussian distribution so that a comparison of current calculations can be made. The conjecture presented here is that while the Gaussian tip radius pdf is of interest, the Rayleigh pdf is probably a more realistic choice in modelling the field emission current from an array. In a fabrication process, the photolithography and etching steps are designed to achieve a targeted tip radius value. As the process (i.e., wet or plasma etching) is carried out to achieve the limits of its capability (i.e., sharpness), the process variation will be exhibited in the process parameter that represents degradation from its limits (i.e., decreased tip sharpness). The resultant tip radius pdf would exhibit a cutoff at the small radii end of the pdf rather than the tail that characterizes the Gaussian distribution.

VII. Summary of Results

The variation in tip radius inherent in the fabrication of a field emission array is a result of the statistical nature of the fabrication process. The resultant I-V characteristic is strongly dependent on the sharpest tips in the array. To quantify the performance of the

array, the tip radius is viewed as a random variable and stochastic concepts are applied. In the case of a Gaussian distributed tip radius, the array current has a lognormal distribution.

It can be observed that the tips with a small radius have a dominating effect relative to the larger radius tips. For the Gaussian array, the tips with radii between 100-150 Å contribute about 1% of the current because there are so few tips in that range for the chosen standard deviation of 15 Å; the tips 150-200 Å contribute 85%, the tips 200-250 Å contribute 14%, and the tips 250-300 Å contribute a negligible current percentage.

It has been proposed that, at least in some cases, the variation of the tip radius may be more closely modeled by a Rayleigh distribution rather than a Gaussian distribution. The Rayleigh tip radius pdf example results in an array current that is about 60 percent of the current calculated from a similar array with a Gaussian distributed tip radius. Additional calculations of expected tip current for various parameters are listed in Table 2. The particular Rayleigh pdf parameters listed to the right of the Gaussian parameters have been determined to match the two distribution functions as shown in Figure 2. Comparison of the horizontal pairs of expected tip currents indicates that the Rayleigh expected current falls below the Gaussian expected current, and to a greater degree as the distribution spread or standard deviation is increased.

The tabulated values of expected current are plotted in Figure 3 to highlight the ratio of the standard deviation to the mean. The Rayleigh curves are consistently below their respective, paired Gaussian curves. The upward trending of the Gaussian curve (a) in Figure 3 is reflective of the fact that the pdf functions with the ratio $\sigma/\mu=0.1$ have their Gaussian tails substantially within the limits of tip radii used to add up current contributions. The increased standard deviations of the other Gaussian curves designated as (b) and (c) (i.e., $\sigma/\mu=0.2$, $\sigma/\mu=0.3$) resulted in a substantial portion of the pdf Gaussian tails falling outside the limits of tip radii used to add up current contributions.

The practical matter of examining the microtips of an array by sampling to determined whether the tip radius is distributed either Gaussian or Rayleigh is indeed difficult. As shown in Figure 2, such a task is a determination of whether the Gaussian tail is present or not. An alternative for making such a pdf determination is to sample the microtips for the purpose of determining a mean value radius and a standard deviation. This statistical information can then be used to model the microtip array as demonstrated herein, and the modeled current can be compared with actual current in making a final determination of the tip radius pdf.

It is important to note that the above analysis suggests that it may be difficult to accurately predict the performance of an array-type emission device, based on the

measured emission characteristics of a single tip. We have shown that the total current of such a device depends in a nonlinear fashion on the statistical variation of the tip radii which will inevitably occur in a fabrication process, and it is accentuated by using micron-sized procedures to form nanometer-sized structures. However, the understanding and quantification of the statistical effects associated with tip radius variation can assist in developing a device testing strategy to support a fabrication specification.

REFERENCES

[1]C.A. Spindt, C.E. Holland, A. Rosengreen, and Ivor Brodie, IEEE Trans. Electron Devices, ED-38, 2355 (1991).

[2]R.J. Harvey, R.A Lee, A.J. Miller, and J.K. Wigmore, Proceedings of the 2nd Institute of Vacuum Microelectronics Conference, Bath, England, 1989, ed. R.E. Turner, Institute of Physics Conference Series, 99, Institute of Physics, Bristol and New York.

[3]C.H. Hunt, J.T. Trujillo, and W. Orvis, IEEE Trans. Electron Devices, ED-38, 2309 (1991).

[4]J.D. Levine, Invited papers presented at IVMC, Grenoble, France, July 1994. Submitted for publication to J. Vac. Sci. Technol.

[5]J. He, P.H. Cutler, N.M. Miskovsky, T.E. Feuchtuang, T.E. Sullivan, and M. Chung, Surf. Sci. 246, 348 (1991).

[6]P.H. Cutler, J. He, N.M. Miskovsky, T.E. Sullivan, and B. Weiss, J. Vac. Sci. Technol. B 11, 387 (1993).

[7]I. Brodie and C.A. Spindt, *Vacuum Microelectronics*, Academic Press Inc., New York, 14 (1992).

[8]J.D. Zuber, T.E. Sullivan, L. Pan, V. Peridier, and P.H. Cutler, Paper submitted to J. Vac. Sci. Technol.

[9]David W. Jenkins, IEEE Trans. Electron Devices, ED-40, 666 (1993).

[10]Jun He, Theory of Electron Emission from Atomically Sharp Metallic Emitters in High Electric Fields, The Pennsylvania State University, iv (1992).

[11]Dan Nicolaescu, J. Vac. Sci. Technol. B 11, 392 (1993).

[12]R.H. Good Jr. and E.W. Muller, *Handbuch der Physik, Vol. XXI*, Springer, 188 (1956).

[13]C.A. Spindt, I. Brodie, L. Humphrey, and E.R. Westerberg, J. Appl. Phys. 47, 5250, (1976).

[14]Henry Stark and John W. Woods, *Probability, Random Processes, and Estimation Theory for Engineers*, Prentice-Hall, Inc., Englewood Cliffs, NJ, 37-48 (1986).

[15]Henry Stark and John W. Woods, 73-81.

[16]Wilbur B. Davenport, Jr., *Probability and Random Processes*, McGraw-Hill, 128 (1970).

CAPTION PAGE

Figure 1. Tip current probability density functions for Gaussian and Rayleigh distributions of tip radii between 100-300 Å, with V=150 volts, k=1.6, and ϕ=4.7 eV. (a-Gaussian, b-Rayleigh). Calculated expected values: Gaussian 2.16 μA and Rayleigh 1.36 μA.

Figure 2. Comparison of a Gaussian pdf to a Rayleigh pdf for the tip radii range 100-300 Å. The Gaussian parameters are mean μ=200 Å and standard deviation σ=15 Å. The Rayleigh parameters are γ=175 Å and λ=23 Å. (solid-Gaussian, dashed-Rayleigh).

Figure 3. Expected tip current vs. tip radius for various σ/μ ratios. (a-Gaussian with σ/μ=0.1, b-Gaussian with σ/μ=0.2, c-Gaussian with σ/μ=0.3, d-Rayleigh similar to curve a, e-Rayleigh similar to curve b, f-Rayleigh similar to curve c).

Table 1. Comparison of tip current probability density functions based on Gaussian and Rayleigh tip radius probability density functions. Φ is the Heaviside unit step function in the Rayleigh pdf.

Table 2. Tip Current Expected Value Examples.

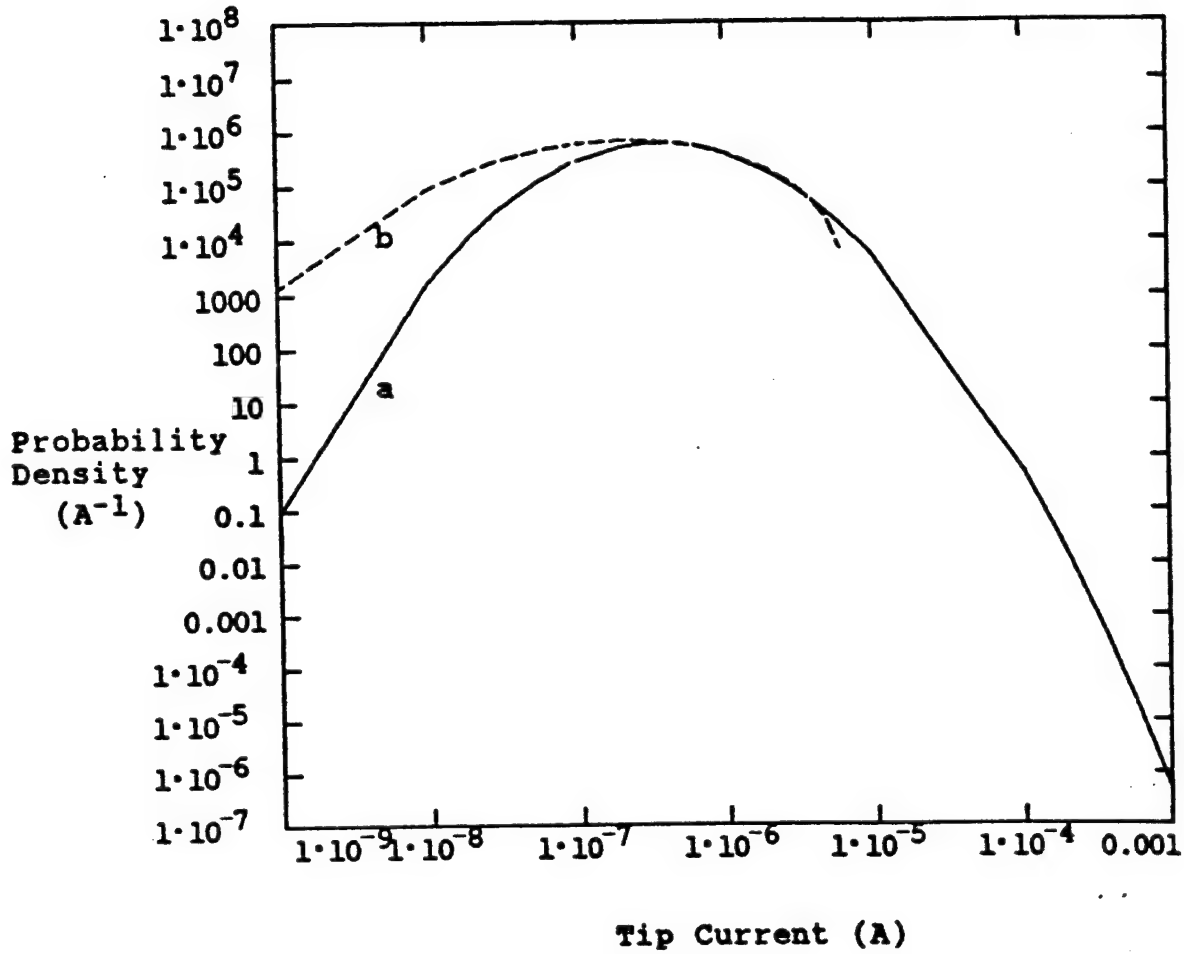
1·10^8
1·10^7
1·10^6
1·10^5
1·10^4
1000
100
10
1
0.1
0.01
0.001
1·10^-4
1·10^-5
1·10^-6
1·10^-7
Probability Density (A^-1)
a
b
1·10^-9
1·10^-8
1·10^-7
1·10^-6
1·10^-5
1·10^-4
0.001
Tip Current (A)

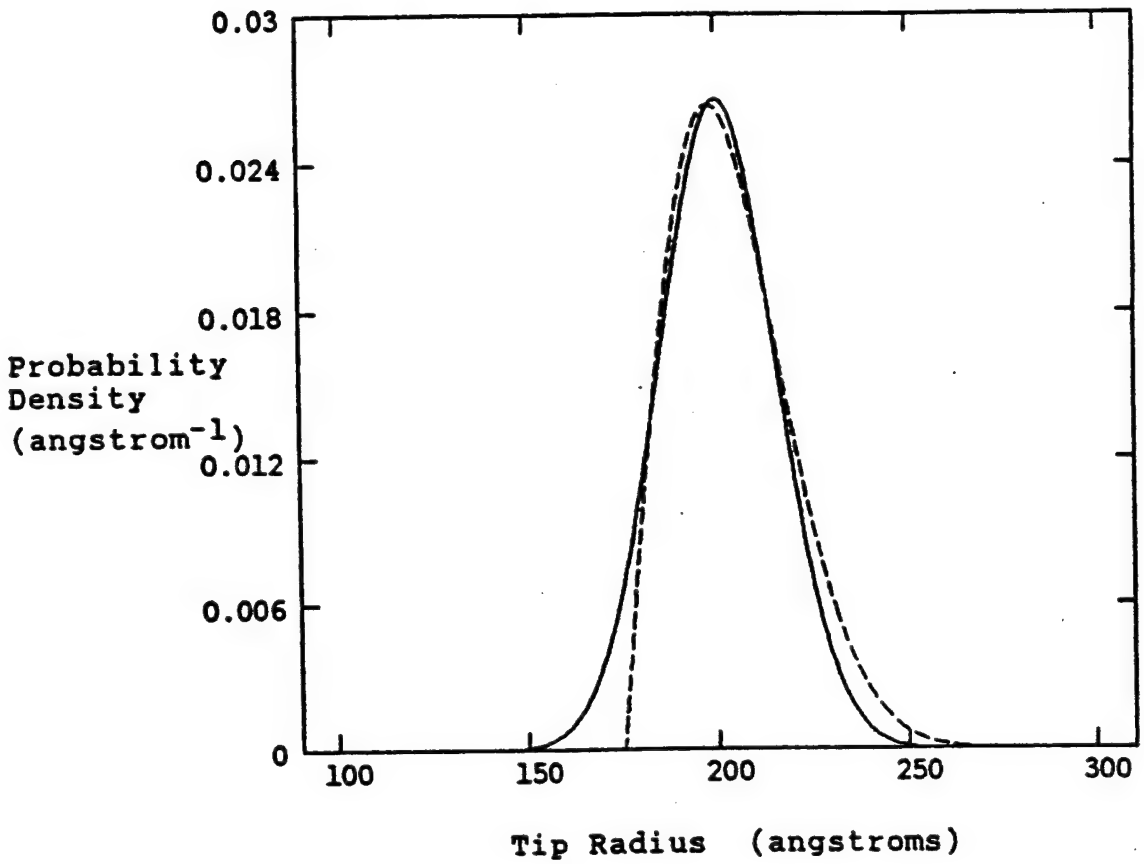
0.03
0.024
0.018
0.012
0.006
0
Probability
Density
(angstrom^{-1})
100
150
200
250
300
Tip Radius (angstroms)

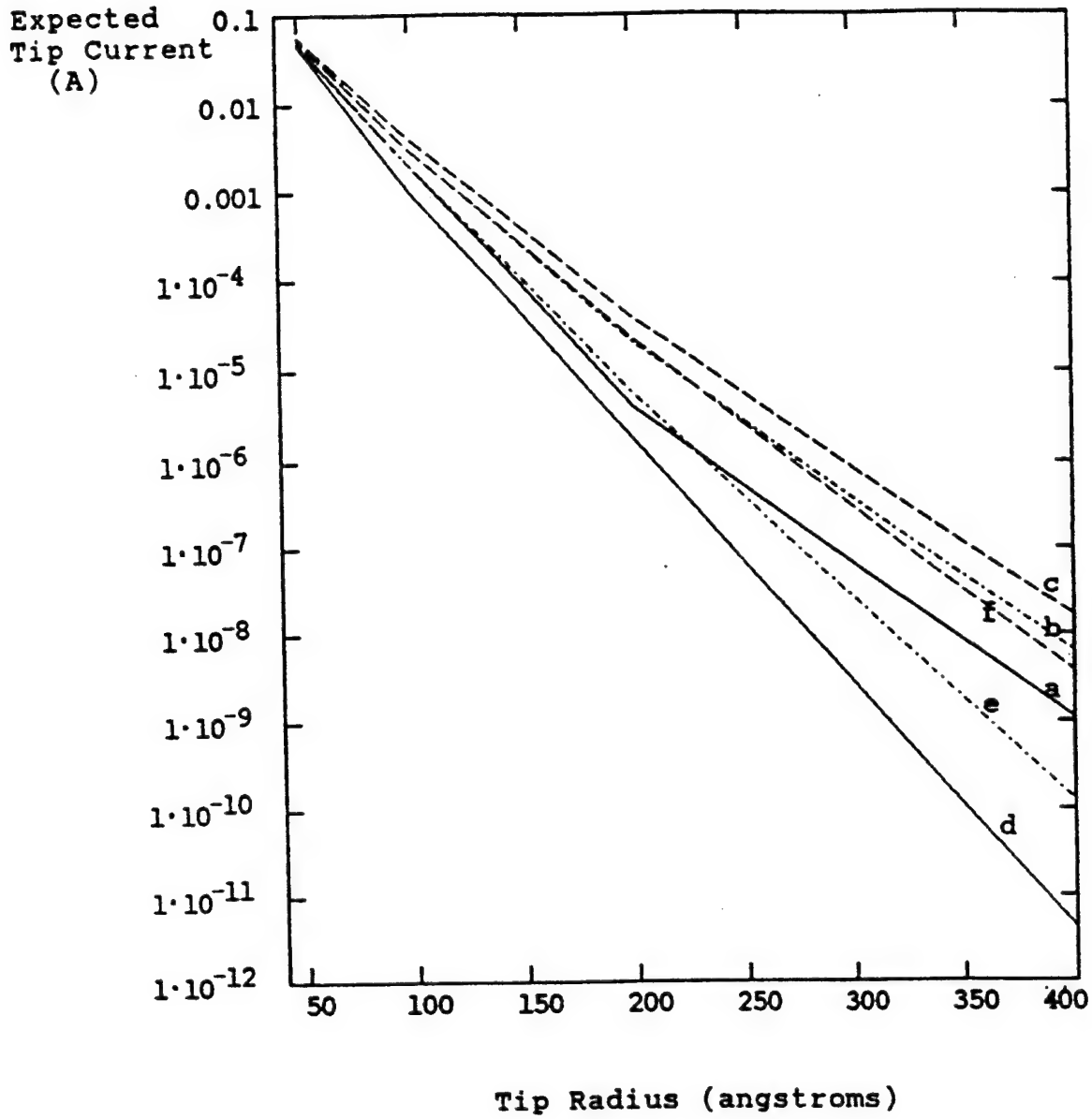
Expected Tip Current (A)
0.1
0.01
0.001
1·10^-4
1·10^-5
1·10^-6
1·10^-7
1·10^-8
1·10^-9
1·10^-10
1·10^-11
1·10^-12
50
100
150
200
250
300
350
400
c
f
b
a
e
d
Tip Radius (angstroms)

Gaussian (μ=200 Å, σ=15 Å)

Tip radius pdf

$$f_R(r) = \frac{1}{\sqrt{2\pi}\sigma} \exp\left[-\frac{1}{2}\left(\frac{r-\mu}{\sigma}\right)^2\right]$$

Current pdf

$$f_I(i) = \frac{\frac{1}{\sqrt{2\pi}\sigma} \exp\left[-\frac{1}{2}\left(\frac{\frac{\ln\left(\frac{i}{2x10^{-16}\pi A}\right)}{-B} - \mu}{\sigma}\right)^2\right]}{|-Bi|}$$

Rayleigh (γ=175, λ=23 Å)

Tip radius pdf

$$h_R(r) = \left[\frac{r-\gamma}{\lambda^2} \exp\left[-\frac{1}{2}\left(\frac{r-\gamma}{\lambda}\right)^2\right]\right] \Phi(r-\gamma)$$

Current pdf

$$h_I(i) = \frac{\left[\frac{\frac{\ln\left[\frac{i}{2x10^{-16}\pi A}\right]}{-B} - \gamma}{\lambda^2} \exp\left[-\frac{1}{2}\left[\frac{\frac{\ln\left[\frac{i}{2x10^{-16}\pi A}\right]}{-B} - \gamma}{\lambda}\right]^2\right]\right] \Phi\left[\frac{\ln\left[\frac{i}{2x10^{-16}\pi A}\right]}{-B} - \gamma\right]}{|-Bi|}$$

Gaussian			Rayleigh		
mean μ	std dev σ	current exp value	γ	λ	current exp value
50	5	48 mA.	41	7.6	46 mA.
50	10	55 mA.	34	15	46 mA.
50	15	57 mA.	25	23	53 mA.
100	10	2 mA.	84	15	1 mA.
100	20	3 mA.	67	30	2 mA.
100	30	4 mA.	51	45	3 mA.
200	20	3.2 µA.	167	30	1.7 µA.
200	40	20.6 µA.	134	61	5.5 µA.
200	60	37.6 µA.	104	91	21.9 µA.
400	40	1.54 nA.	334	61	.004 nA.
400	80	6.31 nA.	268	121	.119 nA.
400	120	16.44 nA.	208	185	3.6 nA.

Appendix D

I. INTRODUCTION

Experiments on frequency mixing [1-3] and tunneling time measurements [4-6] have stirred renewed interest in the problem of tunneling through time dependent barriers in a vacuum diode configuration such as the STM junction. When the laser field interacts with the STM, the tip and base act as an antenna system for detection, harmonic generation and mixing [7]. The resulting nonlinear I-V characteristics of the STM diode produce both a rectified DC and AC tunneling voltage bias [7]. Earlier, the metal-oxide-metal point-contact diode with the same configuration was used to determine absolute frequencies up to the visible (~10^{15} Hz) and as a consequence of these precise measurements, the speed of light is redefined as an exact SI constant of 299792458 m/s [8]. Lucas et al. [9] and Krieger and co-workers [1-3] have claimed that the STM configuration is superior to the point-contact diode because of its controllable gap width and electron transport in vacuum. This latter is easier to treat theoretically than transport through an oxide layer. However, at present the frequency response of the STM junction has only been measured to a few tens of gigahertz (~10^{13} Hz). There are few theoretical treatments of electron transport through oscillating barriers [10-14]. Here we describe briefly the formulation of a theory and present calculations of the inelastic photo-assisted tunneling through a planar junction with both a static DC voltage and a AC voltage of angular frequency ω. One purpose of this paper is to ultimately explain the experimental data of Nguyen et al.[4] for the determination of the tunneling time in a laser irradiated STM junction.

In 1987 Cutler et al. [15] proposed an experiment to estimate the time of transit of an electron tunneling through a quantum mechanical barrier by measuring the DC current as a function of gap spacing (for a fixed laser frequency) or as a function of frequency (for a fixed gap spacing) in an irradiated STM junction. If a linearly polarized laser beam is focused on the STM junction with the shank of the tip assumed to be many wavelengths longer than the radiation, then the tip acts as an antenna to couple the radiation and the junction. The current at the laser frequency will be propagated with small attenuation over an appreciable length and establish a time dependent oscillating potential between the tip and base. Because of the geometric asymmetry of the junction,

a DC component is generated of the form

$$I_{DC}=I_0+\sum_{n=1}^{\infty}\frac{V^{2n}}{2^n(2n)!}\frac{d^{2n}I_0}{dV^{2n}}. \tag{1}$$

where the second term arises from the non-linearity of the junction [4]. To estimate the tunneling time they assume a simple pseudo-kinetic description of ballistic transport, for the case of fixed gap distance at a constant frequency. If the junction is irradiated by a laser of a fixed frequency where the polarization is parallel to the axis of the tip, the electron transfer process is enhanced during half of the period when the electric field vector of the laser beam is accelerating. During the second half of the period when the laser field is reversed, the barrier will increase and transport will be diminished [4,9]. If the gap width is greater than some critical value s_c, the electron will not have "enough time" to traverse the barrier and be detected before the field is reversed. The tunneling time can be deduced from [4,16]

$$\tau\sim\frac{s_c}{v} \tag{2}$$

where it is found that $v\approx v_F$, the Fermi velocity of the electrons in the metallic electrodes [4,16]. The argument for estimating the tunneling time is similar for the case of a fixed gap spacing with a variable frequency. If the frequency changes too rapidly then the electron will not have "enough time" to traverse the barrier before the field reverses direction.

In 1989, Nguyen et al. [4] used the dynamical response of an STM to measure an operational tunneling time. In this method, a natural time scale is provided by the frequency of the laser that constitutes an integral part of the measuring apparatus. The laser causes the tunneling and at the same time determines the "speed" of the tunneling process. In this experiment, a linearly polarized Nd-YAG laser of wavelength $\lambda=1.06\mu m$ was focused on an STM junction consisting of a W-tip (of radius of curvature ~2nm and a Si base in UHV (~10^{-10}torr). The experiment was performed with no applied DC bias.

The rectified current was measured from tip to sample. From their results, using Eq. (2), they deduced a tunneling time of about 1.8 fs. This is in agreement with the theoretical estimates of Hartman [17], Buttiker et al. [11] and Huang et al. [16]. A somewhat different version of this experiment by Moller et al. [18] yielded similar results but the interpretation of the tunneling time is still in question. Other attempts have been made to measure the "traversal time" [5,6]. Most related is the experiment of Gueret et al.[5] who indirectly measured the traversal time in a heterostructure tunneling barrier using the orbital analog of a Larmor spin precessional clock. Their value of τ for a barrier of 40-50 nm in width scales with the results of Nguyen et al. for a barrier of 1-2 nm [4].

In this paper we first describe briefly the formulation of a theory of the inelastic mediated photo-assisted tunneling for a planar bimetallic junction with both a static DC voltage and a time dependent bias of angular frequency ω. A more detailed derivation and analysis will be published elsewhere [14]. We then present results for a trapezoidal barrier surmounted by an oscillating potential of the same frequency range as used in the tunneling time experiments [4].

In Section II an expression for the current is derived using a kinetic formulation of the transfer hamiltonian method. Although the current is initially calculated within the free electron model, the kinetic formulation allows for the inclusion of band structure effects through the density of states factors. In section III the formalism is applied to a model planar MVM diode with a trapezoidal barrier (due to an external static field) surmounted by a time dependent oscillating potential. Although the wave function can be calculated exactly to infinite order, we have initially calculated the current to first order in order to focus on the role of single photon mediated inelastic tunneling. The transition probability is calculated using time dependent perturbation theory. The photo-assisted inelastic tunneling current was obtained as a function of frequency, fields, barrier parameters and material asymmetry. The results presented in Section IV indicate that for the tunneling biases used in STM experiments, the contribution of inelastic mediated photo-assisted tunneling rises rapidly for frequencies $\geq 10^{15}$ Hz (i.e., visible). The results are applied to an analysis of the tunneling time experiments of Nguyen et al. [4]. The conclusions suggest some constraints but do not invalidate the experimental procedure used for

extracting tunneling times in an irradiated tunneling junction. This is discussed in Section V.

II. TUNNELING CURRENT FORMALISM

The tunneling current is calculated using a kinetic formulation of the transfer hamiltonian method. Time dependent perturbation theory is used to determine the perturbed barrier wave functions. The harmonic perturbation is of the form,

$$V(t) = eV_{os}\cos\omega t, \tag{3}$$

where V_{os} is the amplitude of the applied oscillating field and ω is the angular frequency.

The inelastic (and elastic) tunneling enhancement due to this perturbation is viewed as a transition from an electron energy state E_{ol} (electrode to the left of the barrier) to an energy state $E_{mr}=E_{ol}\pm m\hbar\omega$ (electrode to the right of the barrier), where m is an integer. For weak coupling of the two electrodes, the wave function inside the barrier region can be written as,

$$\Psi(r,t) = a_{ol}\Phi_{ol}(r)e^{\frac{-iE_{ol}t}{\hbar}} + \sum_m b_{mr}(t)\Phi_{mr}(t)e^{\frac{-iE_{mr}t}{\hbar}} \tag{4}$$

where a(t) and b(t) are time dependent coefficients. The functions $\Phi_{ol}(r)$ and $\Phi_{mr}(r)$ are the spatial solutions of the unperturbed left and right hamiltonians H_l and H_r, respectively. These barrier wave functions have decaying exponential like tails in the barrier region whose overlap is responsible for the tunneling.

Using time dependent perturbation theory and the initial conditions a(0)=1 and b(0)=0, we obtain to first order [19],

$$b_m^{(1)}(t) = \frac{1}{i\hbar}\int_0^t \langle\Phi_{mr}|V(t')|\Phi_{ol}\rangle e^{i\omega_{mo}t}dt'. \tag{5}$$

Here $\omega_{mo}=(E_{mr}-E_{ol})/\hbar$. The transition rate from the initial state (i) to the final state (f) is

$$R_{if}=\frac{1}{t}\sum_{m}|b_m(t)|^2, \tag{6}$$

We assume that the final states are dense enough so that the total transition probability in Eq.(6) can be expressed in terms of an integration. If the parallel component of the energy is conserved during tunneling, the transition rate from state E_{xi} to E_r can be written

$$R_{ir}=\frac{1}{t}\int dE_{xr}\rho(E_{xr})|b(t)|^2(1-f(E_r)), \tag{7}$$

where the x-direction is the normal direction and the Fermi factor has been introduced to account for occupancy of the final state. Since the transmitted probability current is equal to the tunneling rate R_{ir}, the transmission coefficient or tunneling probability is

$$D_{ir}=\frac{R_{ir}}{R_0}, \tag{8}$$

where R_0 is the probability current incident on the barrier. For a free electron model and box normalization,

$$R_0=\frac{\hbar k_l}{m}|a_{11}|^2, \tag{9}$$

where the coefficient of the incident plane wave is a_{11}.

The tunneling current within the kinetic formulation is the product of the arrival rate, density of initial states, occupation factor for initial state and tunneling probability integrated over all initial states, E_i,

$$J_{if}=\int \rho(E_i)\nu(E_i)f(E_i)D_{if}dE_i, \tag{10}$$

where ν is the arrival rate of electrons on the barrier and $\rho(E_i,E_{xi})$ is the density of states for incident electrons having energy between E_i and E_i+dE_i and normal energy between E_{xi} and $E_{xi}+dE_{xi}$.

Within the free electron approximation the transmission coefficient is [20]

$$D_{lr}=\frac{1}{t\hbar^2}\int dE_{xr}\frac{1}{v_1|a_{11}|^2}[1-f(E_r)]\rho(E_{xr})|M_{lr}|^2\left(\frac{\sin^2\omega_-^2 t/2}{\omega_-^2}+\frac{\sin^2\omega_+ t/2}{\omega_+^2}+\text{cross terms}\right) \quad (11)$$

where $\omega_\pm=(E_r-E_l\mp\hbar\omega)/\hbar\equiv E_\pm/\hbar$ and

$$|M_{lr}|^2\equiv|<\Phi_r|eV_{os}|\Phi_l>|^2 \quad (12)$$

for a harmonic perturbation. In the limit of long time,

$$\lim_{t\to\infty}\frac{1}{t}\frac{\sin^2(E_\pm t/2\hbar)}{(E_\pm t/2\hbar)^2}=2\pi\hbar\delta(E_\pm) \quad (13)$$

The delta function limit yields the result that the most probable transitions involve the exchange of a single photon. The short time limit is proportional to t indicating that the tunneling current initially increases with time [19].

III. TUNNELING CURRENT FOR A TRAPEZOIDAL BARRIER IN FE APPROXIMATION

In this section we calculate the current for the case of a trapezoidal barrier within the free electron approximation. The hamiltonian for the left electrode is

$$H_l=-\frac{\hbar^2}{2m}\nabla^2+[V_0-Fx]\Theta(x-s), \quad (14)$$

and the left electrode hamiltonian is

$$H_r=-\frac{\hbar^2}{2m}\nabla^2+[v_0-Fx]\Theta(s-x)+[\zeta_l-\zeta_r-eV_{st}]\Theta(x-s). \quad (15)$$

Here $\Theta(x)$ is the step function, F is the applied static electric field, $\zeta_{l,r}$ are the Fermi energies of the left and right electrodes, and 's' is the barrier gap width. The zero of energy is taken to be the bottom of the left hand electrode. The solutions for the unperturbed hamiltonians are

$$\Phi_{l(r)}(\mathbf{r}) = A^{-1/2} e^{i\mathbf{k}_t \cdot \mathbf{r}_t} \chi_{l(r)}(x), \tag{16}$$

where A is the normalized area of the planar contact and $\mathbf{k}_t$ is the transverse component of the wave vector. The solutions for $\chi_{l(r)}$ are given by a linear combination of plane waves in the electrodes and by Airy functions of the first and second kind in the barrier region [20,21]. Using boundary matching at the two interfaces, χ can be determined exactly in each region [20,21].

The total tunneling current is [20],

$$\begin{aligned} J_{tot} = \frac{2e\pi}{\hbar} \Bigg(& \frac{1}{|a_{11}|^2} \int_{\zeta_l-\zeta_r-eV}^{\infty} dE_{xr} \int_0^{\infty} dE_{xl} \int_{E_{xl}}^{\infty} dE_l f_l(E_l)[1-f(E_l-E_{xl}+E_{xr}+eV_{st})] \\ & \times \rho(E_l,E_{xl})\rho(E_{xr}+\zeta_r-\zeta_l+eV_{st})[\delta(E_{xr}-E_{xl}-\hbar\omega)]|M_{lr}|^2 \\ & - \frac{1}{|b_{3r}|^2} \int_0^{\infty} dE_{xl} \int_{\zeta_l-\zeta_r-eV}^{\infty} dE_{xr} \int_{E_{xr}}^{\infty} dE_r f_r(E_r+\zeta_r-\zeta_l+eV_{st})[1-f(E_r-E_{xr}+E_{xl}] \\ & \times \rho(E_r+\zeta_r-\zeta_l+eV_{st}, E_{xr}+\zeta_r-\zeta_l+eV_{st})\rho(E_{xl})[\delta(E_{xl}-E_{xr}-\hbar\omega)+\delta(E_{xl}-E_{xr}+\hbar\omega)|M_{rl}|^2 \Bigg) \end{aligned} \tag{17}$$

The subscript 1 refers to the left hand electrode, 2 to the barrier region, and 3 refers to the right hand electrode.

IV. RESULTS

To determine the frequency response of a model W-Au junction we calculated the tunneling current using Eq.(17). In Fig. 1 we exhibit the results of the tunneling current as a function of angular frequency with a static field $F_{st}=1.5\times10^8$V/m and an oscillating field of magnitude $F_{os}=5\times10^8$V/m. Calculations were done for two different gap widths, s=0.8nm and s=1.0nm. For $\omega \leq 5\times10^{14}$rad/s, the current dentsity is independent of frequency; for $\omega \geq 10^{15}$rad/s, there is a rapid increase in the current density, i.e., about a tenfold increase in J as ω goes from 10^{15} to 3×10^{15}rad/s. This behavior is exhibited for both gap widths and other model calculations by the authors give the same systematics

for different values of the static field. The calculated results are in good qualitative agreement with the analysis of Buttiker and Landauer [11] who calculated the transmission coefficient for time dependent tunneling in an oscillating barrier superimposed on a one-dimensional rectangular barrier. Their calculated transmission coefficient for the first two side bands also indicates that at low frequency the probability of tunneling is independent of frequency. However, at higher frequencies, the transmission probability increases rapidly. This is consistent with the results in Fig. 1. This occurs because a particle which absorbs a quantum $\hbar\omega$ and has energy $E+\hbar\omega$ tunnels through the barrier more easily than particles with energy E or $E-\hbar\omega$. For angular frequencies sufficiently greater than $\sim 5\times10^{14}$ rad/s, electrons can gain enough energy so that pure photoemission occurs.

We have also examined the dependence of the tunneling current density on the gap spacing with V_{st} and V_{os} as parameters. In Fig. 2 we exhibit the results for $\omega=1.8\times10^{15}$rad/s (approximately the value for the Nd YAG laser) and for a low frequency $\omega=5\times10^{14}$rad/s. Both the static and oscillating field are 10mV, values typical to some STM experiments. For a constant V_{st} the tunneling current density falls off approximately exponentially as s increases, which mimics elastic tunneling.

Using Eq.(17) we calculated J as a function of 's' at two different frequencies but with a constant $F_{st}=1.5\times10^{6}$V/m and two values of $F_{os}=1.5\times10^{8}$V/m and $F_{os}=5\times10^{7}$. The results are plotted in Fig.3. The curves exhibit similar behavior with a maximum and rapid fall-off with gap distance. This results from ohmic transport for small gap spacings and then conventional tunneling as the gap distance increases. The curves exhibited in this figure are almost identical qualitatively to the low frequency results of Levy Yeyati and Flores [13]. Calculations show that the peak position and fall-off is relatively insensitive to frequency even up to frequencies near the visible. The curves exhibit a cut-off in the rectified current as a function of gap width for a fixed ω and F_{os} as was predicted by Cutler et al. [15]. However, the cutoff does not have the expected dependence on frequency. One of the reasons may be that only a field $F_{os}>F_{st}$ can reverse the direction of the electron's motion and lead to the expected decrease in J_{DC}. In these first calculations the static field is always equal to or greater than F_{os}. In addition, even the

small work function differences of the W-Au junction (~0.2-0.3eV) correspond to effective fields of about 2-3x10^8V/m for a gap width of 1 nm. Hence, the static field always dominates.

CONCLUSIONS

In the present work we have formulated a theory of inelastically mediated photo-assisted emission for a planar bimetallic junction with both a static dc voltage and a time dependent bias. An expression for the current is derived using kinetic theory and the transfer hamiltonian method. The wave functions are determined from time dependent perturbation theory and are calculated recursively to infinite order. The photo-assisted inelastic tunneling current was calculated as a function of frequency, fields, barrier parameters and material asymmetry.

Some important conclusions emerge from these calculations which impose limitations on but do not invalidate the experimental procedure to determine a tunneling time using a laser irradiated STM junction. To make the experiment feasible it is necessary that the rectified DC current must reach a maximum and then decrease as a function of frequency for fixed gap spacing or as a function of gap spacing for a fixed frequency. In the first method, having chosen some appropriate gap spacing, the critical frequency at which I_{DC} decreases to some negligible value must be such that the electron's "motion" can be reversed by the oscillating field before it is detected at the anode. This requires that the effective static field, consisting of the applied static bias and/or the field due to the contact potential difference is less than the amplitude of the laser induced oscillating field. In the alternative procedure, the limitations are less stringent and only the condition that $F_{st}(V_{st}) < F_{os}(V_{os})$ needs to be satisfied. A careful and systematic study will have to be done before definitive criteria can be established to define the exact limitations on the experimental procedure.

REFERENCES

* Supported in part by the Air Force Office of Scientific Research under Grant AFOSR-F-49620-92-J-0209.

1. L. Arnold and W. Krieger, J. Vac. Sci. Technol. **A6**, 465(1988).

2. W. Krieger, H. Koppermann, T.Suzuki and H. Walter, IEEE Trans. Instrum. Meas. **38**, 1019(1989).

3. W. Krieger, T. Suzuki and M. Volker, Phys. Rev. **B41**, 10229(1990).

4. H.Q. Nguyen, P.H. Cutler, T.E. Feuchtwang, Z.-H. Huang, Y. Kuk, P.J. Silverman, A.A. Lucas and T.E. Sullivan, IEEE Trans. Electron Devices **36**,2671(1989).

5. P. Gueret, A.Baratoff and E. Marclay, Europhys. Lett. **3**, 367(1987).

6. D. Esteve, J.M. Martinis, C. Urbina, E. Turlot and M.H. Devoret, Physica Scripta **T29**, 121(1989).

7. T.E. Sullivan, P.H. Cutler and A.A. Lucas, Surf. Sci. **62**, 455(1977).

8. **Proc. 17th General Conf. Measures and Weights.** Sevres, France: Comptes Rendus, BIPM, p. 93, (1983).

9. A. A. Lucas, P.H. Cutler, T.E. Feuchtwang, T.T. Tsong, T.E. Sullivan, Y. Kuk, H. Nquyen and P.J. Sullivan, J. Vac. Sci. Technol. **A6**, 461(1988).

10. P.K. Tien and J.P. Gordon, Phys Rev. **128**, 647(1963).

11. M. Buttiker and R. Landauer, Physica Scripta **32**, 429(1986).

12. S.P. Appel and D.R. Penn, Phys. Rev. **B45**, 6757(1992).

13. A. Levy Yeyati and F. Flores, Phys. Rev. **B44**, 9020(1991).

14. S.H. Park, N.M. Miskovsky, P.H. Cutler, and T.E. Sullivan, to be published.

15. P.H. Cutler, T.E. Feuchtwang, T.T. Tsong, H.Q. Nguyen and A.A. Lucas, Phys. Rev. **B35**, 7774(1987).

16. Z.-H. Huang, P.H. Cutler, T.E. Feuchtwang and R.H. Good, Jr., IEEE Trans. Electron Devices **36**, 2665(1989).

17. T.E. Hartman, J.Appl. Phys. **33**, 3427(1962).

18. R. Moller, U. Albrecht, J. Boneberg, B. Koslowski, P. Leiderer and K. Dransfeld, J. Vac. Sci. Technol. **B9**, 506(1991).

19. L.I. Schiff, **Quantum Mechanics**(McGraw-Hill Book Co., Inc., 1955).

20. Sookyung Hur Park, Ph.D. thesis, August, 1993, The Pennsylvania State University, University Park, PA 16802, unpublished.

21. C.B. Duke, **Tunneling In Solids, Solid State Physics**, vol. 10, ed. by F. Seitz, D. Turnbull and H. Ehrenreich(Academic Press, NY,1969).

LIST OF FIGURES

Figure 1 The tunneling current density as a function of angular frequency for gap widths s=1nm (solid line) and s=0.8nm (dotted line). The average static field is 1.5×10^{8}V/m and the amplitude of the oscillating field is 5×10^{8}V/m.

Figure 2 The tunneling current density as a function of gap width with angular frequency as a parameter. The dotted line indicates the values for $\omega=1.8\times10^{15}$rad/s and the solid line is for $\omega=5\times10^{14}$rad/s. The external bias voltage is 10 mV and the amplitude of the oscillating field is 10^{8}V/m.

Figure 3 The tunneling current density as a function of gap width with amplitude and angular frequency as parameters. The average static field is 1.5×10^{8}V/m. The applied fields $F_{o\omega}=1.5\times10^{8}$V/m (——) and $F_{o\omega}=5\times10^{7}$V/m for $\omega=1.8\times10^{15}$rad/s (– –). Also shown is the curve for the applied oscillating field $F_{o\omega}=1.5\times10^{8}$V/m(-*-*-) with frequency 1.8×10^{11} rad/s. The curve (-- -) is a normalized version of the curve for (-*-*-).

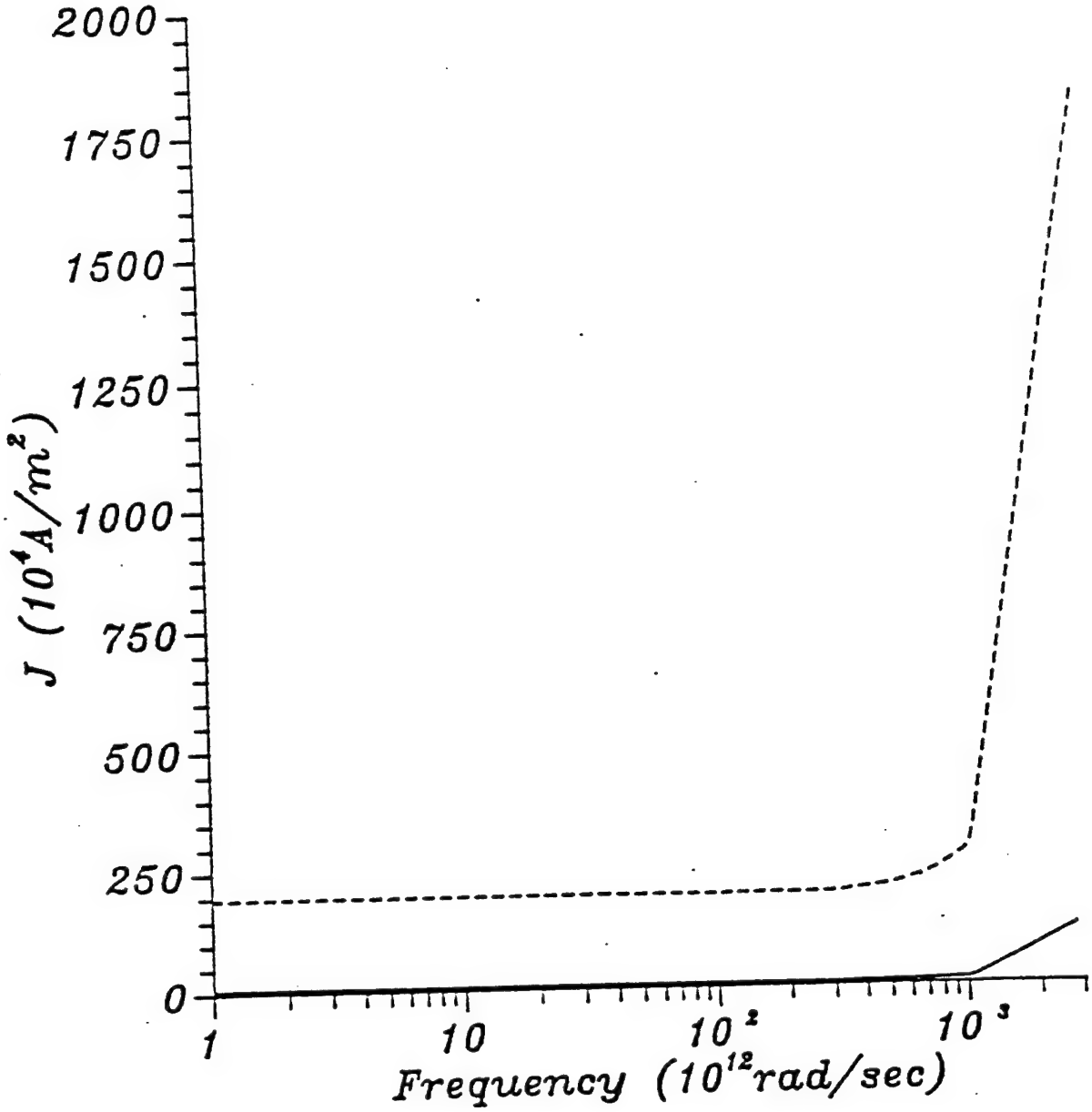
2000
1750
1500
1250
1000
750
500
250
0
J (10^4A/m^2)
1
10
10^2
10^3
Frequency (10^{12}rad/sec)

Fig. 1

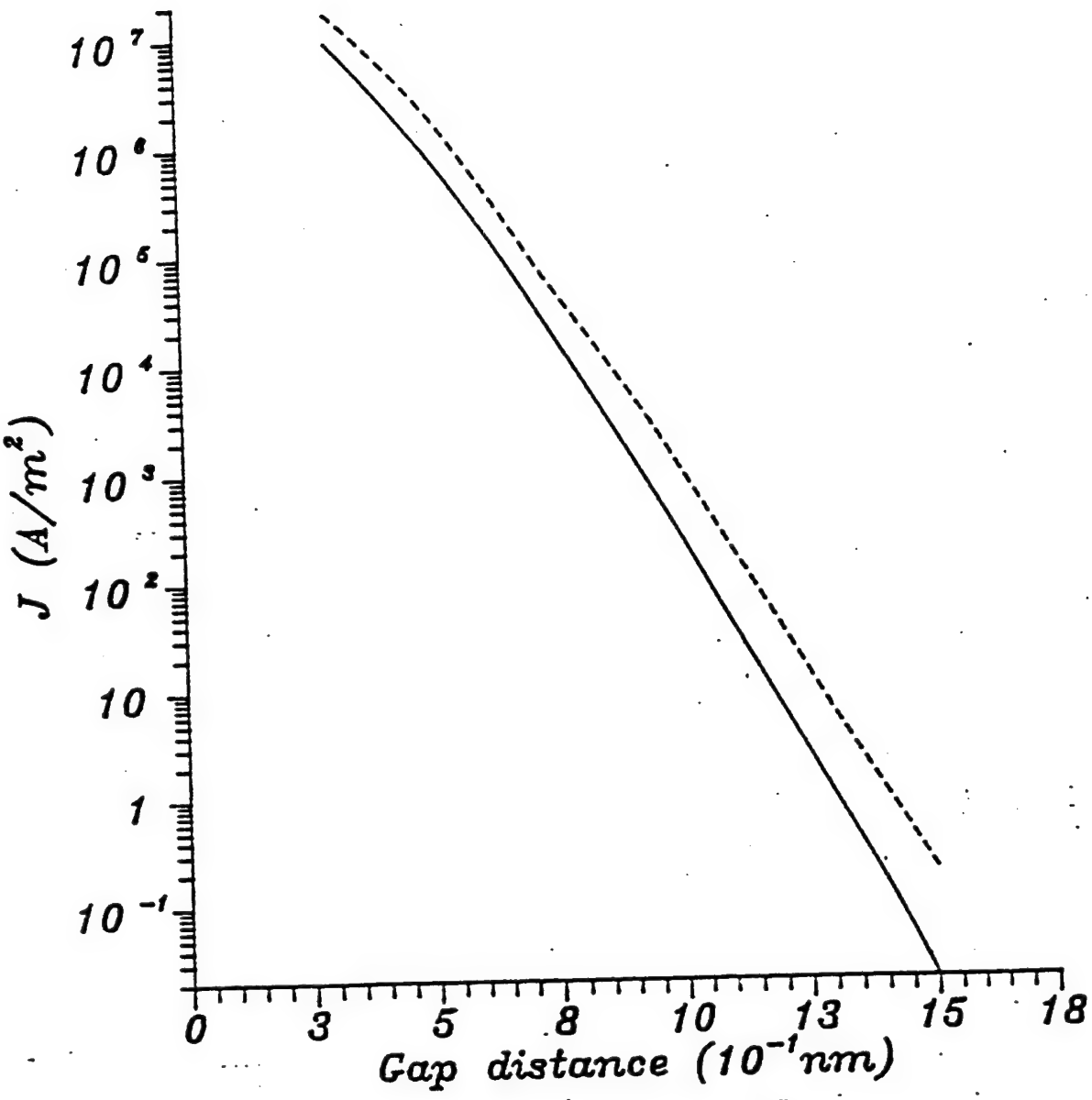
10^7
10^6
10^5
10^4
10^3
10^2
10
1
10^{-1}
J (A/m²)
0
3
5
8
10
13
15
18
Gap distance (10^{-1}nm)

Fig. 2

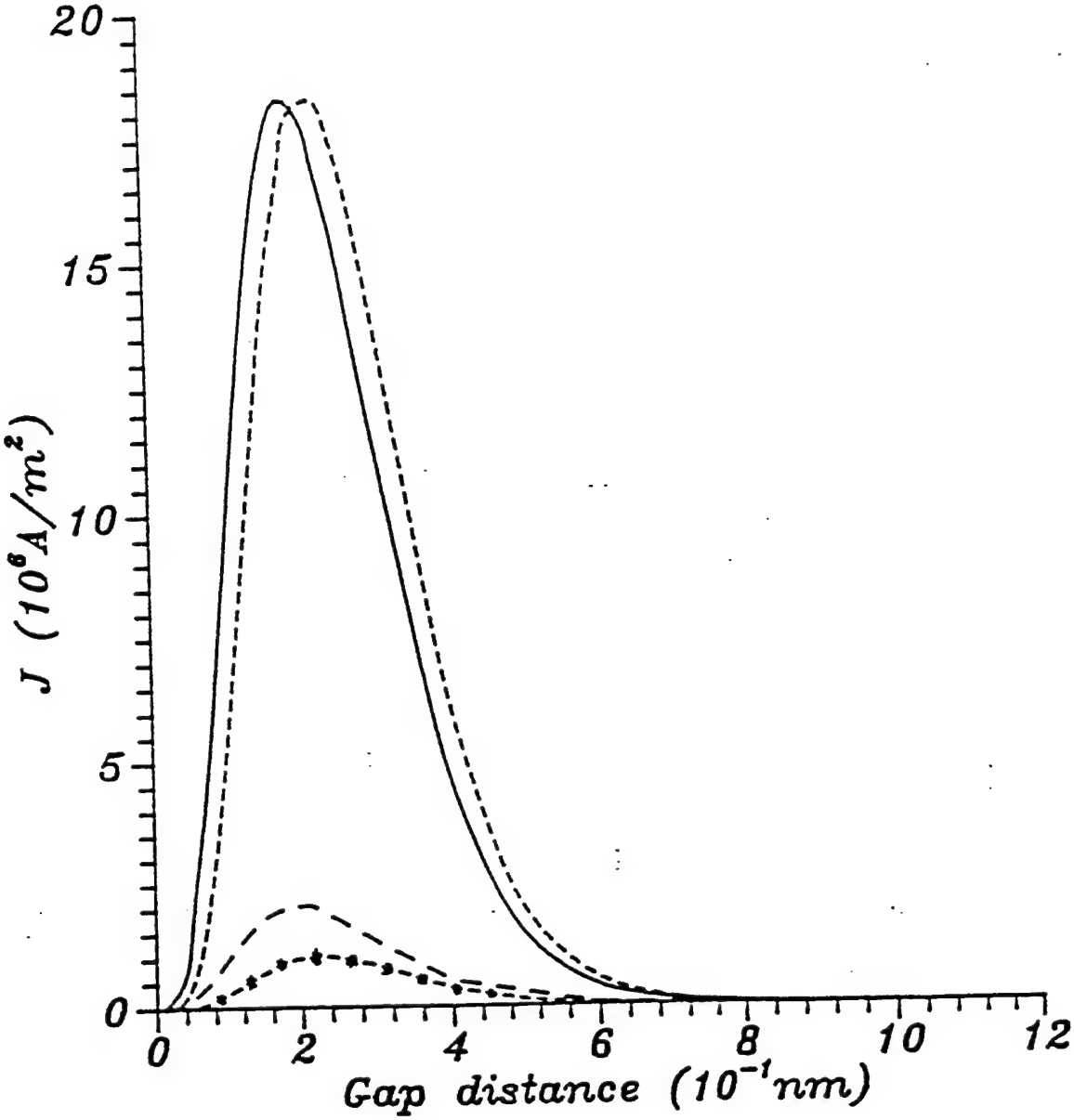

Fig. 3

Appendix E

100 by 100 pixels can take several minutes to display as a three dimensional plot on a typical microcomputer. The same plot takes 30 seconds on this system. If twenty images are recorded in a single day, each one being say, 500 by 500 pixels, displaying that data on a simple microcomputer would require throwing away every other pixel and it would still take hours to review a days worth of data.

The last function of the computer is control of the STM scan. This requires a special output device to send the correct electronic signals to the electronics controlling the STM. There are a number of possible ways to do this. There is an instrument bus, IEEE 488, or direct digital I/O, or an analog control signal generated with a digital to analog converter. Each method has advantages and disadvantages. The D/A method was chosen as a quick and dirty approach. It's cheap, and can interface to simple analog circuitry controlling the STM. It's disadvantage is noise. At some point in the future, a better but more expensive option may be used in it's place.

The requirements for speed and accuracy are roughly the same as those for the A/D converter used to collect data. Now let's outline the actual system built to meet these functions.

3 Meeting the Requirements

3.1 The Outline

This section will explain how the above requirements were met. The overall computer system for the STM is shown in figure 1. This paper will give the details of the hardware shown in figure 1.

3.2 The Chassis

The PC tower was chosen as the basis for this system. The reasons were expansion capacity, availability of boards, and cost. While the PC bus is one of the slower ones available, CPU speeds and video speeds have increased enough in the last couple of years, to allow the PC to be the basis of our system. Only a couple of years ago, STM would have required a much more expensive bus such as VME. The tower case was needed to allow enough cards to be installed (6 expansion cards) and to supply enough power.

3.3 The CPU

The central processor unit (CPU) card is critical. In order to meet the speed requirement outlined above, the CPU had to be fast and able to address large amounts of memory. High speed floating point was also required. The CPU card chosen has an Intel 486DX CPU, running at 66 MHz. This is an minimum. A 100 MHz Pentium would be better.

3.4 Extra Memory

Experience had already shown that 4 megabyte of memory is not enough. In order to be able to handle low resolution images 8 megabyte is just enough. So 8 megabyte of extra memory has been installed. The total RAM in the system is now 20 megabutes. Xwindows is the largest user of RAM. If the system were used without Xwindows, a system with 8 megabytes of RAM would do.

3.5 Disk and Tape

There are four disk drives connected to this system. Two hard disk with a capacity of over 700 megabytes and a two floppy drives, one 5 inch and one 3 inch drive. The speed of disk access is important when large volumes of data must be reviewed or processed. The current system uses an IDE interface. The system could be improved with SCSI disk. The floppy drive is used to make backup copies of data once it is no longer needed on-line. A tape drive which connects through the floppy controller is used for major system backups.

The capacity of the hard disk will be a problem if high resolution data taking begins. A 100 by 100 pixel image only requires 20000 bytes of storage. A single image of 500 by 500 pixels requires 1/2 megabyte to store. That is one floppy disk per image. While the current system can just get by, a larger hard disk and a SCSI tape backup would be a good idea. These can be added to the current system.

The base system, chassis, mother board, disks and tape drive are all rather generic parts.

3.6 Video card

The graphics requirements are currently being met by a Diamond "Viper" SVGA graphics card, and a 14 inch color multiscan monitor. Both of these devices have a resolution of 512 pixels. The graphics board has it's own memory and processing firmware. The video card was a mistake. Diamond has a closed architecture and hence is not supported by second source software. It should be replaced with a better card such as the ATI "Wonder" card. The monitor should also be upgraded to at least a 17 inch monitor to take full advantage the Xwindows environment. If the mother board is upgraded, a PCI bus with ATI video card is recommended for best results using Xwindows. The graphics firmware supports at least 256 colors or 256 grey levels, this is important for image display. It also requires an analog RGB signal to work at such high resolution. It takes a special monitor to use these signals.

3.7 Analog and Digital

There are both an analog to digital and digital to analog boards in this system. Both of these boards were supplied by Computer Boards Inc. [?]. The analog

to digital board is a 12 bit, 50 KHz device. The D/A board is 100 KHz and resolution 16 bits.

The A/D board is used to record tunneling current. The D/A board controls the STM scans by suppling analog X, Y and Z signals to a high voltage amplifier which drives the piezoelectric tube. Also the D/A board supplies the bias voltage to the tip.

These boards are just fast enough to support a 256 pixel image scan. To push to higher resolution imaging, A/D board will need be replaced at some point in the future with a 16 bit, 100 kHz board. The 12 bit resolution of the A/D board is a problem. Twelve bits gives a resolution of 1 part in 4096. But that assumes you make use of the total range of the board. In practice, this is not the case. If the board has a 10 volt range, and the signals from a given experiment only span 1 volt, then the effective resolution of such a board is only 1 part in 400. This is still ok for pictures, but it can add unwanted noise to the signal if statistical analysis is to be performed on the data.

3.8 The Outside World

The current system has two serial lines running to the outside world. One line is connected serial mouse and is used as input for Xwindows. The second line is connected to a standard ASCI terminal and can be used to log into the system to do background task.

There is also a standard ethernet card connecting the system to hypespace. The system allows remote users to log in from anywhere on the internet. It also supports remote Xterminals.

3.9 The Software

Of course the real work in getting all this hardware to function together as a system is in the software. OS9000/PC was the operating system of choice. It is small, fast, powerful and relatively bug free. It supports C, FORTRAN and 486 assembly as the programming languages. It is similar to the UNIX system but is much more compact. It also supports real time operation, which is a real plus in a laboratory environment.

After the operating system, the next level of software is the system of hardware drivers. Each of these programs is required to interface the operating system and applications programs to specific devices in a standardized way. Since this computer system was put together with parts from several different vendors, some of the device drivers (D/A and A/D) had to be developed here. Software to support the serial lines, ethernet and Xwindows were all supplied by MIcroware.

The next level of the software is applications program libraries. There are libraries to support devices such as the graphics processor and mouse, Xwindows. Internet support libraries are supplied by Microware.

Finally, there is the applications software. These programs include various utilities, image processing and display, data acquisition and STM control.

The serial links to the outside world have been functioning for some time and work well. Ethernet access includes telnet and FTP. The graphics system is functioning and emulates a black and with Xterminal. Both the Xserver and the video card must be upgraded to display color images on the system monitor. Currently, images are displayed on a remote HP Xwindow workstation. There is still a lot of work to do at the applications level to develop better displays. Device drivers for the A/D and D/A boards have been developed. Data acquisition and STM control programs have been written and improvements continue.

All of this software must fit into some sort of unified whole. The goal is to acquire and analyze STM data. Since higher resolution imaging is the main thrust of this effort, speed and efficiency of both hardware and software are very critical. This requires that the software effort be well organized and the programs must be well written.

References

[1] M. Aguilar, A. Garcia, P. Pascual, J. Presa, and A. Santisteban, Surf. Sci. **181**, 191 (1987).

[2] J. Becker, Surf. Sci. **181**, 200 (1987).

[3] M. Aguilar, P. Pascual, and A. Santisteban, IBM J. Res. Dev. **30**, 525 (1986).

[4] P. Schroer and J. Becker, IBM J. Res. Dev. **30**, 543 (1986).

[5] Y. Li, L. Vazquez, R. Piner, R. Andres, and R. Reifenberger, Appl. Phys. Lett. **54**, 1424 (1989).

Block diagram of PC/OS9000 computer system

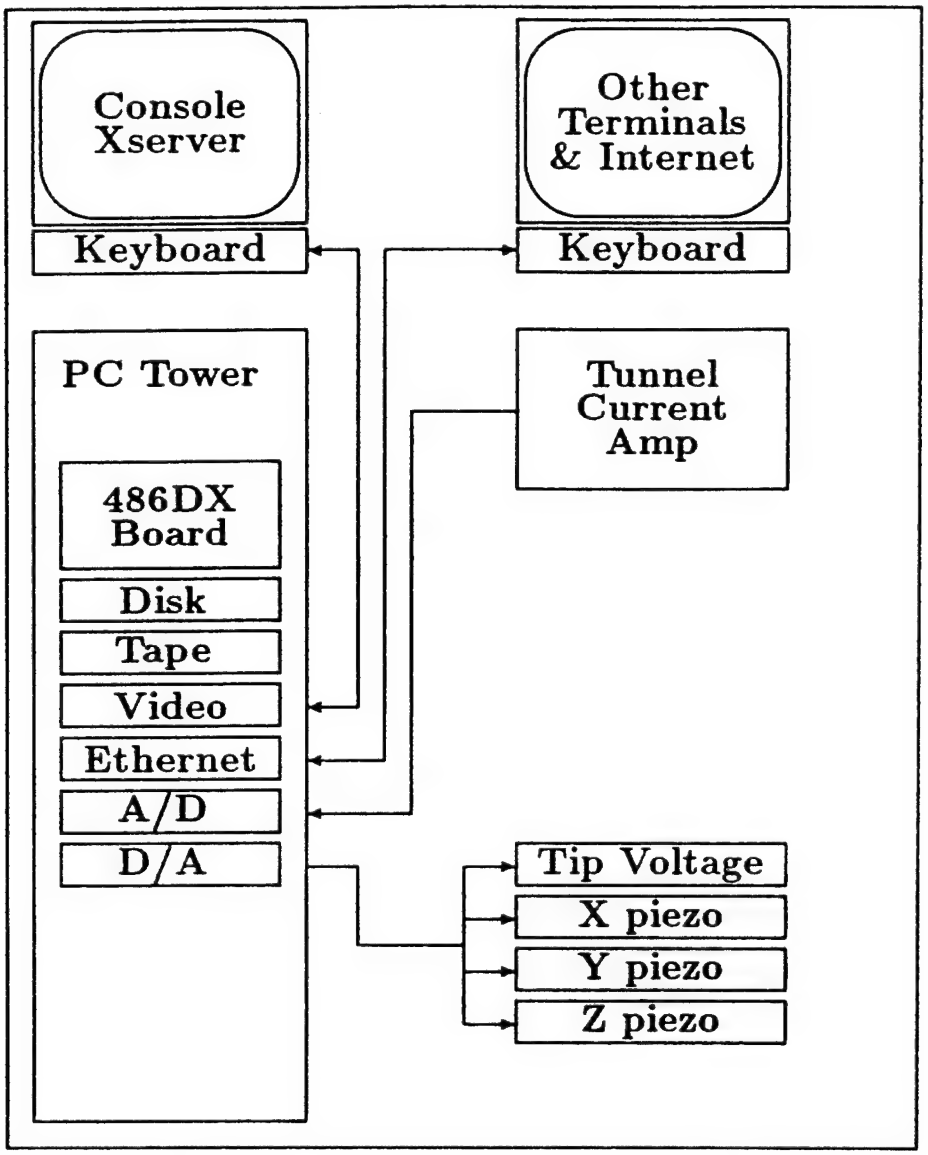

Figure 1: Schematic of Computer System for STM

Appendix F

Figure

A scan of a planar gold surface taken immediately after forming a 17 X 44 Angstrom pit.

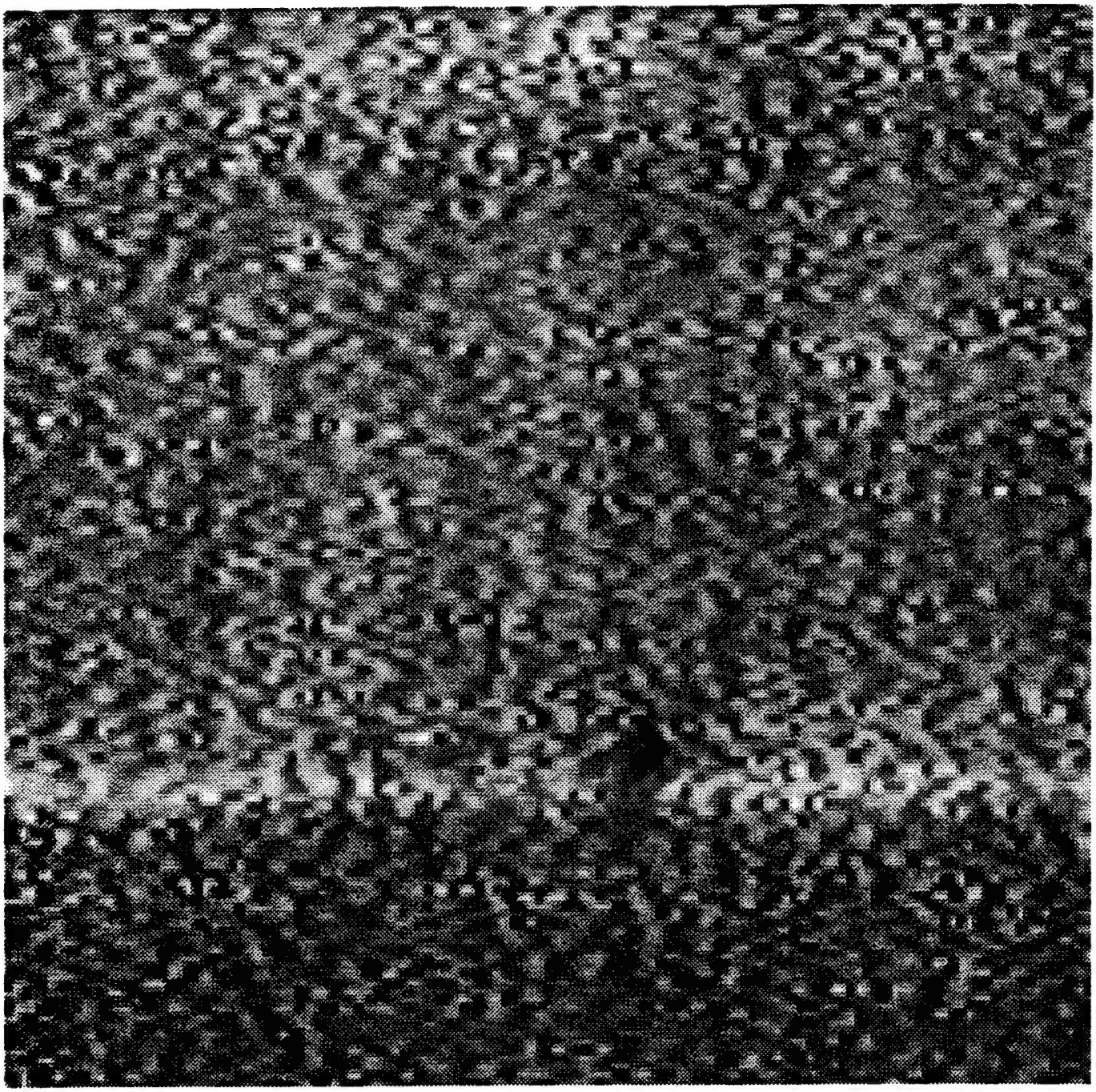

scan2b.804.PS

17Å

44Å

Appendix G

Laser - Induced Thermoelectric Effects in an STM Junction

Sookyung H. Park, N. M. Miskovsky, P.H. Cutler, E. Kazes
Department of Physics
104 Davey Laboratory
The Pennsylvania State University
University Park, PA 16802
and T. E. Sullivan
Department of Electrical Engineering
Temple University
Philadelphia, PA 19122

ABSTRACT

The spatial and temporal temperature distribution for a conical shape metal emitter under laser irradiance is obtained analytically using the Green function method. In this study the tip is modeled as an infinite cone of half angle θ_o which can vary between 0 and $\pi/2$. The full three dimensional heat diffusion equation is solved simultaneously with the Fourier equation for the heat flux assuming no radiation losses. The general solution is obtained for an arbitrary temporal and spatial distribution of the irradiance. With uniform irradiance the temperature rise in the conical tip varies almost linearly with the laser intensity and heating time and depends strongly on cone angle and thermal properties. For a tungsten tip, the temperature increase is about 2-3 orders of magnitude above ambient for a typical laser intensity of about $1 MW/cm^2$ in a time of a few hundred nanoseconds. To study Joule heating and the Thomson thermoelectric effect in the STM junction we first obtained the current distribution inside the emitter. Using this as a volume heat source, we used the Green function method to solve the heat conduction equation. The resulting temperature gradient was then used to obtain the thermoelectric potential. For a tungsten tip at ~ 1000 °K, the thermoelectric effect generates a bias voltage on the order of 10 mV.

I. INTRODUCTION

Recent experiments on laser frequency mixing [1-3] and tunneling time measurments[4] have prompted interest in thermal effects due to laser irradiation of an STM junction. When the laser field interacts with an STM, the tip and base act as an antenna system for detection, harmonic generation and mixing [5]. The resulting nonlinear I-V characteristics of the STM diode junction produce both a rectified dc and ac tunneling voltage bias. In addition, the thermoelectric effects may also contribute to the bias potentials in the junction. To investigate these latter effects it is necessary to determine the laser induced temperature distribution in the junction. The resulting temperature gradient inside the emitter as well as the rectified dc current through the STM junction can produce both resistive (Joule) heating [6] and a Thomson thermoelectric effect due to the absorption or evolution of heat. Thus the STM junction can be heated or cooled by the reversible Thomson heat depending on the direction of tunneling current flow. These heating or cooling effects modify the temperature distribution inside the emitter and anode with the result that a thermoelectric potential can be generated by a temperature gradient between the tip and base. These heating effects also produce thermal expansion [7] so the tunneling gap width will be modulated influencing the tunneling current. To find the temperature distribution inside the tip (and anode for $\theta=\pi/2$) due to Joule and Thomson heat we solved the Laplace and continuity equations to obtain the current distribution. To avoid mathematical singularities and replicate the current distribution for a realistic tip, the infinite cone model is truncated at some appropriate distance from the apex. The temperature distribution is then obtained by solving the heat conduction equation using the Green function method with surface and volume generation of heat. Knowing the temperature gradient, the laser induced thermoelectric potential in the STM junction is calculated.

In section II, we outline the calculation for the temperature distribution in an infinite and truncated conical emitter using the Green function. The solution for surface and volume generation of heat by laser irradiation and by resistive and/or Thomson heat respectively are also given in this section . The thermoelectric voltage generated by heat

and current sources is presented in section III and numerical result and discussion is given in section IV.

II. THE CALCULATION OF THE TEMPERATURE DISTRIBUTION

In our analysis we assume that the emitter tip is an infinite metallic cone of angle θ_o which can varies 0 to $\pi/2$ [see fig.1]. The emitter is immersed in a uniform azimuthally symmetric laser beam incident normally on the cone surface. We here only briefly summarize the details of the calculation of the temperature distribution with surface and volume sources of heat. A detailed description of this analysis is to be published elsewhere.

To obtain the temperature distribution T(r,t), we solve the inhomogeneous heat conduction equation

$$\nabla^2 T(r,t) - \frac{1}{k}\frac{\partial T(r,t)}{\partial t} = -\frac{F(r,t)}{K} \qquad (1)$$

where r and t are spatial and time coordinates, k is the thermal diffusivity, K is the thermal conductivity (k and K are assumed as constant) and F(r,t) is the rate of heat supplied per unit volume per unit time.

We use the Green function method to obtain a general solution of eq. (1).

The procedure is ;

1. Solve for the Green function $G(r,t,r',t')$ for a point source with Neumann boundary conditions

$$n \cdot \nabla G(r,t,r',t') = 0 \qquad (2)$$

where prime denotes the source, and n is an outward pointing normal to the surface. The Green function satisfies

$$\nabla^2 G(r,t,r't') - \frac{1}{k}\frac{\partial G(r,t,r',t')}{\partial t} = -4\pi\,\delta(r-r')\,\delta(t-t') \qquad (3)$$

It is assumed that both volume and surface generation are possible.

2. Apply Green's theorem and the principle of superposition to obtain the solution for an arbitrary source distribution.

For volume and surface generation the resulting temperature distribution is given by [8]

$$T(r,t)=\int_0^t dt'\int_S G(r,t,r',t')\frac{\partial T(r',t')}{\partial n'}\,k\,dS + \int_0^t dt'\int_V G(r,t,r',t')\frac{F(r',t')}{K}\,k\,d^3r' \quad (4)$$

The boundary condition to be satisfied for surface generation is

$$\frac{\partial T(r',t')}{\partial n'} = -\frac{Q(r',t')}{K} \qquad (5)$$

where, in our case, $Q(r',t')$ is the heat produced per unit time per unit area due to laser irradiation at the surface.

It is assumed that in general the laser intensity has Gaussian spatial and temporal distribution:

$$Q(r',t')=Q_0(1-R(\lambda))\exp(-(r'/D^2))\exp(-(t'/T_D)^2) \qquad (6)$$

where Q_0 is the maximum intensity of the laser beam, $R(\lambda)$ is the reflectivity and T_D, D are temporal and spatial pulse widths. The reflectivity is a function of the wavelength λ.

We first consider the emitter to be modelded as an infinite cone. Subsequently we will concern ourselves only with the temperature distribution near the apex of the emitter. It can be shown that the Green function for this case is [9]:

$$G(r,t,r',t') = -\frac{1}{4\pi\,k(t-t')\sqrt{(rr')}}\sum_n (2n+1)\exp[-(r^2+r'^2)/4k(t-t')]$$

$$\times \quad I_{n+1/2}\,(rr'/2k(t-t')) \; \frac{P_n(\mu)P_n(\mu')}{(1-\mu_o^2)\,P_n(\mu_o)\left.\dfrac{\partial^2 P_n(\mu)}{\partial n\,\partial\mu}\right|_{\mu=\mu_o}} \qquad (7)$$

$I_{n+1/2}\,(x)$ is the modified Bessel function and $P_n(\mu)$ is the Legendre function.

The summation over n is for succesive roots of $\left.\dfrac{dP_n(\mu)}{d\mu}\right|_{\mu=\mu_o} = 0$ greater than -1/2.

For the finite (i.e., truncated) cone case [fig.2], we assume, as in the infinite cone case, a uniform azimuthally symmetric laser irradiation is incident on the cone surface. The cone length is assumed large enough compared to the real emitter radius so that the upper part of cone (at radius r=d in fig.2) is kept at a constant temperature by a heat reservoir. The result is

$$G(r,t,r',t') = -\sum_n \sum_m \frac{(2n+1)}{2\pi\, k\sqrt{(rr')}} \frac{J_{n+1/2}(\gamma_{nm}\, r) J_{n+1/2}(\gamma_{nm}\, r')}{d^2\,[J'_{n+1/2}(\gamma_{nm} d)]^2}$$

$$\times \frac{P_n(\mu)P_n(\mu')}{(1-\mu_o^2)\,P_n(\mu_o)\left.\dfrac{\partial^2 P_n(\mu)}{\partial n\,\partial\mu}\right|_{\mu=\mu_o}} \exp(-\gamma_{nm}^2\, k(t-t')) \qquad (8)$$

where $J_{n+1/2}(x)$ is a Bessel function and the summation over m is for roots of $J_{n+1/2}\,(\gamma_{nm}\, d) = 0$.

II.1. SURFACE GENERATION OF HEAT

For a uniform spatial and temporal distribution of CW laser radiation at the surface of an infinite cone model the temperature distribution [9] is

$$T(r,\theta,t) = \sum_n \sum_\alpha Q_o(1-R(\lambda)) \frac{(2n+1)}{4K} \frac{r\,\Gamma(\alpha+n/2+1)}{\Gamma(\alpha+1)\;\Gamma(\alpha+n+3/2)}$$

$$\times \quad \Gamma(\alpha+n/2-1/2\,;\frac{r^2}{4kt})\,\frac{P_n(\mu)}{(1-\mu_o^2)^{1/2}\left.\frac{\partial^2 P_n(\mu)}{\partial n\,\partial\mu}\right|_{\mu=\mu_o}} \tag{9}$$

where $\Gamma(x)$ is the complete Gamma function and $\Gamma(x;y)$ is the incomplete gamma function.

In the case for which the cone degrades into a plane ($\theta_o=\pi/2$) the temperature distribution along the axis ($\theta=0$) is

$$T(r,t)=\frac{Q_o(1-R(\lambda))}{4K}\,\frac{r\Gamma(-1/2;\frac{r^2}{4kt})}{\Gamma(3/2)} \tag{10}$$

$$=\frac{Q_o(1-R(\lambda))}{4K}\sqrt{(rt)}\;\mathrm{ierfc}\,(\frac{r}{\sqrt{(4kt)}}) \tag{11}$$

where $\mathrm{ierfc}\,(x)=\int_x^\infty \mathrm{erfc}\,(z)\,dz$ and erfc is the error function. The planar case correspond to the temperature distribiution in the laser irradiated anode.

II.2 THE VOLUME GENERATION OF HEAT

II.2.1 THE CALCULATION OF CURRENT DISTRIBUTION

In this section we will consider the temperature distribution in the emitter tip by resistive generation of heat due to a tunneling current flow across the STM junction. To avoid a singularity in the current density at the apex of the cone, we assume that in the region denoted as 1 for $0 \le r \le c$ (in fig.2), the constant current density $J_o \sim 10^7 - 10^8$ amp/cm^2 flows into the region through the finite conical tip surface. This approximation is not unreasonable because it assume a more realistic current distribution over a finite area rather than through a singular point. Another justification for this approximation is that the field in this region decays so rapidly that for $r > c$, it becomes negligible and

$$\times \frac{P_{n_1}(\mu')P_{n_2}(\mu')}{\left.\frac{\partial^2 P_{n_1}(\mu)}{\partial n_1\,\partial\mu}\right|_{\mu=\mu_o}\left.\frac{\partial^2 P_{n_2}(\mu)}{\partial n_2\,\partial\mu}\right|_{\mu=\mu_o}} k\, d^3r' \qquad (13)$$

II.2.3 THOMSON HEAT AS A SOURCE TERM

When both an the electric and heat current exist at the same time in the volume of a conductor, there can also be Thomson heat produced or absorbed in addition to resistative or Joule heat. The Thomson heat evolved (or absorbed) per unit volume per per unit time is given $-\sigma_T\, J\bullet\nabla T$ (When the Thomson heat is absorbed, the Thomson coefficient σ_T is positive if J and ∇T are parallel) [11]. As a source of volume generation of heat we use the current density obtained in sec. II.2.1 and the temperature distribution given in sec. II.1. The source distribution (i.e., the Thomson heat evolved in this system) is $F(r,t)=\sigma_T\, J\bullet\nabla T$. The temperature distribution, with Thomson heat as a source, can be found from eq. (4):

$$T(r,\theta,t)=\sigma_T\, J_o \frac{Q_o(1-R(\lambda))}{4K}\sum_n (2n+1)\frac{\Gamma(\alpha+n/2+1)}{\Gamma(\alpha+1)\,\Gamma(\alpha+n+3/2)}\int_o^t dt'\int_{v_1} G(r,t,r',t')$$

$$\times\,\Gamma\left(\alpha+n/2-1/2;\frac{r'^2}{4k(t-t')}\right)\frac{P_n(\mu')}{(1-\mu_o^2)^{1/2}\left.\frac{\partial^2 P_n(\mu)}{\partial n\,\partial\mu}\right|_{\mu=\mu_o}} k\, d^3r' + \sigma_T \frac{Q_o(1-R(\lambda))I}{8\pi\, K(1-\mu_o^2)^{3/2}}\sum_{n_1}\sum_{n_2}\sum_{\alpha}$$

$$\times\,(2n_1+1)(2n_2+1)\frac{\Gamma(\alpha+n_1/2+1)}{\Gamma(\alpha+1)\,\Gamma(\alpha+n_1+3/2)}\int_o^t dt'\int_{v_2} G(r,t,r',t')\frac{(n_2 r'^{n_2-1}+d^{2n_2+1}(n_2+1)r'^{-n_2-2})}{(n_2 c^{n_2+1}+d^{2n_2+1}(n_2+1)c^{-n_2})}$$

$$\times\,\Gamma\left(\alpha+n_1/2-1/2;\frac{r'^2}{4k(t-t')}\right)\frac{P_{n_1}(\mu')P_{n_2}(\mu')}{\left.\frac{\partial^2 P_{n_1}(\mu)}{\partial n_1\,\partial\mu}\right|_{\mu=\mu_o}\left.\frac{\partial^2 P_{n_2}(\mu)}{\partial n_2\,\partial\mu}\right|_{\mu=\mu_o}} k\, d^3r' \qquad (14)$$

no current is assumed to flow through the surface of the cone in the region 2 (see fig.2) [10]. The spatial polar coordinate $r=c\sim 3\times10^{-5}$cm defines the lower boundary of region 2. We also truncate the cone at $r=d\sim 1$mm. To obtain the current density distribution in region 2, we solve the Laplace equation for the potential of the current field $J=-\sigma \nabla V$ satisfying the continuity equation $\nabla\bullet J=0$. The resulting current density distribution in region 2 ($c \le r \le d$) is given by

$$J_2(r,\theta) = -\sigma \nabla V$$

$$=\sum_n \frac{(2n+1)}{2\pi} \frac{(nr^{n-1}+d^{2n+1}(n+1)r^{-n-2})}{(nc^{n+1}+d^{2n+1}(n+1)c^{-n})} \frac{P_n(\mu)}{(1-\mu_o^2)\left.\frac{\partial^2 P(\mu)}{\partial n\, \partial\mu}\right|_{\mu=\mu_o}} I \qquad (12)$$

where V is the electric potential, σ is the electrical conductivity and the current $I=J_o\pi c^2\sin\theta_o$ in this region is constant.

II.2.2 JOULE HEAT AS A SOURCE TERM

In this section we calculate the temperature distribution assuming the Joule heat as a source term. This volume source term is $F(r,t)= J^2\rho$, where ρ is the electrical resistivity. The temperature distribution inside the cone emitter is obtain from eq.(4):

$$T(r,\theta,t)=\int_o^t dt'\int_{v_1} G(r,t,r',t') \frac{J_1^2\rho}{K} k\, d^3r' + \sum_{n_1}\sum_{n_2} (2n_1+1)(2n_2+1)\frac{I^2\rho}{4\pi^2(1-\mu_o^2)^2}$$

$$\times \int_o^t dt'\int_{v_2} G(r,t,r',t') \frac{(n_1 r'^{n_1-1} + d^{2n_1+1}(n_1+1)r'^{-n_1-2})}{(n_1 c^{n_1+1}+d^{2n_1+1}(n_1+1)c^{-n_1})} \frac{(n_2 r'^{n_2-1}+d^{2n_2+1}(n_2+1)r'^{-n_2-2})}{(n_2 c^{n_2+1}+d^{2n_2+1}(n_2+1)c^{-n_2})}$$

In the next section, we describe the calculation of the thermoelectric voltage due to both surface and volume sources of heat.

III. THERMOELECTRIC POTENTIAL

We have previously considered the spatial and temporal temperature distribution due to the laser irradiance of the STM junction. This produces not only a temperature gradiant due to surface generation of heat but also a rectified dc current component through the junction. The thermal energy in the tip consists of heat brought into the volume by the heat conduction through the surface as well as resistive heat due to the current density established by the laser field even in absence of an external bias voltage. In addition, there is a Thomson heat due to the temperature gradient as well as current flow in the junction. This heat can be either absorbed or evolved into the system influencing the temperature gradient across the juction. The thermoelectric potential generated by the field due to the temperature gradiant between two points in the presence of current can be written as [11]

$$V_{ther} = -\int E_{ther} dr \tag{15}$$

$$= \int \sigma_T \nabla_r T \, dr \tag{16}$$

$$= \int_{T_o}^{T_1} T \frac{dS}{dT} dT \tag{17}$$

$$= T_1 S(T_1) - T_o S(T_o) - \int_{T_o}^{T_1} S dT \tag{18}$$

where σ_T is related to the thermoelectric power S by $\sigma_T = T\frac{dS}{dT}$.

Therefore the thermoelectric potential produced across the junction is

$$V_{junc} = T_1 S_e(T_1) - T_2 S_a(T_2) - \int_{T_o}^{T_1} S_e \, dT + \int_{T_o}^{T_2} S_a \, dT \qquad (19)$$

where T_1 and T_2 are the temperatures of the emitter and anode base, S_e and S_a are the absolute thermoelectric powers of the emitter and anode base, respectively. It is assumed that $T_o=0$ at sufficiently large distances from the apex.

For the sake of completness we also consider the current density due to the spatial dependence of the chemical potential ζ. Since this quantity is a function of the temperature the differential variation in chemical potential with temperature in the junction can also produce a thermoelectric voltage in the juction [12]. Therefore the total field produced in the system is

$$E_{total} = \frac{J}{\sigma} + \frac{1}{e} \nabla_r \zeta - \sigma_T \nabla_r T \qquad (20)$$

where J/σ is the field produced by the laser irradiation in the absence of an external applied voltage. The thermoelectric potential generated due to the effective field $E_{eff} = \frac{1}{e} \nabla_r \zeta - \sigma_T \nabla_r T$ in the STM junction is

$$V_{eff} = - \int (\frac{1}{e} \nabla_r \zeta - \sigma_T \nabla_r T) dr \qquad (21)$$

or

$$V_{eff} = - \frac{1}{e} (\int_{T_o}^{T_1} \frac{d\zeta_e}{dT} dT - \int_{T_o}^{T_2} \frac{d\zeta_a}{dT} dT) + (\int_{T_o}^{T_1} T \frac{dS_e}{dT} dT - \int_{T_o}^{T_2} T \frac{dS_a}{dT} dT) \qquad (22)$$

where ζ_e and ζ_a are the chemical potentials of the emitter and anode, respectively. In the case where $T_1 = T_2 = T$ (T is the local equilibrium temperature at the junction and assuming $T_o=0$) the effective thermoelectric potential becomes

$$V_{eq} = -\frac{1}{e}\int_0^T\left(\frac{d\zeta_e}{dT} - \frac{d\zeta_a}{dT}\right) + T[S_1(T)-S_2(T)] - \int_0^T(S_e - S_a)\,dT \qquad (23)$$

However, for the present application, this contribution is of second -order and will not be included in the determination of V_{junc}.

IV. DISCUSSION AND CONCLUSIONS

In this paper we have studied the thermal effects in an STM junction under laser irradiance. For a tungsten emitter modeled as a cone, we have used a Green function method to obtain analytic expressions for the temperature distribution with both surface and volume sources of heat. Using the laser irradiance, resistive and Thomson heat as the surface and volume sources respectively, we have calculated the thermoelectric potential contribution to the bias voltage across the junction. Some specific results we have obtained are summarized below.

The temperature rise in the conical tip due to surface generation of heat varies almost linearly with laser intensity and heating time and depends strongly on the cone angle and thermal parameters [fig.3] . In a heating time of about 120 ns with a CW laser intensity of 1 MW/cm^2 , the temperature rise of a conical emitter with half- cone angle of 15° is about 1100 ^{o} K near the apex (within 1 nm) and drops rapidly for distance beyond a micron from the apex [fig.4].

The temperature distribution due to Joule heat produced by the laser- induced tunneling current depends strongly on the magnitude of the induced current density [fig.5]. For densities in the range 10^6~10^7 amp/cm^2 the temperature increase is neglegible because the current density is so small and the thermal conductivity of the material is high. When the current density is about 10^8 amp/cm^2 , the temperature increase is about 50 ^{o} K. This temperature change is approximately uniform near the tip apex and then begin to drop rapidly for distance beyond 100 nm. When the current density is greater than 5×10^8 amp/cm^2 the temperature of the conical emitter (half cone

angle of 15 °) increases dramatically and is on the order of 2000 °K. These temperatures already begin to exceed the melting temperature of most metals. For comparision, T_m for tungsten is 3683 ° K.

The temperature change due to Thomson heat generated or absorbed by the system is relatively small compared to the both the laser induced surface heating and the resistive heating due to the tunneling current because the current flow is small and consequently the heat transport through the emitter is so small. Therfore the heating or cooling effect due to the Thomson heats is negligible compare to the surface and Joule heating effects.

Lastly the thermoelectric potential is due principally to surface heating and depends on the intensity of the laser irradiation. The induced thermoelectric voltage due to surface generation of heat for a laser intensity of 1.2 MW/cm^2 is about 10 mV [fig.6].

REFERENCES

[1] L. Arnold and W. Krieger, J. VAC. SCI. TECHNOL. A6 (1988) 465

[2] W. Krieger, H. Koppermann, T.Suzuki, H.Walter, IEEE, Transaction on Instrumentation and Measurement 38 (1989) 1019

[3] W. Krieger, T. Suzuki and M. Volker, Physical Review B41 (1990) 10229

[4] H.Q. Nguyen and P.H. Cutler, T.E. Feuchtwang, Z.H. Huang, Y. Kuk, P.J. Silverman , A.A. Lucas, T.E. Sullivan, IEEE Transaction on Electron Device 36 (1989) 2671

[5] T.E. Sullivan, P.H. Cutler, A.A. Lucas, Surface Science 62 (1977)455

[6] W.W. Dolan, W.P. Dyke, and J.K. Trolan, Physical Review, 91 (1953) 1054

[7] S. Grafstrom, J. Kowalski, R. Neumann, O. Prosst, and M. Wortge, J. VAC. SCI. TECHNOL . A8 (1991) 357

[8] P. Morse and H. Feshbach, Method of Theoretical Physics (McGRAW-HILL, NY. 1954) ch. 7

[9] S.H. Park, P.H. Cutler and N.M. Miskovsky to be published

[10] Jun He, P.H. Cutler, N.M. Miskovsky, T.E.Feuchtwang, T.E. Sullivan and

M. Chung, Surface Science, 246 (1991) 348

[11] F.J. Blatt, P.A. Schroeder, C.L. Foiles and D. Greig, Thermoelectric Power of Metals (Plenum Press, NY. 1976) ch. 1

[12] C.C. Williams and H.K. Wickramasinghe, Nature, 344 (1990) 319

Figure Captions

Fig.1 The infinite cone model. The half- cone angle θ_o varies from 0° to 90°.

Fig.2 The fl inite cone model. The cone is truncated at r=d (~ 1 mm). The active region for electron emission is the conical surface between r=0 and r=c (~3×10^{-5} cm).

Fig.3 The laser- induced tempereture rise near the apex (10 A^o) vs. heating time for the infinite cone model. The solid line is for a laser intensity of 1.6MW/$cm^2$and the dashed line is for 1 MW/cm^2. The cone half angle is:(a)15° (b)30° (c)90°. The values of k=0.68 $cm^2 s^{-1}$, K=1.78 W/cm°K, and R=0.68.

Fig.4 The laser-induced temperature rise vs. radial distance along the emitter axis for different cone angles after a heating time of 120 ns with a laser irradiance of 1 MW/cm^2. The same value of thermal parameters as in fig.2 are used.

Fig.5 The temperature rise due to Joule heating vs. radial distance along the axis of the emitter for different current densities. The heating time is 100 ns. The resistivity of the tungsten sample was taken to be 5×10^{-5} ohm cm.

Fig.6 The laser induced thermoelectric voltage vs. energy flux of CW laser beam with different cone angle. The surface generation of heating effect is only considered in this data and the heating time is 100 ns.

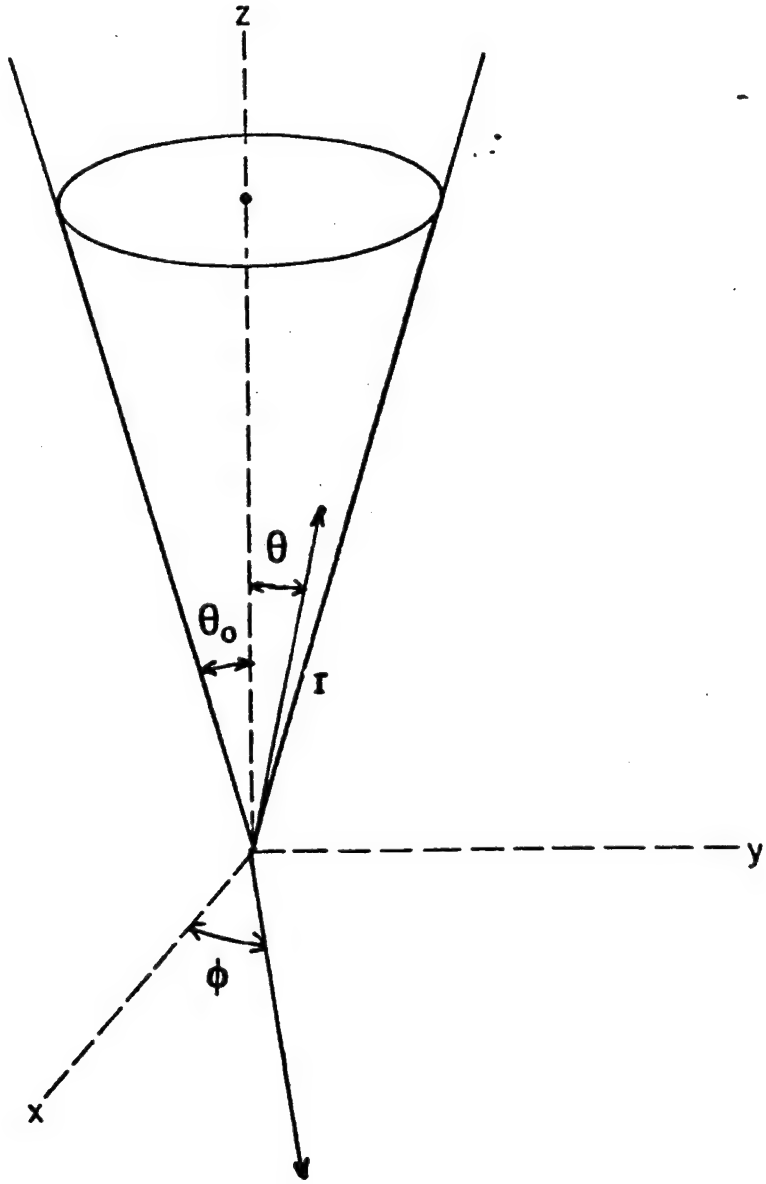
z
θ
θo
r
y
φ
x

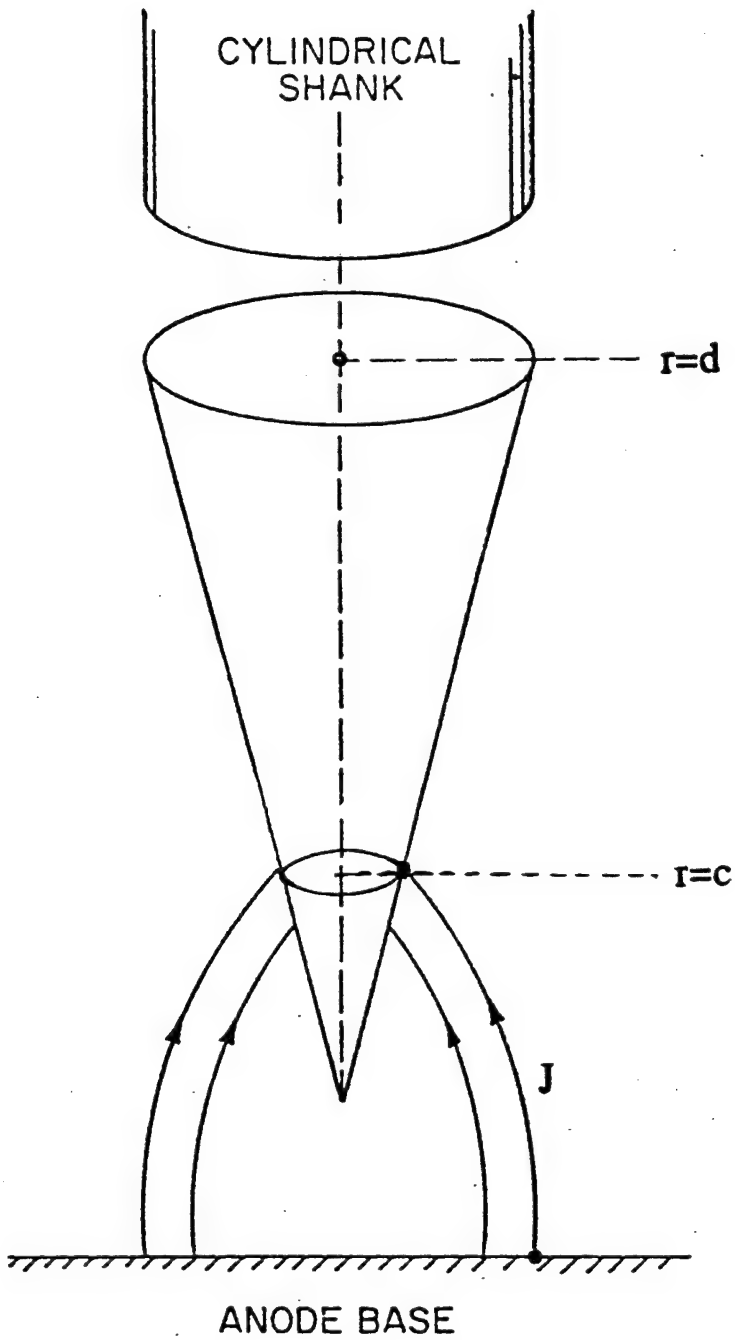
CYLINDRICAL
SHANK
r=d
r=c
J
ANODE BASE

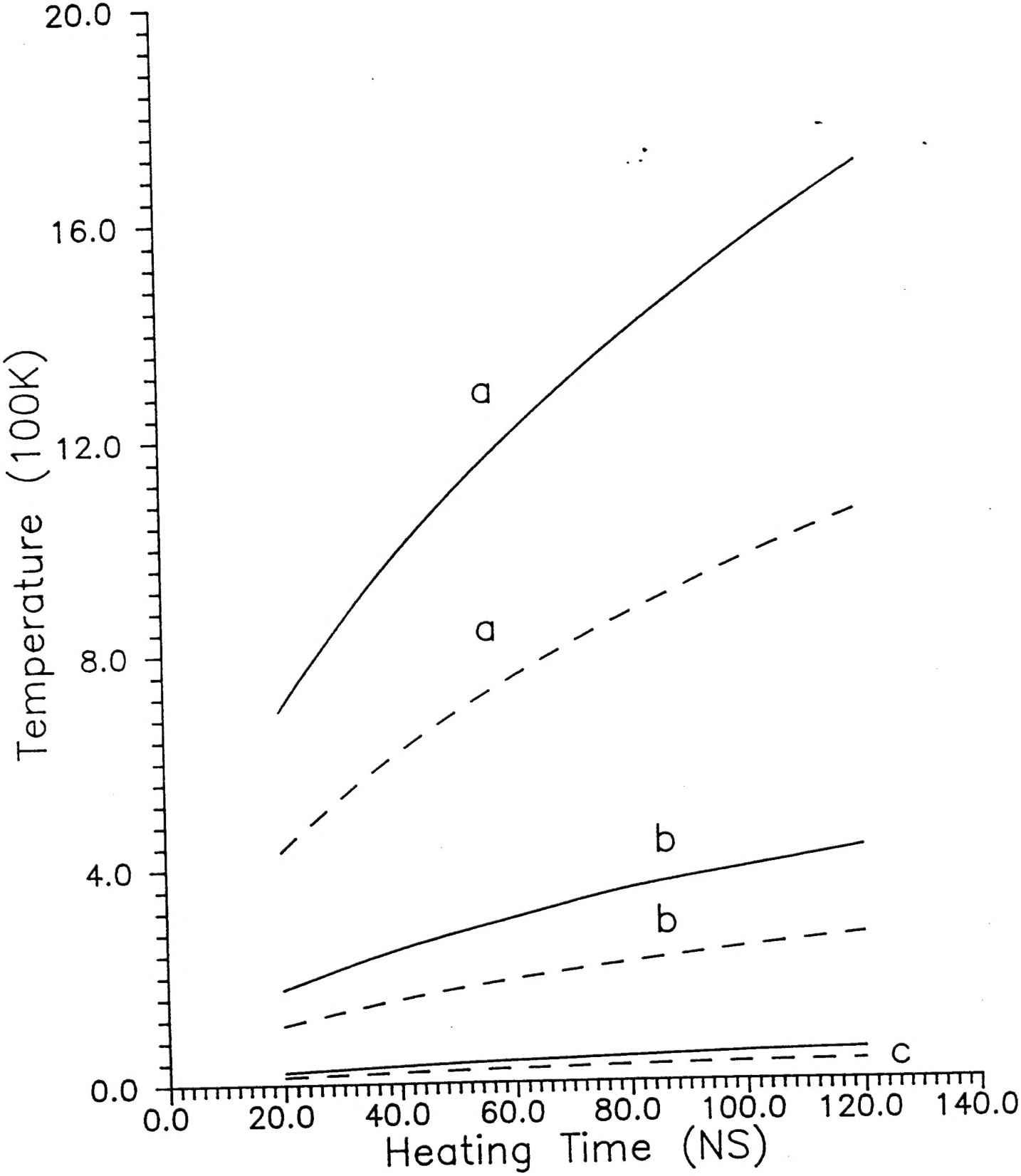
20.0
16.0
12.0
8.0
4.0
0.0
Temperature (100K)
a
a
b
b
c
0.0
20.0
40.0
60.0
80.0
100.0
120.0
140.0
Heating Time (NS)

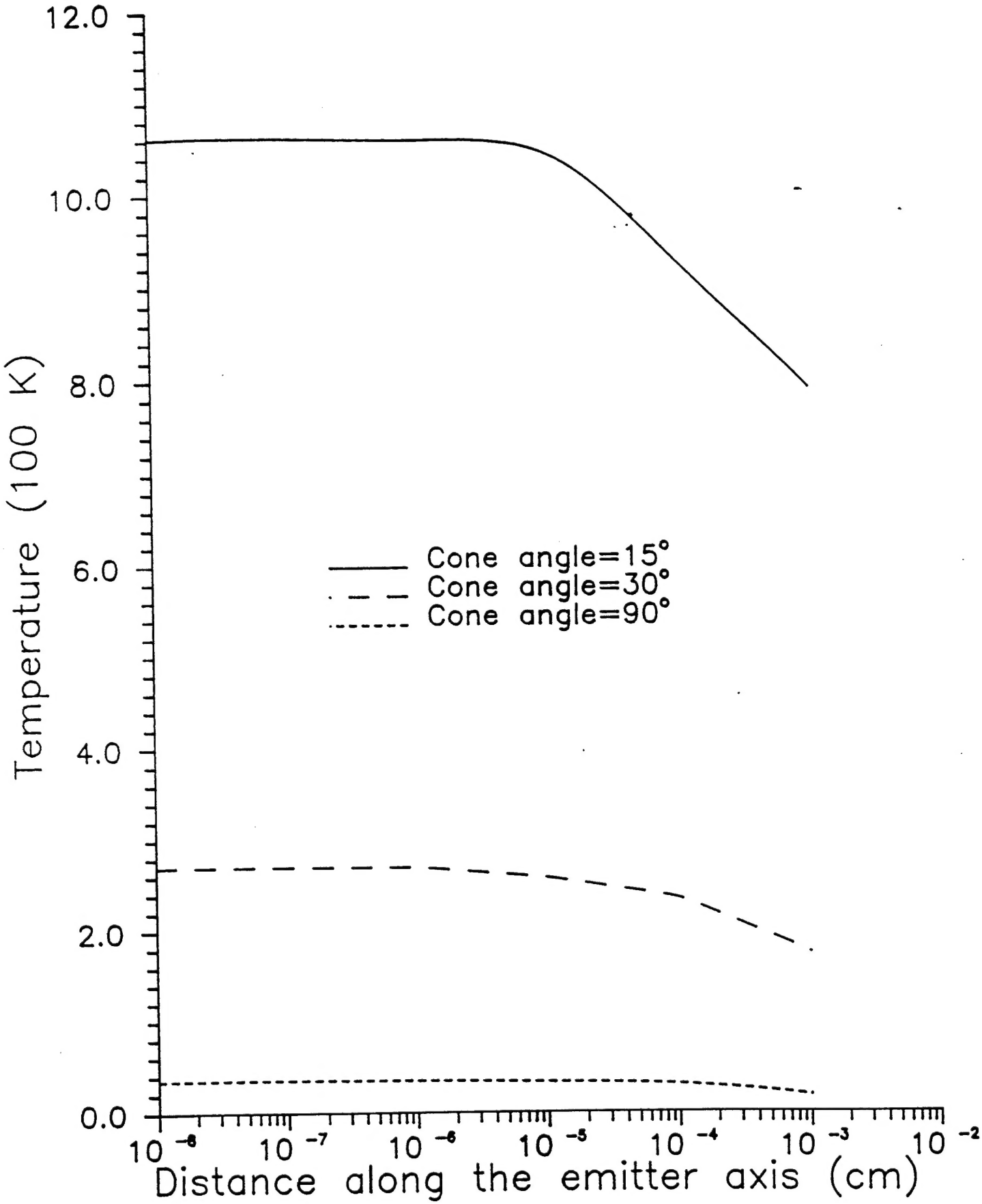
12.0
10.0
8.0
6.0
4.0
2.0
0.0
Temperature (100 K)
Cone angle=15°
Cone angle=30°
Cone angle=90°
10 -8
10 -7
10 -6
10 -5
10 -4
10 -3
10 -2
Distance along the emitter axis (cm)

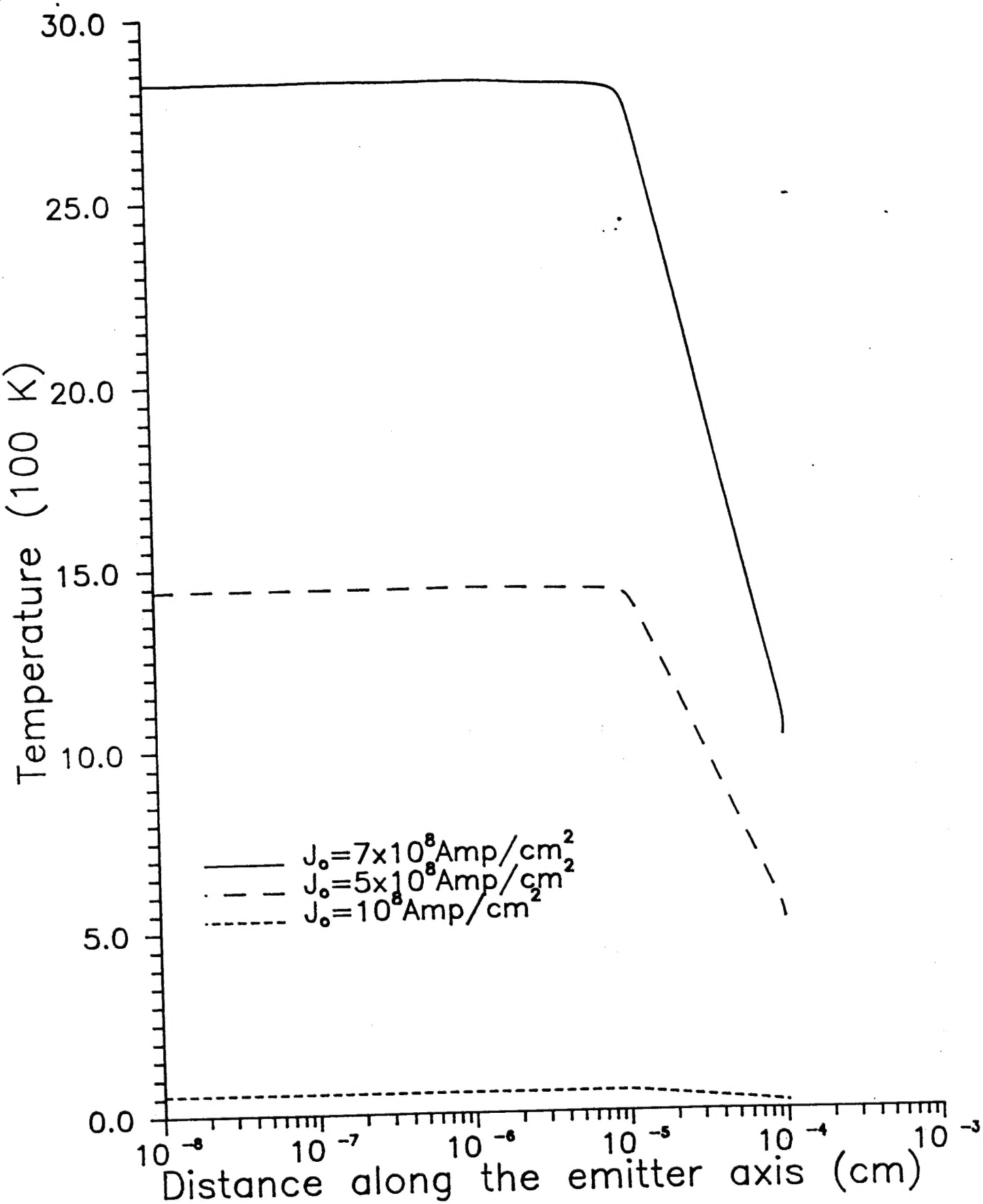
30.0
25.0
20.0
15.0
10.0
5.0
0.0
Temperature (100 K)
$J_o=7\times10^8$Amp/cm^2
$J_o=5\times10^8$Amp/cm^2
$J_o=10^8$Amp/cm^2
10^{-8}
10^{-7}
10^{-6}
10^{-5}
10^{-4}
10^{-3}
Distance along the emitter axis (cm)

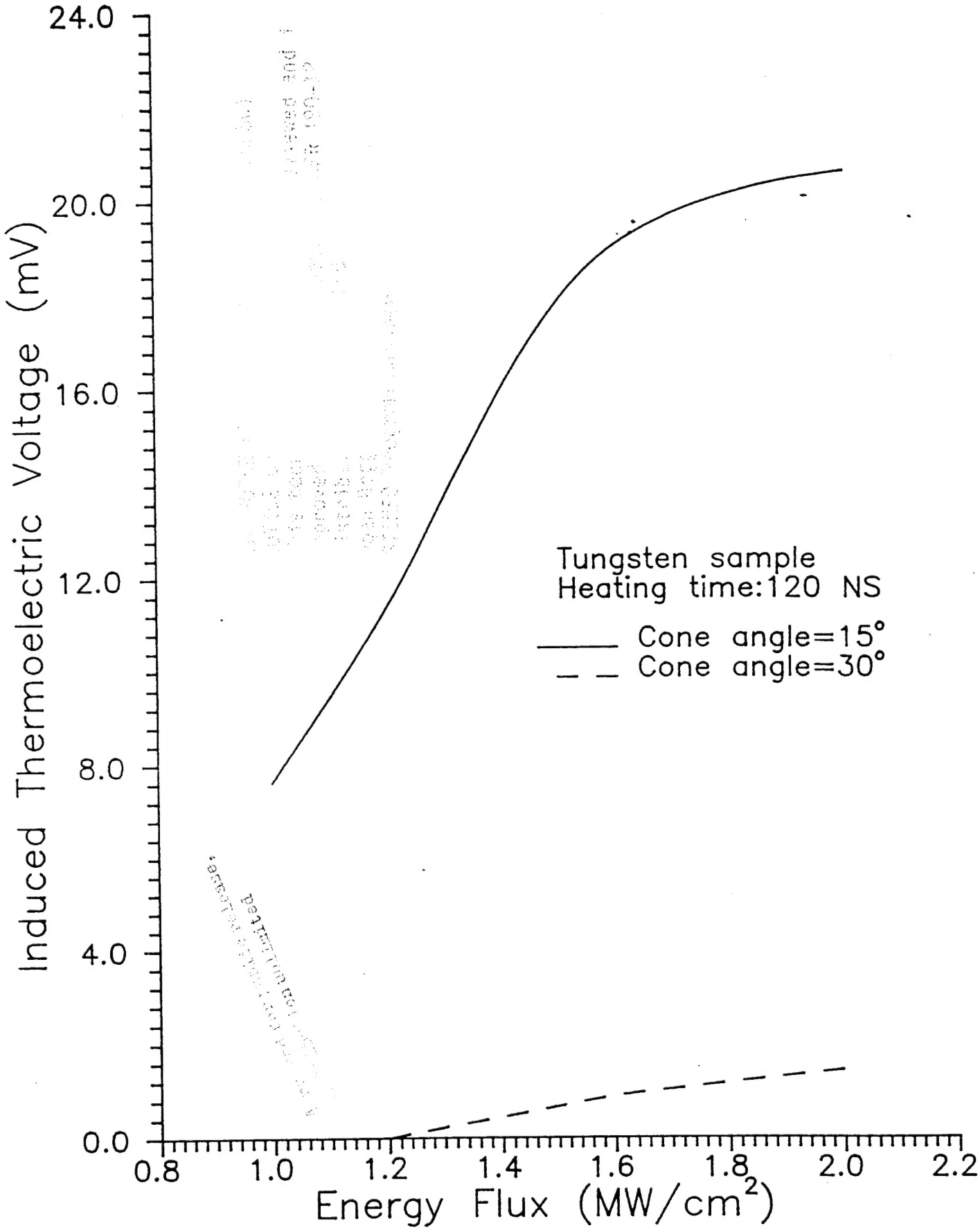
Induced Thermoelectric Voltage (mV)
24.0
20.0
16.0
12.0
8.0
4.0
0.0
0.8
1.0
1.2
1.4
1.6
1.8
2.0
2.2
Energy Flux (MW/cm^2)
Tungsten sample
Heating time:120 NS
Cone angle=15°
Cone angle=30°